MICROMAGNETIC INVESTIGATIONS OF MAGNETIC MULTILAYERS AND FERRITES BY TRANSMISSION ELECTRON MICROSCOPY

by David McAdam Donnet

submitted for the degree of Ph.D at the University of Glasgow.

November 1992

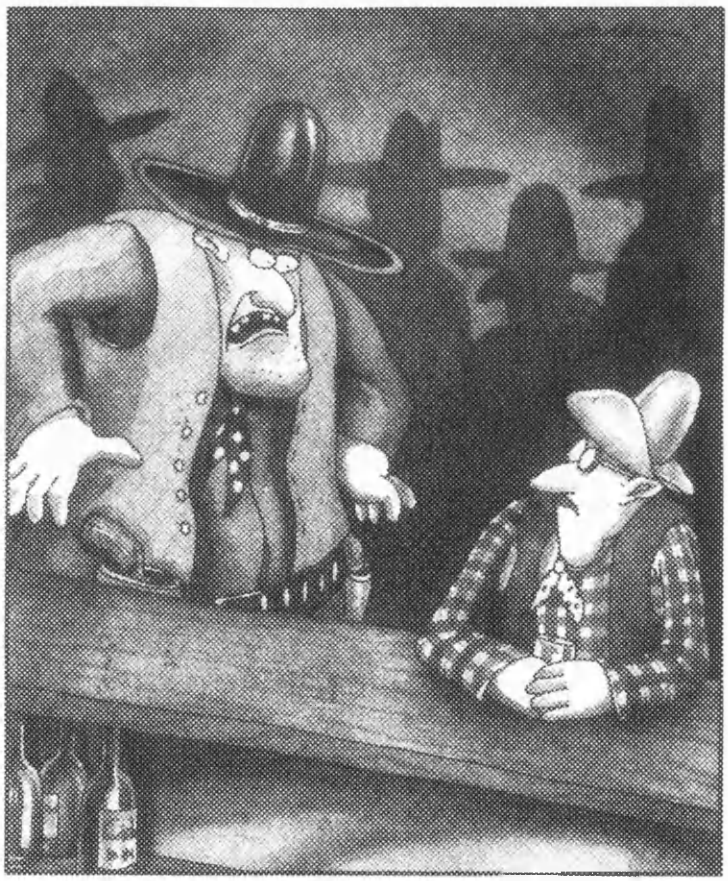

"I asked you a question, buddy. . . . What's the square root of 5,248?"

Contents

Chapter 2

Chapter 3

Chapter 4

Chapter 7

Chapter 8

Chapter 9

Acknowledgements

I would like to take this opportunity to thank the many people whose contributions throughout the three years made this project possible.

Foremost I wish to thank my supervisor, Professor John Chapman for his excellent guidance and help at all times and Professor R P Ferrier for his encouragement and the provision of the electron microscope facilities in the Solid State Group at the University of Glasgow.

I am indebted to Dr H W van Kesteren, Dr W B Zeper and Dr P J van der Zaag from Philips Research for supplying the necessary specimens throughout the project.

I would also like to thank all those at Philips Research who made my stay so enjoyable and productive. Thanks especially to Dr J P C Bernards for overseeing all my work and to Dr A den Boef for his help in operating the force microscope.

Thank you also to Dr K O'Grady and Mr V Lewis for the use of their AGFM at the University of North Wales, Bangor and to Prof D M Titterington and Dr W Qian of the Statistics Dept. for their help in quantifying the domain edge boundaries.

For maintenance of the electron microscope facilities at Glasgow I must thank Mr J Simms and Miss M Low for maintaining the CTEM machines and to Dr W A P Nicholson and Mr A Howie for maintaining the HB5 STEM.

For the many diagrams and photographic prints presented in the thesis I would like to thank Miss M Low, Mrs M Waterson and Mr I McVicar.

I would also like to thank the SERC for the provision of a grant and to CAMST for financial support during my visit to Bangor.

Finally I wish to thank my parents, without whose help and support none of this would have been possible.

Declaration

This thesis is a record of the work carried out by me in the Department of Physics and Astronomy at the University of Glasgow. The work described is my own, apart from the deposition of the multilayer and ferrite specimens which were provided by Philips. Some of the work in this thesis can be found in the following papers:

'Differential phase contrast microscopy of magnetic materials', J N Chapman, R Ploessl and D M Donnet, *Ultramicroscopy*, in press.

'Investigation of domain structures in Co/Pt multilayers by modified differential phase contrast microscopy', D M Donnet, J N Chapman, H W van Kesteren and W B Zeper, *J. Magn. Magn. Mater.*, **115** 342 (1992).

'An investigation of thermomagnetically written marks in Co/Pt multilayers', D M Donnet, J N Chapman, H W van Kesteren and W B Zeper, *J. Magn. Magn. Mater.*, accepted for publication.

'Domain structures in MnZn-ferrites', P J van der Zaag, A Noordermeer, D M Donnet and J N Chapman, Proc. ICF6, accepted for publication.

This thesis has not previously been submitted for a higher degree.

David Donnet

November 1992

Summary

The work described in this thesis is a study of domain structures in Co/Pt multilayers and MnZn-ferrites using Lorentz microscopy. The vast majority of the work is concerned with the multilayers which are produced for use as future magneto-optical media. The basic ideas of ferromagnetism and domain structures together with an outline of the concepts of magneto-optical recording are given in chapter 1.

Throughout this thesis, domains are observed using the Foucault, Fresnel and differential phase contrast (DPC) modes of Lorentz microscopy. Chapter 2 explains the techniques used and how they are applied to the materials in question. Also given, is a brief discussion of image formation in a scanning transmission electron microscope (STEM) for DPC imaging which allows induction distributions within thin magnetic films to be mapped.

Chapter 3 discusses the deposition and initial characterisation of the multilayers and also reports on the preliminary results achieved from the electron microscopy of these films. Optimum conditions for all the Lorentz modes are given.

The main body of results from the Co/Pt multilayers is presented in chapters 4-7. Chapter 4 deals with all the in-situ magnetising results using DPC microscopy. Domain patterns in various remanent states were imaged. Such observations provided great insight into the mechanisms (nucleation and reversal) that determine the shape of the bulk magnetising loop. Remanence loops were constructed from the MDPC images and their shapes agreed well with those measured on the AGFM.

An investigation of thermomagnetically written domains (marks) was carried out in chapter 5. Marks written with different parameters were imaged by MDPC and their most important features investigated. It was found that the size of the marks was only weakly dependent on the applied bias field, but increased linearly with increasing laser power. Reverse domains were present in the written mark until the bias field exceeded 30kA.m^{-1}, but above this value the domain boundary became more ragged. A quantitative analysis of the electron signal

from a series of marks written with different bias fields was undertaken and the shape of the curve agreed well with actual recording results.

In chapter 6 domain wall calculations were carried out and the domain periods modelled for a series of multilayers with increasing numbers of bilayers. The theoretical results agreed best with the experimental measurements when a magnetic characteristic length of 6.7nm was used in the model.

Chapter 7 deals with the work carried out during a placement at Philips Research Laboratories. The domain structure of the multilayers was investigated with scanning magnetic force microscopy and the images and results compared with those achieved from Lorentz microscopy. It was found that the greatest spatial resolution and reproducibility was achieved with MDPC microscopy, although SMFM was most useful when imaging written tracks because no specimen preparation was required.

Chapter 8 concerns all the work carried out on thinned samples MnZn-ferrite. Domain structures in an ac-demagnetised state were examined for films with different grain sizes. In general it was established that most grains were multi-domain. Local variations in the atomic composition across grain boundaries were investigated using energy dispersive x-ray analysis (EDX) and substantial Zn depletion was found in the vicinity of grain boundaries..

Chapter 9 contains conclusions drawn from the observations of chapters 4-8 along with suggestions for the continuation of the work.

Chapter 1

Ferromagnetism and magneto-optical recording

1.1 Basic ferromagnetism

A ferromagnetic material is one which exhibits a spontaneous magnetisation $\underline{M}$ in the absence of any external field. This is produced by a co-operative phenomenon (called the exchange interaction) leading to the magnetic moments being aligned parallel to each other. As the temperature increases, the disordering effects increase until a temperature is reached where the sample loses its spontaneous magnetisation, its magnetic moments become disordered and the material acts as a paramagnet. This temperature is called the Curie temperature T_c.

From the knowledge that the magnetic fields required to magnetise a paramagnetic substance were around 10^6 times greater than those needed for a ferromagnet like iron, Weiss postulated in 1907 that a high internal field existed spontaneously in ferromagnetic materials. He thus introduced the idea of a molecular field in which the interaction of one magnetic moment with the remainder of the sample could be replaced by an effective field $\underline{B_E}$ which is directly related to the average magnetisation $\underline{M}$ of the sample, by:

$$\underline{B}_E = \lambda \underline{M} \qquad (1.1)$$

where λ is a constant.

1.1.1 Ferromagnetic domains and energy considerations

Below the Curie temperature, it was expected that a ferromagnetic material should be magnetised in a single direction; instead, however, it was found that small regions within the material were magnetised to a saturation value predicted by the molecular field, but different regions were magnetised in directions which need not be correlated. These regions are called magnetic

domains. The magnetic moment of the bulk specimen is equal to the vector sum of the moments of the individual domains so that the observed magnetisation of the specimen may be lower than the predicted value, or even zero. The reason for the formation of this domain structure is the need to minimise the free energy of the sample. The following discussion outlines the main energy contributions to be accounted for.

1.1.2 Exchange energy

The experimental values of λ found from measurements of T_c in ferromagnets shows that it is many orders of magnitude too great for the origin of the molecular field to lie in magnetostatic interactions between neighbouring moments. Instead it originates from the quantum mechanical exchange interaction (Heisenberg 1928). This fundamental energy term initiates ferromagnetic order and is electrostatic in origin. It is a consequence of the Pauli exclusion principle which states that two electrons with parallel spins cannot exist in the same spatial wavefunction whilst two electrons with opposite spins can. This results in the mean spacing for a pair of electrons with parallel spins being different from a pair with anti-parallel spins. Therefore the electrostatic energy of the system becomes dependent on the orientation of the spins involved. The energy associated with this exchange interaction for a pair of neighbouring spins is:-

$$E_{ex} = -2J_{ij}S_i \cdot S_j \qquad (1.2)$$

where J_{ij} is a constant called the exchange integral and $\underline{S}_i$, $\underline{S}_j$ are the magnetic spin moments. The negative sign in the expression implies that the minimum exchange energy configuration favours a parallel alignment of the spins. Ferromagnetism then results if $J_{ij}>0$. For a ferromagnetic solid, it is necessary to sum the exchange over all the electron pairs which may contribute to the energy. The total energy is then given by:-

$$E_{EX} = -2\Sigma\Sigma J_{ij}S_i \cdot S_j \qquad (1.3)$$

1.1.3 Magnetostatic energy

The magnetostatic energy, E_m of a specimen arises from a Coulombic interaction between dipoles and magnetic fields. When a ferromagnetic body is isolated and placed in a saturating field, charge is produced at its end surfaces. This charge induces an external stray field distribution and an internal field H_d, which opposes the internal saturation magnetisation $\underline{M}$ and is called the demagnetization field. For a solid of volume V and surface area S, H_d is defined as:-

$$H_d(\underline{r}) = \frac{1}{4\pi}\int_V -\frac{\nabla.\underline{M}}{r^2}dV + \frac{1}{4\pi}\int_S \frac{\underline{M}.\underline{n}}{r^2}dS \qquad (1.4)$$

where $\underline{r}$ is a position vector for the field points, $\underline{n}$ is a unit vector normal to the surface, $\nabla.\underline{M}$ denotes volume charge density and $\underline{M}.\underline{n}$ denotes surface charge density. The magnetostatic energy is then given by:-

$$E_m = -\frac{1}{2}\mu_o\int_v \underline{M}.\underline{H}_d\,dV \qquad (1.5)$$

where the integral is taken over all space. From the above expressions it is clear that the energy depends on the size and shape of the specimen as well as on its magnetisation.

1.1.4 Zeeman energy

The Zeeman contribution to the energy of a magnetic system is analogous to that found in the previous section. Now however, the energy is induced by the action of an externally applied magnetic field $\underline{H}$ and the new expression is given as:-

$$E_z = -\mu_o\int_V \underline{M}.\underline{H}\,dV \qquad (1.6)$$

1.1.5 Magnetocrystalline anisotropy energy

Many ferromagnetic materials (eg cobalt) are magnetically anisotropic, meaning that the internal energy of the domains is dependent on the direction of the spontaneous magnetisation $\underline{M}$ within them.

For a bulk specimen, in which surface effects may be neglected, the direction of the spontaneous magnetisation in the absence of any external field will coincide with particular crystallographic axes called the directions of easy magnetisation. A state of minimum energy exists in a particular domain when its magnetisation lies along one of the preferred directions.

The simplest form is uniaxial anisotropy which can be found in hexagonal cobalt. Here the easy direction of spontaneous magnetisation is parallel to the c-axis of the crystal. The internal energy increases as $\underline{M}$ rotates away from this axis and an expression for the resultant energy density, to a first approximation, is:-

$$E_a = K_1 \sin^2\phi \qquad (1.7)$$

where K_1 is the first order magnetocrystalline anisotropy constant and ϕ is the angle of rotation away from the easy axis.

1.1.6 Domain walls and their associated energy

The transition layer that separates adjacent domains magnetised in opposite directions is called a domain wall. Bloch (1931) first postulated that the boundary between two such domains was not sharp on an atomic scale but spread over a certain distance where the direction of the spins changes gradually from one domain to the next. The magnetisation vectors in a Bloch wall rotate about an axis perpendicular to the boundary and this produces an exchange energy per unit area which tends to increase the width of the wall. However, this in turn leads to an increase in the magnetocrystalline energy, introduced by the increased numbers of magnetisation vectors not

aligned with the easy axis. The width of Bloch domain wall is therefore a balance between the exchange and magnetocrystalline energy contributions. For bulk specimens, the magnetostatic energy contribution, arising from surface charges, can be neglected.

It is not possible however, in very thin specimens (eg. thin films) to neglect magnetostatic energy contributions. In such specimens, the film thickness is less than that of the transition layer. Charge is now present over the whole boundary wall as the magnetisation now rotates in the plane of the film. This type of wall is called a Neèl wall (Neèl 1955).

1.1.7 Domain configuration

The total energy of the system, in zero field, is a sum of the previously mentioned four energy terms:-

$$E_{TOTAL} = E_{EX} + E_m + E_z + E_A \qquad (1.8)$$

where E_A is the magnetocrystalline anisotropy energy contribution.

Figure 1.1 shows a simple example of why domain structures are formed. With the single domain (a), charge is formed on the end surfaces resulting in a large magnetostatic energy term and hence large demagnetising effects. These can first be reduced by splitting the original domain into two (or more) oppositely magnetised parallel domains (b), this causes a reduction in the external stray field and thus also reduces the magnetostatic energy. There is however a limit to the number of subdivisions possible because of the increase in the domain wall energy, due to the fact that the adjacent magnetic moments are no longer parallel. Thus the size of the domains is a balance between all the energy terms.

The magnetostatic energy can be reduced to zero by forming flux closure domains (c), so that the flux circuit is completed within the crystal. This is called a solenoidal domain structure and is only allowed if there is no strong crystal anisotropy present.

The domain structures seen experimentally via electron microscopy and

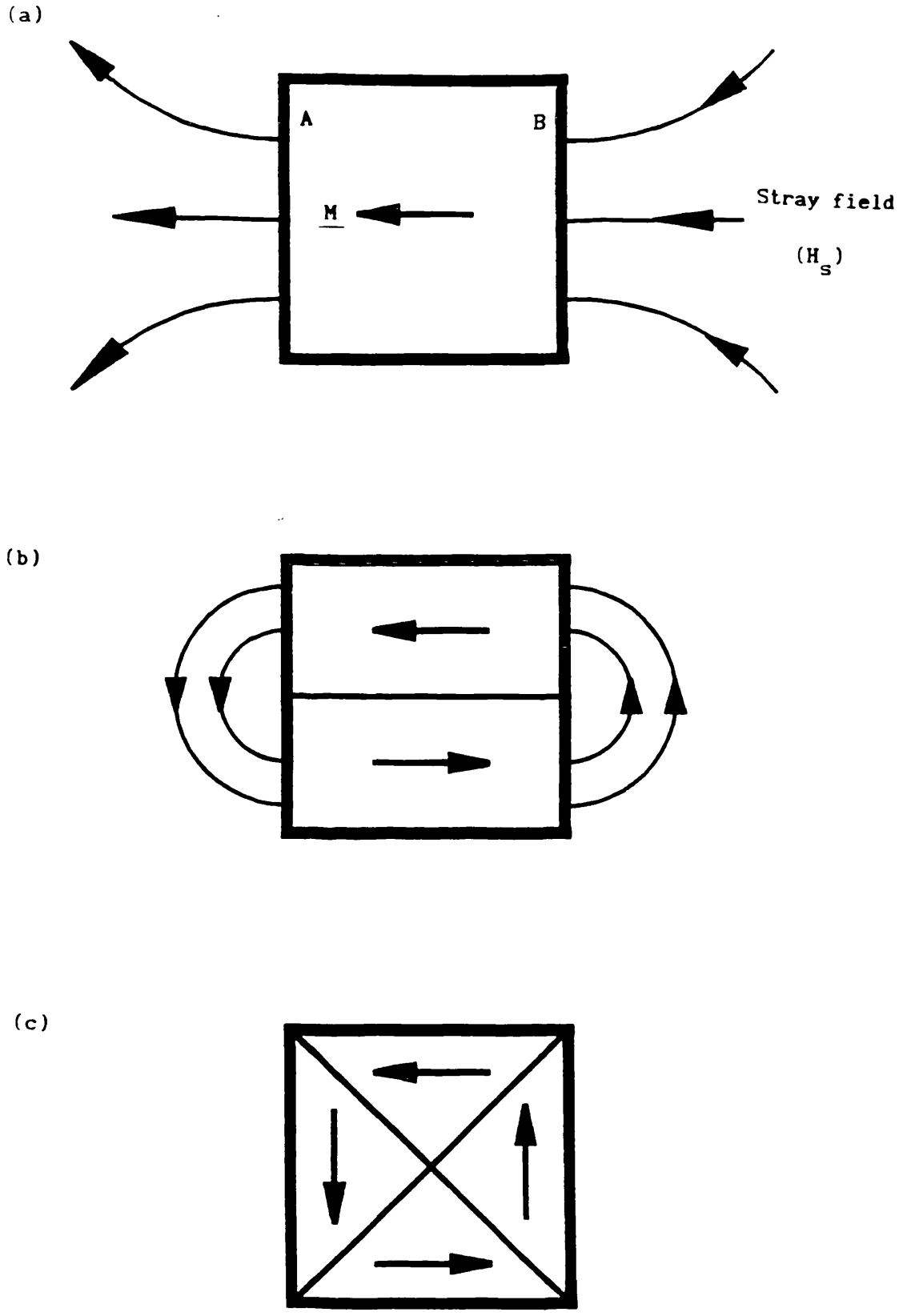

Figure 1.1 (a) A uniformly magnetised particle.
(b) A particle with two oppositely magnetised domains.
(c) A particle with a solenoidal domain structure.

magnetic force microscopy in this study are far more complicated than this simple example. In the absence of any hysteresis (where the magnetisation, under the influence of external fields, follows an irreversible path) a domain configuration always tries to lower the energy of a system by forming a domain structure with lower energy than previously. It is the presence of hysteresis however, that makes many magnetic materials attractive for information storage. In hysteretic systems, the remanent magnetisation acts as a memory of the last magnetic state of the material. Therefore once a domain has been written, its position (in the absence of external fields) shall be fixed, allowing information (in either analogue or digital form) to be stored. It is the written domains that provide the data signal when a recording head (conventional magnetic recording) or laser beam (magneto-optical recording) are reading from the recording media in the system. The next section deals with one such method of storing data in magnetic materials.

1.2 Magneto-optical recording

As its name suggests magneto-optical (MO) recording (Hartmann et al 1985, Kryder 1985, Meiklejohn 1986, Hansen 1990) is a hybrid of the existing magnetic and optical recording technologies and combines the merits of both. It allies the availability of high areal storage densities (10^8 bits.cm^{-2}) (Luitjens 1990) of optical recording (ten times that of high performance magnetic disc drives), with erasability and rewritability found in conventional magnetic recording, together with a non-contact method for writing, thus avoiding any material wear. Drawbacks do exist however; access times (≈45ms) although comparable with floppy discs are twice as long as conventional Winchester technology and are therefore not yet competitive. Also conventional MO recording lacks the facility for direct overwrite. This means that previously written data is overwritten by first resetting the magnetisation in the whole written area to one direction. This slows down the data rate by a factor of two.

The information is stored in uniaxial magnetic films in the form of small

(micron) vertical domains. Both reading and writing are performed using a focused laser beam. Writing is carried out thermomagnetically, while read-out utilises the polar Kerr effect.

1.2.1 Thermomagnetic writing

There are various schemes for thermomagnetically writing domains. Curie point writing involves locally heating the material, which has been initially saturated in one direction, with a focused laser beam to its Curie temperature T_c, whereby the material loses its spontaneous magnetisation. With a suitably orientated magnetic field present, the direction of magnetisation within the heated area is then reversed and locked-in as the medium cools back down. A schematic is shown in figure 1.2. The size of the written domains is determined by the diffraction limited spot size of the laser beam and the temperature profile of the MO medium. The minimum bit size is given by:

$$d = \frac{0.5\lambda}{NA} \tag{1.9}$$

where λ is the wavelength of the light and NA is the numerical aperture of the objective lens. This results in a typical written domain size of $\approx 1\mu m$ (Greidanus et al 1989).

Another method utilises the temperature profile of the coercive field of the material. As the medium is heated its coercivity decreases, thus domains can be written with a field that is larger than the coercivity of the heated area, but smaller than that of the remaining unheated area. This method is referred to as threshold point writing. In conventional Curie and threshold point writing, the domains are written by laser modulation (LM). That is, the applied field is kept constant while the recorded information is supplied by the modulation of the laser beam, resulting in small circular written marks as shown in figure 1.3(a). The main drawback with this writing mode is that the information cannot be directly overwritten. Whole sectors of data need be erased before new information can be written. To overcome this, it has been

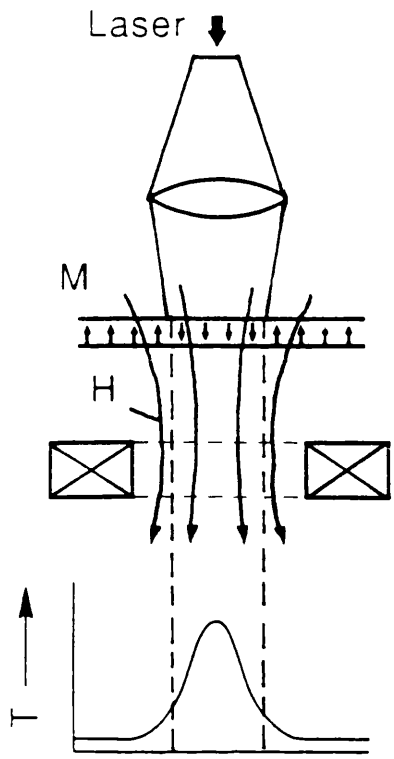

Figure 1.2 Schematic of thermomagnetic writing process. A laser generates a temperature profile in the perpendicularly magnetised layer and the magnetisation direction is reversed locally by the application of a magnetic field.

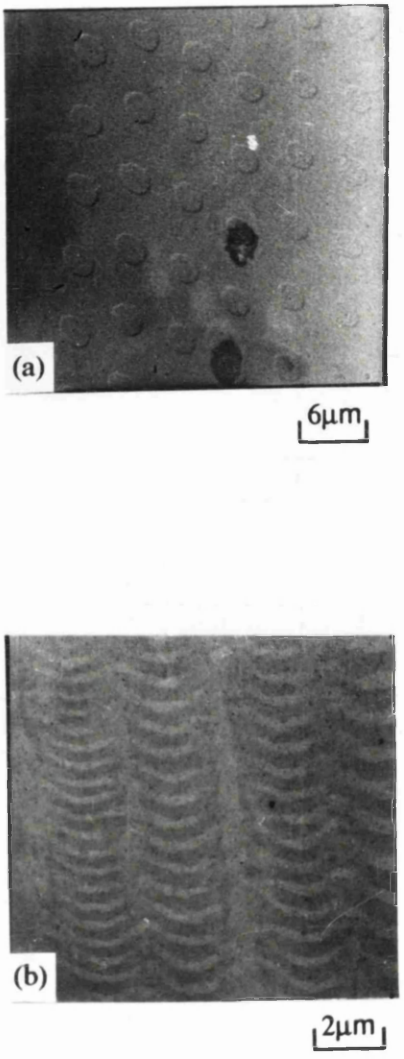

Figure 1.3 Lorentz images of thermomagnetically written marks in an MO media, produced by (a) laser modulation and (b) magnetic field modulation.

suggested that the magnetic field should be modulated, while the laser is left on continuously. This mode of writing is called magnetic field modulation (MFM) (Aeschlimann et al 1990). In this way new information is easily overwritten. An added bonus is that the domains of opposite polarity now overlap, leaving only crescents with much smaller dimensions (0.25μm) than previously (figure 1.3(b)). The quality of the recorded signal is improved since the laser is permanently on, insuring its thermal history plays no part. However the technique does require a special magnetic head that can switch fields at very high frequencies, from reasonably great distances, thus reducing the possibility of head crashes.

1.2.2 Read-out and the polar Kerr effect

The principle of magneto-optical read-out is based upon a discovery first made by Faraday (1846). He observed that when a linearly polarised beam of light passed through a fluid sitting in a strong magnetic field the plane of polarisation of the resultant beam changed.

The same principle can be applied to the reflection of polarised light from a magnetic surface (Kerr 1877) and is known as the Kerr effect. In the recording set-up, the laser power is first reduced below the threshold for writing, the laser scans the surface and when the polarised beam is reflected from a written domain within the magnetic specimen, its plane of polarisation is rotated through an angle θ_k, known as the Kerr rotation angle (figure 1.4). This effect is called the magneto-optical Kerr effect (MOKE). The direction of rotation is dependent upon whether the written domain has its magnetisation parallel or anti-parallel to the incident beam. For a detailed explanation of the Kerr effect and its implementation in MO recording see chapter 2 in the thesis by Zeper (1991).

The recording system must be supplied with a polarisation sensitive optical head to detect the rotation. Current materials of interest for M-O recording have $\theta_k \approx 0.2\text{-}0.4°$. This value gives rise to small signals, but if noise contributions can be reduced then a good carrier to noise ratio (CNR) may be achieved. For

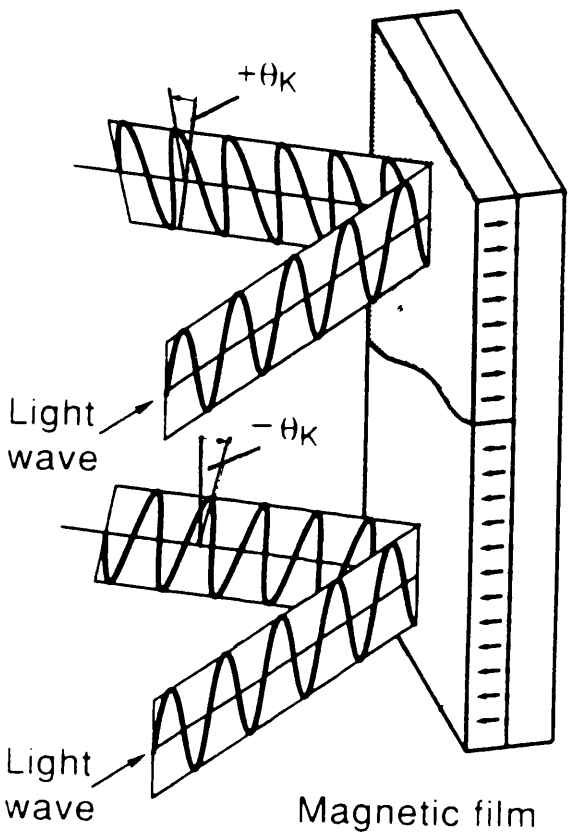

Figure 1.4 Schematic of magneto-optical read-out. The direction of the magnetisation is detected by the rotation of the plane polarised light wave over an angle θ_k

MO recording purposes a minimum CNR of 45dB must be achieved (Zeper 1991). Much research is centred upon reaching and improving upon this figure. The carrier level is proportional to the MO figure of merit, which is defined as $R\theta_k^2$, where R is the reflectivity of the material and θ_k is the Kerr rotation. Therefore the CNR may be increased by choosing a film composition which yields a large Kerr rotation. By the introduction of enhancement layers, deposited before the recording medium, the figure of merit can be increased greatly. However it has been established that by doubling the Kerr rotation only results in an increase of 6dB to the CNR, which is quite small with respect to the noise contribution. It is therefore more common to attempt to reduce sources of noise. There are two forms of noise in MO recording; media noise is defined as the difference in noise present when the disc is rotating or not, whilst write noise is due to imperfections in the thermomagnetically written domains. The microstructure of the film is an important consideration in the former, as noise is caused by inhomogeneities.

1.2.3 Materials for M-O recording

The basic requirement for any material to be considered as a future MO recording media is the ability to sustain a perpendicular magnetic anisotropy. As well as this consideration, the material must have: (a) a high MO figure of merit $R\theta_k^2$; (b) high room temperature coercivity H_c, to prevent any unwanted writing taking place; (c) 100% remanence, since anything less will reduce signal and cause write noise due to the medium having reversed magnetic polarisation; (d) good material homogeneity to reduce crystal boundaries resulting in lower media noise and higher CNR; (e) switching characteristics compatible with existing laser powers and magnetic fields and (f) good long term stability. These restrictions greatly limit the classes of materials that are suited to MO recording.

Although the magneto-optical effect has been known about and researched for thirty years (Chang et al 1965), a major breakthrough was not made until Chaudhari et al (1973) discovered uniaxial magnetic anisotropy in

amorphous Gd-Co and related compounds. This research led to commercially available MO recording media. The most common of these rare-earth transition metal (RE-TM) compounds are: GdTbFe and CoTbFe (Connel et al 1982, Ichihara et al 1988, Greidanus et al 1989). For such films the perpendicular magnetic anisotropy is achieved by proper deposition conditions and they have a large room temperature coercivity (>400kA.m^{-1}). RE-TM alloys, prepared for MO recording, are amorphous and consequentially low media noise is achieved. However they are not chemically stable, being highly susceptible to oxidation and corrosion. This necessitates the need for protective layers, which can encumber manufacture of the discs. Also their Kerr rotation is moderate (0.2-0.4° at λ=800nm) and further reduces at lower wavelengths, thus decreasing the possibility of future higher density storage of information.

These problems have motivated the continuing search for more suitable MO recording media and following the discovery of perpendicular magnetic anisotropy in artificial multilayer systems of cobalt (Carcia et al 1985), a new class of material has been investigated: cobalt platinum multilayers (Co/Pt ML). Continued research since has shown that these multilayers meet most the MO requirements made of them.

1.3 Cobalt-Platinum multilayers (Co/Pt ML) as a M-O recording media

Artificial layered structures with ultra thin layers of cobalt and platinum are extremely attractive candidates for future M-O recording media (Ochiai et al 1989, Zeper et al 1989, Lin and Do 1990, Carcia and Zeper 1990) for a number of reasons. The constituent metals are chemically stable, and highly resistive to oxidation and corrosion. Therefore protective layers are not required to enhance operating lifetimes and manufacture is made easier. They can be deposited simply at room temperature by either electron-beam evaporation or sputtering. So far the best recording results have been achieved on evaporated Co/Pt multilayer discs (Zeper et al 1989).

1.3.1 Magnetic and M-O properties of the multilayers

The individual metal layer and the total multilayer thicknesses are critically important with regards to the magnetic properties of the system. Carcia (1988) discovered perpendicular magnetic anisotropy in Co/Pt ML for cobalt thicknesses T_{Co}<8Å. Above this thickness of cobalt, the easy axis of magnetisation lies in plane because the magnetic anisotropy cannot overcome the demagnetising field of the film. The perpendicular anisotropy is thought to arise from interfacial contributions (Zeper et al 1989), although the exact nature of this is still debated. This together with 100% remanence (square hysteresis loop, as shown in figure 1.5) is found in ML's with T_{Co} < 4Å and platinum thicknesses T_{Pt} between approximately 8-20Å. The hysteresis loops become more sheared if the cobalt layers are thicker. A multilayer of overall thickness 30nm, whose bilayer is in the composition range, has perpendicular magnetic anisotropy and a room temperature coercivity of 100-150 $kA.m^{-1}$. This value is much lower than the coercivity range (>400$kA.m^{-1}$) found in RE-TM alloys, but may be increased by depositing the film directly onto an appropriate underlayer (Zeper et al 1990). The magnetisation $\underline{M}$, and Kerr rotation θ_k, are directly proportional to the Co:Pt ratio, while the Curie temperature decreases for thicker platinum layers (this is due to the cobalt layers being magnetically coupled through the platinum). Thus a compromise has to be made between the magnetic and MO properties: the platinum thickness should be as thin as is compatible to give a reasonable Kerr rotation with 100% remanence.

Co/Pt multilayer discs have smaller Kerr rotations at 800nm (0.1-0.2°) than their RE-TM counterparts; however their recording performance (53dB) is comparable with GdTbFe disks despite the highly polycrystalline nature of these films which results in higher media noise levels. This is due mainly to the high reflectivity of Co/Pt. As stated previously the typical bit size while recording at 800nm is 1μm. This dimension decreases with decreasing wavelength; thus higher storage densities are achieved if λ is reduced to 400nm by frequency doubling. An additional advantage of recording at this wavelength with Co/Pt ML's is that their Kerr rotation increases, leading to greater carrier levels (Zeper

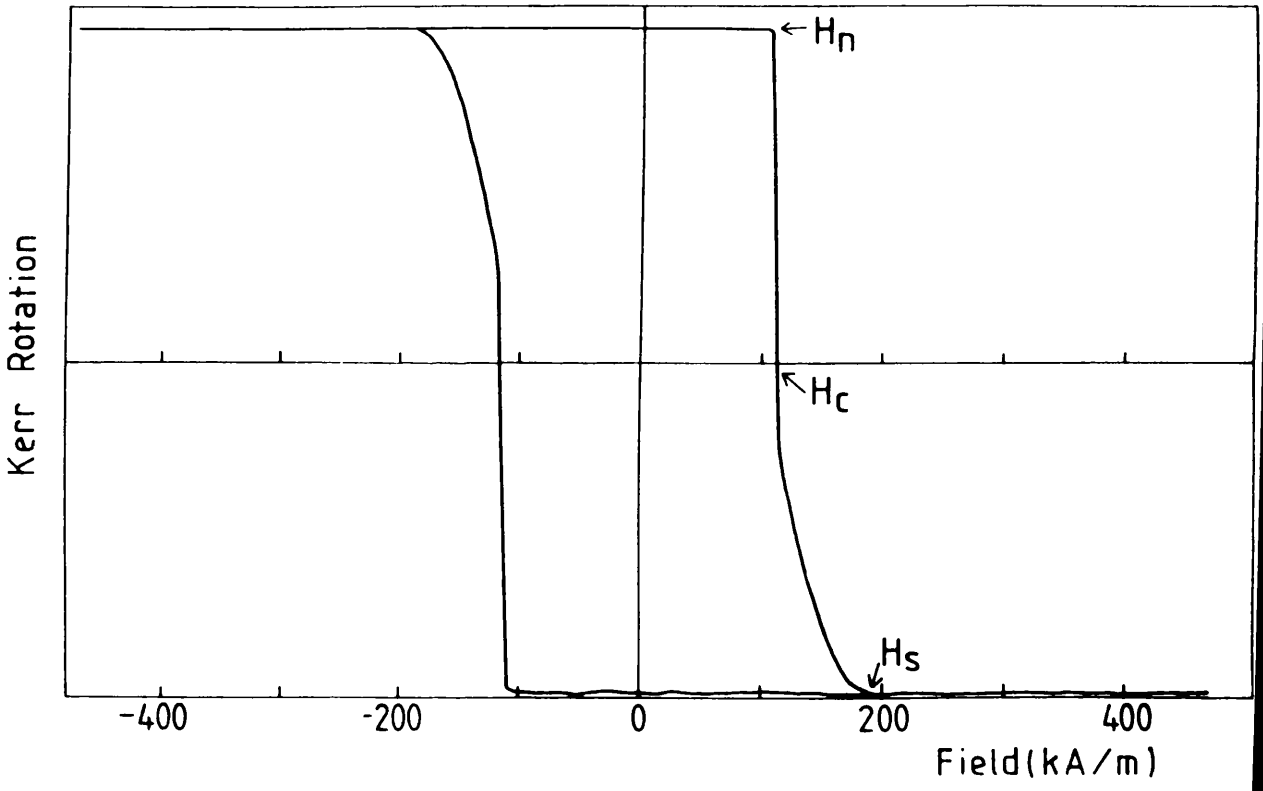

Figure 1.5 Typical square hysteresis loop measured from Co/Pt multilayers suitable for MO recording.

1991). As yet no commercial solid state lasers are available which operate at such low wavelengths, but progress is being made in that direction.

1.4 Scope of Thesis

The majority of this thesis details the microscopy (both electron and force) carried out on artificial multilayers of cobalt-platinum in the Solid State Physics group at the University of Glasgow and at Philips Research Laboratories in Eindhoven.

Chapter 2 describes in detail the instrumentation and techniques required for electron microscopy of magnetic materials. In particular it deals with the differential phase contrast (DPC) mode of Lorentz microscopy, which has been used extensively throughout this study. The characterisation and imaging of the multilayers is covered in Chapter 3. A wide range of imaging techniques were implemented and the instrumental conditions required for each are discussed along with some preliminary results. Chapter 4 includes a large body of work dealing with the in-situ magnetising of the multilayers in the HB5 STEM. During this we were interested in such phenomena as domain nucleation and switching mechanisms. All the work in the previous chapters has dealt with naturally occurring domains; however in Chapter 5 the important subject of thermomagnetically written domains is tackled in depth. Both laser modulated spots and continuous lines were studied and quantitative results achieved. An important characteristic of all magnetic thin films is their domain wall energy. In Chapter 6 we have calculated values for this energy (in Co/Pt ML) using various methods and compared these with theory. A magnetic force microscopy study of these multilayers is reported in Chapter 7 and the results (together with the technique) compared with DPC imaging.

The final results chapter (Chapter 8) moves away from Co/Pt ML and instead deals with a study of MnZn-ferrites. This involved both structural and magnetic imaging together with compositional analysis using energy dispersive x-ray (EDX) microanalysis.

Finally Chapter 9 discusses the conclusions reached from all of this work and also gives recommendations on future work that could be carried out.

Chapter 2

Electron microscopy of magnetic thin films

2.1 Introduction

This chapter deals with the experimental techniques used, throughout this study, to observe magnetic domains in thin films of interest. In particular image formation in a scanning transmission electron microscope (STEM) and the differential phase contrast (DPC) mode of Lorentz microscopy (Chapman 1984) are described extensively. Before this, however, a brief summary of other available micromagnetic observational techniques is given, followed by an explanation of image formation and Lorentz microscopy in a conventional transmission electron microscope (CTEM).

The imaging of magnetic domains is important in order to observe, quantify and better understand the magnetisation distributions that are present within ferromagnetic thin films. The first direct observation of domains was made by Bitter (1931). To do this, he coated the surface of a ferromagnetic crystal with fine ferromagnetic particles held in a colloidal suspension. These particles agglomerate in the stray field produced in regions of high magnetic field gradient, such as domain walls. The method is useful for determining domain configurations, but reveals no information on the direction of $\underline{M}$ within each domain. Imaged optically a resolution of $\approx 1\mu m$ can be achieved.

Two optical techniques are available which give quantitative information on the direction of $\underline{M}$. They rely on the polarisation plane of incident light being rotated as it is either reflected from (Kerr) or transmitted through (Faraday) a magnetic sample. This angle of rotation is directly related to $\underline{M}$. The most commonly used of the two, is the Kerr technique, in which light reflected from the surface is analysed to determine the change in the plane of polarisation of the light. The best resolution obtained with this method is 250nm (Rave et al. 1987) when a laser was used as the light source. The technique also allows

dynamic experiments to be carried out.

Better resolution is attained when an electron beam is used as the illumination source. The electron microscope is well suited to the direct study of magnetic domains within thin film materials. A wide range of interactions takes place when a beam of fast electrons is incident upon a specimen, making it possible to investigate, with high spatial resolution, the crystal and defect structure and observe the effects that they might have on the magnetic domain structure. A detailed knowledge of these properties is important if more suitable materials are to be produced for commercial and professional recording purposes. Domains may be observed in an as-grown or one of many remanent states. However, more relevant for information storage materials is the observation of written tracks in the media, in which case microscopical data may be related to those on recording performance. The first observations of magnetic domains using a transmission electron microscope was by Hale et al (1959). The domain wall contrast could be explained qualitatively by the action of the Lorentz force on the electrons as they travelled through the thin magnetic film. Therefore, this branch of electron microscopy became known as Lorentz microscopy. Lorentz microscopy may be carried out in both CTEM and STEM modes.

Another technique which uses an electron beam as its illumination source is scanning electron microscopy with polarisation analysis (SEMPA) (Celotta and Pierce 1986). This novel technique produces vector maps of surface magnetisation. Quantitative analysis of the vector magnetisation is available with a spatial resolution of 70nm. It is implemented by using a beam of focussed unpolarised electrons incident on a very clean surface of a ferromagnetic sample. This excites secondary electrons near the surface, which retain their spin-orientation as they leave the specimen. They are sent to and collected in an electron-spin polarisation analyser. The electron-spin polarisation is directly related to the magnetisation of ferromagnets. A vector map is produced by rastering the high energy beam across the sample and allowing all three components of magnetisation to be analysed without re-orientating the sample.

Finally, for observing domains there is the increasingly popular technique of

magnetic force microscopy (MFM) (Grütter et al 1988) which is described in chapter 7.

2.2 Image formation in a CTEM

In a standard CTEM, electrons are emitted (under high vacuum) from either a heated tungsten or lanthanum-hexaboride (LaB_6) filament which is held at a high negative potential. They are accelerated towards a grounded anode and form a cross-over (accelerating voltages can be in the range of 40-400kV). Between the anode and the specimen is the condenser system, which in most modern microscopes consists of two lenses and an appropriate aperture. These lenses control the effective size of the source and the angular convergence of the electrons at the specimen plane to suit the type of specimen being investigated and the magnification used. The main imaging lens is the objective lens, which focusses the electron beam to produce a diffraction pattern in the vicinity of the back focal plane (bfp) of the lens. It also determines the final resolution of the microscope. The projector lenses transfer the final image to the viewing screen. The image may then be observed on the viewing screen or, using a low light level TV camera viewed on a monitor. Permanent images are recorded on photographic film or video tape.

2.2.1 Bright field (BF) imaging and selected area diffraction (SAD).

Standard in-focus bright field images are obtained in a CTEM when the viewing screen is conjugate to the specimen plane. The contrast seen in the final image arises from amplitude and phase modulation contributions. The former arises from the removal of part of the scattered beam by an appropriate objective aperture, while the later arises from interference of the incident and scattered beams at the image point.

In crystalline materials, Bragg reflections in the beam occur when atom planes lie nearly parallel to the beam. All electrons scattered through the same Bragg reflection angle reach the bfp of the objective lens at the same radial position.

Therefore a map of lattice points in reciprocal space is generated. A perfect single crystal will result in a regular array of spots, while in polycrystalline materials, concentric rings are obtained. The latter case occurs because the diffraction pattern is the sum of the individual patterns from each grain in the material. By adjusting the projector lens settings, the viewing screen can be made conjugate to the focal plane of the objective lens and the diffraction pattern may be observed. With the camera length known the pattern can be analysed and the crystal structure of the specimen found.

2.3 Lorentz microscopy

2.3.1 Electron beam-specimen interaction

As a beam of fast electrons impinges upon a uniform magnetic film, it is deflected as shown in figure 2.1. The sense of this deflection depends on the direction of induction within each domain and is defined as

$$\beta_x = \frac{e\lambda}{h}\int_{-\infty}^{\infty} B_y(x,y,z)\,dz \qquad (2.1)$$

where B_y is the saturation induction, e is the electronic charge, λ is the electron wavelength and h is Planck's constant. For 100kV electrons incident upon a typical thin magnetic film (as shown in figure 2.1) of 50nm thickness and saturation induction of 1T, a Lorentz deflection of ≈0.06mrad results, which is small enough not to be confused with the Bragg scattering angle (typically 10^{-2}rad). However the magnetic content of the multilayers studied throughout this thesis is very small (in the region of 4nm) and in addition they have perpendicular magnetic anisotropy. This greatly reduces the angle through which the beam is deflected and typically an angle of 2μrad is achieved.

Quantum mechanically, the electron beam-specimen interaction can be understood in terms of the Aharonov and Bohm effect (Aharonov and Bohm 1959). They showed that the effect of magnetic induction was to introduce a phase shift between two electron rays which originated from the same point and rejoined after travelling different paths of the same length, which enclosed a

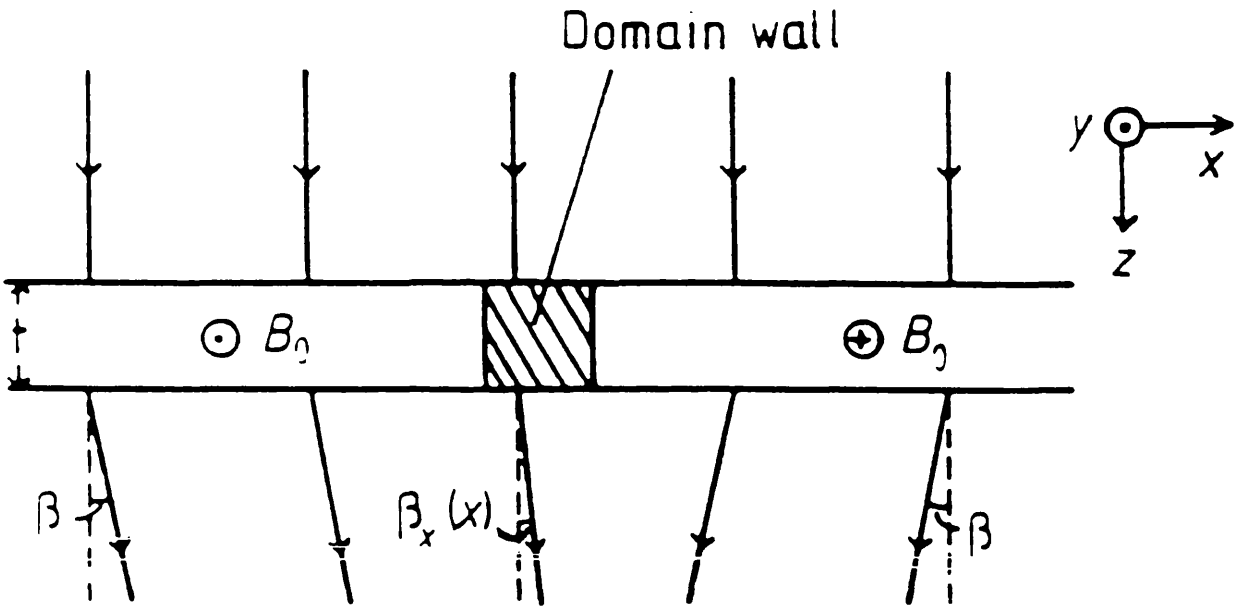

Figure 2.1 Definition of deflection angle for electrons passing through a thin film magnetic object.

magnetic flux N. The phase shift is given by:

$$\phi = \frac{2\pi eN}{h} \tag{2.2}$$

where h is Planck's constant.

In the case of a plane electron wave travelling in the z-direction and incident on a magnetic specimen (as shown in figure 2.1), the phase shift between any two points x_1 and x_2 will be:

$$\phi(x_2 - x_1) = \frac{2\pi et}{h} \int_{x1}^{x2} B_y(x,y,z)\, dx \tag{2.3}$$

Thus ferromagnetic specimens act as pure phase objects to an electron beam and therefore, Lorentz microscopy is a branch of phase contrast microscopy.

2.3.2 Lorentz microscopy in a CTEM

There are two available modes of Lorentz microscopy for a CTEM and these are discussed classically below. The Fresnel mode is best described with reference to figure 2.2. The main imaging lens is defocussed so that at a distance Δz from the specimen, the object plane is no longer coincident with it. The contrast in the image arises where there is a varying component of magnetic induction, such as at domain walls. These are delineated as narrow bright or dark bands corresponding to either a diverging or converging electron beam. There is no contrast from the domain interior, therefore, Fresnel imaging reveals no direct information on the direction of magnetisation within each domain. The advantages of using this mode are its operational simplicity, together with high contrast levels. However drawbacks also exist; since the scattered intensity is not linearly proportional to the induction, this is a non-linear mode, making any quantitative analysis very difficult.

Foucault Lorentz microscopy is shown schematically in figure 2.3. In this mode, magnetic contrast is generated by obscuring part of the diffraction pattern

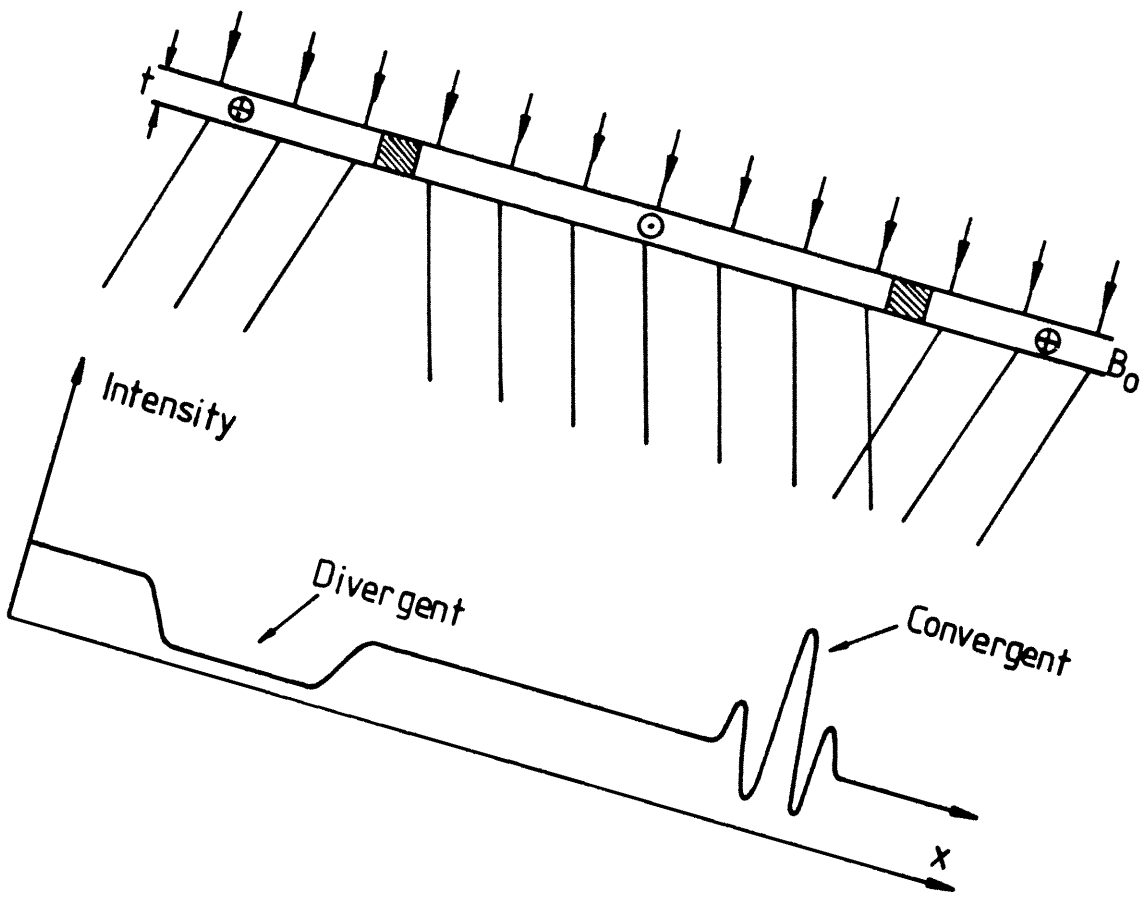

Figure 2.2 Schematic of magnetic contrast generation in the Fresnel mode of Lorentz microscopy.

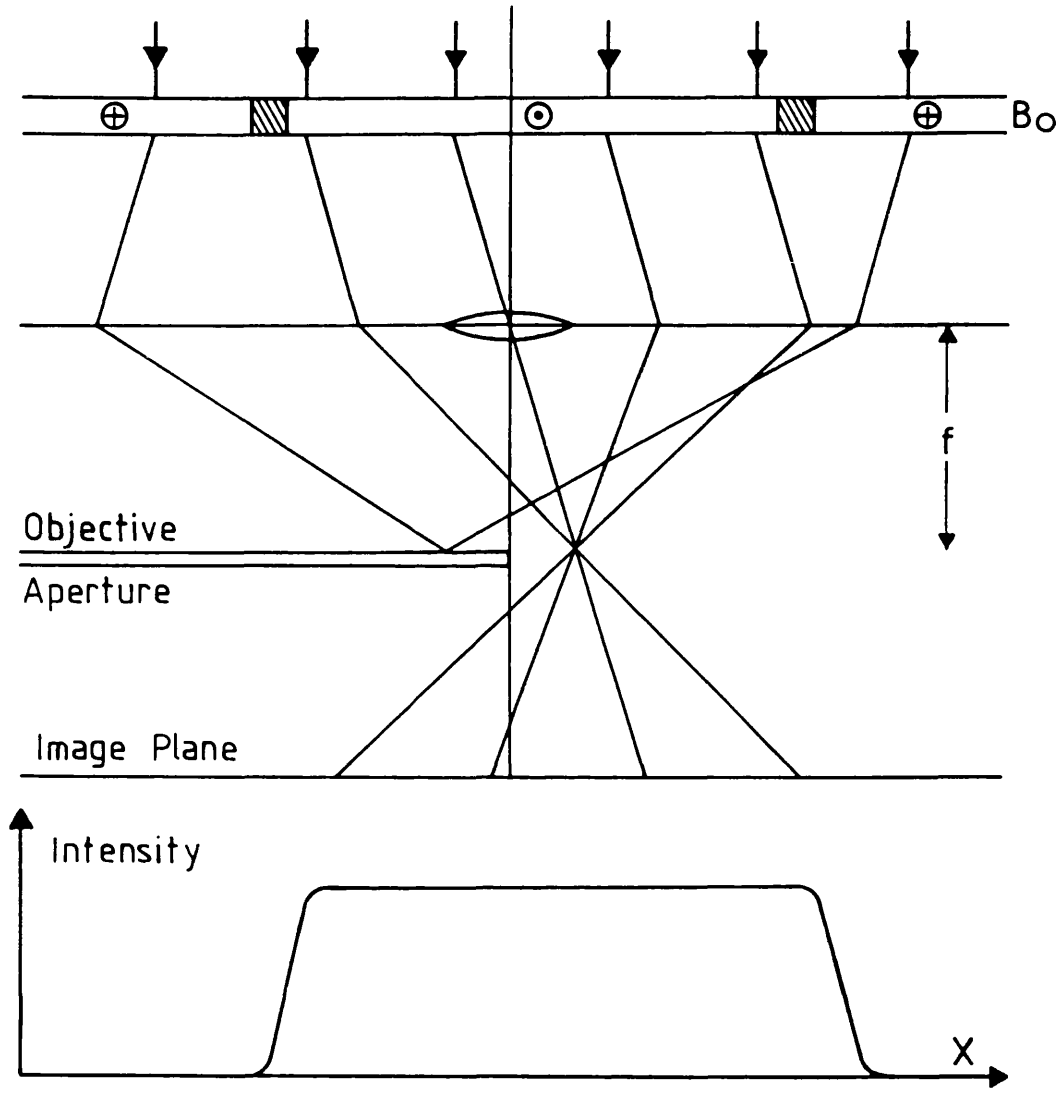

Figure 2.3 Schematic of magnetic contrast generation in the Foucault mode of Lorentz microscopy.

with an off-centred aperture. The aperture allows electrons, deflected in a particular sense to contribute to the image, whilst all others are blocked leading to image areas with zero intensity. By careful manipulation of the displaced aperture, domains whose magnetisation lies in a selected direction may be viewed as areas of high intensity. Usually, in practice, two images of each area are taken, mapping induction parallel to two orthogonal axes. Again Foucault microscopy is simple to implement. In contrast to Fresnel it gives the operator control over the preferred direction of mapping of the induction and is an in focus technique. However it is again a highly non-linear mode, ill suited to most quantitative image analysis. Also, the manual positioning of the displaced aperture makes reproducibility a problem. Thus, although it is difficult to obtain detailed quantitative information from these two modes, they complement each other and give a good qualitative description of the magnetic microstructure.

All the CTEM Lorentz microscopy was carried out on a modified JEOL 2000FX CTEM at the University of Glasgow. This microscope, operated at an accelerating voltage of 200kV, has been modified for the study of magnetic materials. Its significant advantage over standard CTEM's is the type of objective lens used, which is similar in design to that described by Tsuno (1983). Under standard operating conditions the specimen sits in virtually field free space, thus the domain structure of the material in question is not affected. The objective aperture is now situated exactly in the diffraction pattern of the objective lens and this enables Foucault imaging to be conducted.

2.3.3 Lorentz microscopy in a STEM

The way in which images are formed in a STEM differs greatly from those in a CTEM. In a STEM a small focussed probe is scanned in a regular raster across the specimen and some portion of the scattered or unscattered beam is detected. Thus each pixel in the final image is acquired sequentially, in contrast to image formation in a CTEM where the whole image is formed simultaneously.

The mode of Lorentz microscopy which can be implemented in a STEM is

called differential phase contrast microscopy (DPC), which was first discussed by Dekkers and de Lang (1974) and applied to magnetic films by Chapman et al (1979)

The image contrast relating to the magnetic structure of a specimen, in this mode is easily explained classically with the aid of figure 2.4. A small focussed probe of electrons, incident upon a magnetic specimen, is scanned across its surface. As it passes through, it is deflected by the local Lorentz deflection angle, defined by equation (2.1). The electron beam then passes descan coils before being projected onto the detector by a series of post specimen lenses. The purpose of the descan coils is to ensure that, in the absence of any specimen, equal currents fall on each quadrant of the detector. This is no longer the case when a magnetic specimen is present, which in this instance is assumed to be one dimensional. The beam has now experienced a deflection β_x. If this deflection is small compared to the probe semi-angle α, then the difference in currents from two opposite quadrants of the detector is directly proportional to β_x. Thus this difference signal, which forms the DPC image provides a direct measure of the local deflection angle which in turn is directly proportional to the in-plane induction of the specimen $B_y(x)$.

Although it is clearly possible to understand DPC microscopy in classical terms, if quantitative results are desired then a more rigorous quantum mechanical approach involving image formation and beam-specimen interaction must be taken. Such an approach, for a magnetic specimen, is taken in the following section.

2.4 Wave-optical image formation in a STEM

The electron wavefunction incident on a specimen $\psi_o(\underline{r})$, in a STEM can be expressed as a Fourier transform of the wavefunction at the probe forming aperture $\Psi_o(\underline{k})$, which is defined as:

$$\Psi_o(\underline{k}) = A(\underline{k})\exp[i\chi(\underline{k})] \qquad (2.4)$$

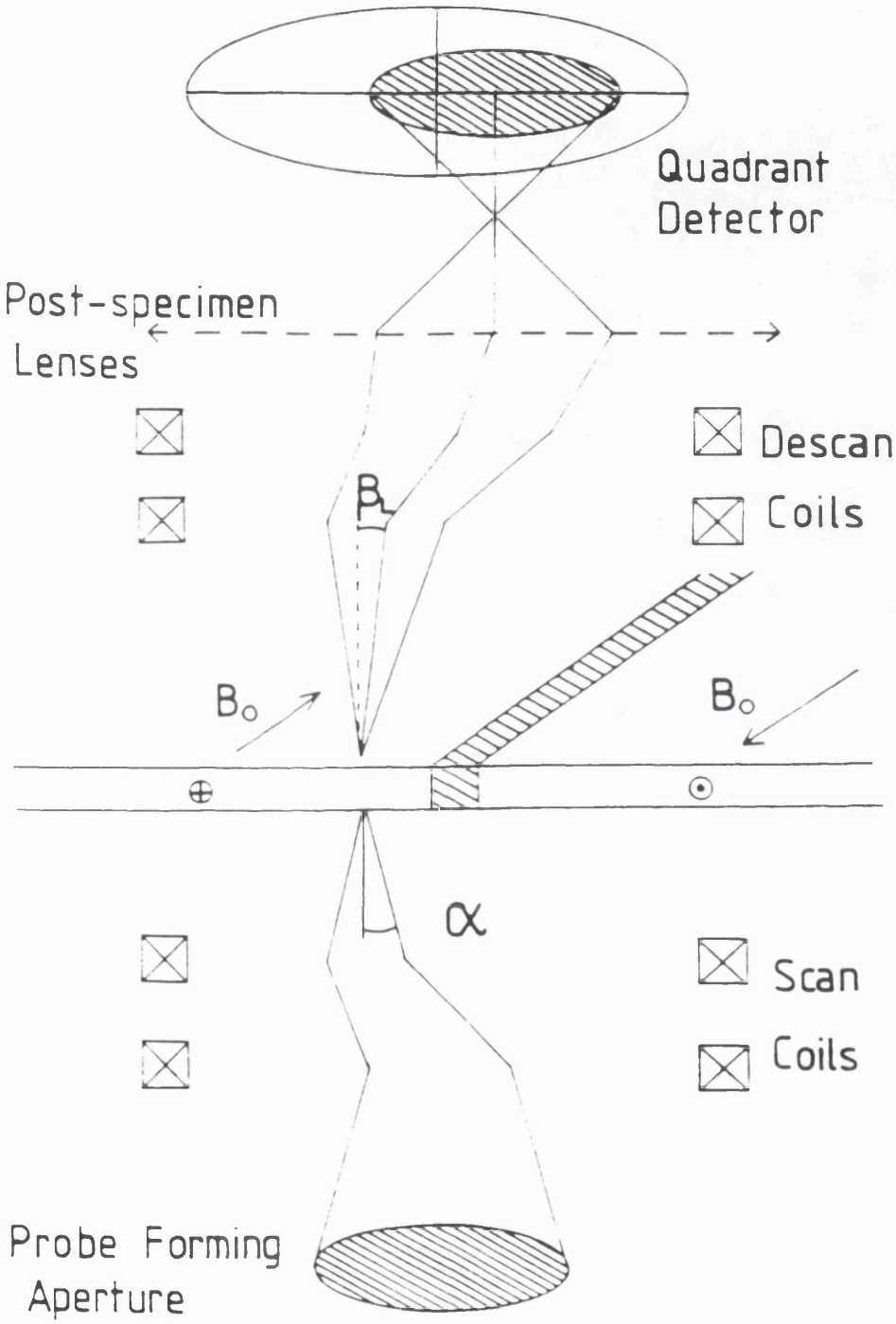

Figure 2.4 Schematic of magnetic contrast generation in the Foucault mode of Lorentz microscopy.

where

$$\chi(\underline{k}) = -2\pi\left[-\frac{C_s\lambda^3k^4}{4} - \frac{\Delta z\lambda k^2}{2}\right] \tag{2.5}$$

In the above A($\underline{k}$) is a pupil function defining the probe aperture function as 1 inside the aperture and 0 elsewhere, C_s is the third order spherical abberation coefficient of the lens and Δz is a defocus term of the probe forming lens. Therefore, as stated above:

$$\psi_o(\underline{r}) = FT[\Psi_o(\underline{k})] \tag{2.6}$$

In all these equations, $\underline{r}$ is a position vector in the plane of the specimen, $\underline{k}$ is a position vector in reciprocal space and FT denotes a Fourier transform of the function within the brackets.

The electron-specimen interaction may be expressed in terms of a transmission function which defines how the electron wavefunction is modulated by the specimen. For a magnetic specimen this may be given as:

$$h(\underline{r}) = \exp[-i\phi(\underline{r})] \tag{2.7}$$

where $\phi(\underline{r})$ denotes the change in phase of the electron wave due to the specimen.

Following transmission, the electron wavefunction on exit is then given by:

$$\psi(\underline{r},\underline{r}_o) = h(\underline{r})\psi(\underline{r}-\underline{r}_o) \tag{2.8}$$

where $\underline{r}_o$ is a position vector upon which the electron probe is centred.

On arriving at the detector, which is sited in the far field, the electron wavefunction is simply given as the Fourier transform of equation (2.8).

$$\psi_d(\underline{k},\underline{r}_o) = FT[\psi(\underline{r},\underline{r}_o)] \tag{2.9}$$

The signal intensity at the detector plane is given by the modulus squared of equation (2.9) and thus can be expressed as:

$$I_d(\underline{k},\underline{r}_o) = \left|\psi(\underline{k},\underline{r}_o)\right|^2 \qquad (2.10)$$

It is necessary to evaluate equation (2.10) for a detector with a suitable response function R($\underline{k}$). The recorded signal on the detector is given by:

$$J(\underline{r}_o) = \int I_d(\underline{k},\underline{r}_o).R(\underline{k})\,d\underline{k} \qquad (2.11)$$

For a split detector (a possible configuration of a quadrant detector), then R($\underline{k}$) is defined as:

$$R(\underline{k}) = 1 \quad for \quad k_x>0 \qquad (2.12)$$

$$-1 \quad for \quad k_x<0$$

Such a response function is antisymmetric. Detailed analysis (Waddell and Chapman 1979, Morrison 1981) has shown that for realistic experimental conditions, J($\underline{r}_o$) with R as in equation (2.12) is, to an excellent approximation, linearly related to $d\phi/dx$ for a pure phase object. Therefore, in general, the image signal is linearly related to phase gradients. From equation (2.3) it follows that for a ferromagnetic specimen:

$$\nabla_x\phi(x,y) = \frac{2\pi e t\overline{B_y}}{h}, \qquad \nabla_y\phi(x,y) = \frac{-2\pi e t\overline{B_x}}{h} \qquad (2.13)$$

This confirms that for an ideal DPC detector the classical result holds. As well as difference images revealing magnetic contrast, it is possible to sum the signals from all four quadrants. Such an arrangement gives an incoherent bright field image, revealing microstructural contrast.

2.4.1 Modified DPC imaging

The previous section has shown that in the idealised situation, DPC microscopy

can yield quantitative maps of in-plane induction. However, in practice inherent problems do exist: as in all modes of TEM, contrast arising from non-magnetic sources is present simultaneously. One such source, in polycrystalline materials is the crystallites of which the film is composed. These can make detailed interpretation of the image difficult, and in unfavourable circumstances may conceal the magnetic detail which is of primary interest. Thus a more correct expression for one of the signals in DPC imaging is given by:

$$\nabla_x \phi(x,y) = \frac{2\pi e}{h} \int B_y(x,y,z)dz + \frac{\pi \nabla_x [t(x,y)V(x,y)]}{\lambda E_o} \qquad (2.14)$$

where ϕ is the total phase shift introduced by the specimen. In the above expression, the two terms arise from separate magnetic and electrostatic potentials. The first term corresponds to the ideal situation, where the final image contrast is only magnetic in origin, as discussed in the previous section. The second term is electrostatic in origin and is important when there is a change in the thickness of the film t, or in its inner potential V. For polycrystalline films, the largest contribution to this term is from the crystal grain boundaries where the phase function changes quasi-discontinuously.

An alleviation to this problem (though not a total solution) is found by noting that the scale of the magnetic induction which we wish to map is usually much greater than that of the crystallite boundaries. Thus there is a marked difference in the respective power spectra of the two components. It is this difference that is exploited by making a modification to the detector geometry, so that a detector similar to that shown in figure 2.5 is now used. This modification allows a high degree of control over the relative efficiencies with which low and high spatial frequency information can be transferred from the specimen to the image. A simple physical argument is used below, but a full wave-optical discussion of the imaging properties when using such a detector is given by Chapman et al (1990).

When an electron beam passes through a magnetic specimen, the induction introduces a shift in the position of the bright field (BF) cone on the detector

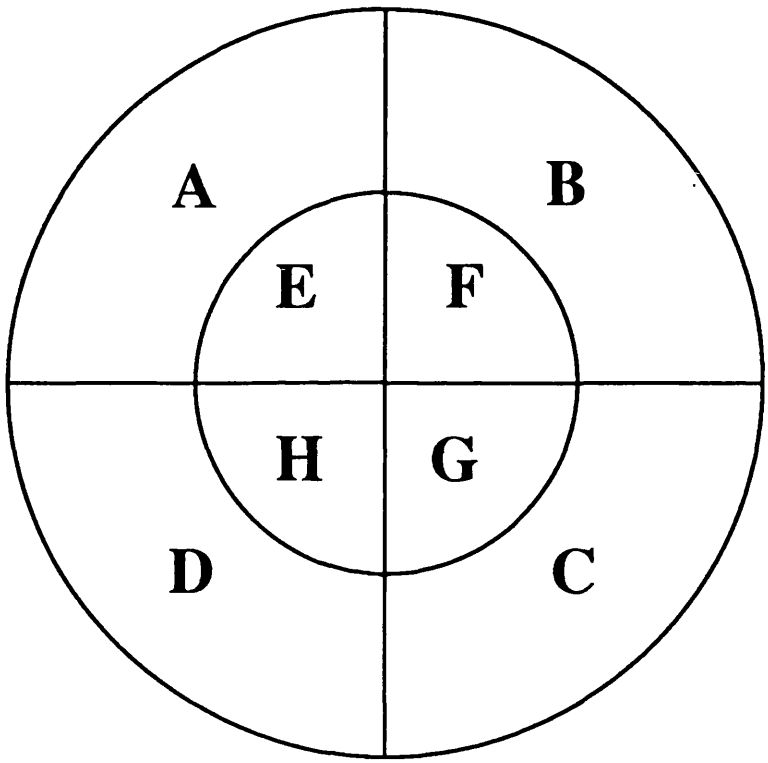

Figure 2.5 Schematic of detector geometry necessary to implement modified DPC Lorentz microscopy.

due to the Lorentz deflection. By taking difference images from only the outer annulus of the detector (eg A-C), the signal arises from electrons at the periphery of the BF cone and is now only sensitive to its position on the detector and not to intensity modulations within it. The signal pertaining to information on the crystallites falls in the mid to high frequency range. Intensity modulations within the BF cone which do not shift its position are created by interference of the BF and diffracted cones. Thus this signal can be collected using only the inner quadrants.

By introducing an eight segment detector, it is now possible to separate substantially low (magnetic) and high (non-magnetic) frequency components and display them simultaneously in separate images. This allows finer magnetic detail to be observed than was previously possible. Experimentally, the most important consideration is the ratio of the inner annulus K_i of the detector relative to that of the BF cone K_α and this is denoted by κ. The camera length must be manipulated (by varying the excitation of the post specimen lenses) such that a non zero signal falls on the outer annulus. Figure 2.6 (from Chapman et al 1990) clearly shows the advantage which can be obtained by using an annulus detector. At low spatial frequencies the signal to noise ratio is enhanced, whilst in the mid-band it is significantly suppressed, leading to an overall improvement compared to the solid detector. In some films, such as cobalt platinum multilayers, there is severe non-magnetic scattering from the platinum layers. In such cases κ must be close to unity.

2.5 Instrumental considerations for DPC imaging

2.5.1 VG HB5 STEM

This section deals with the instrumental requirements to implement DPC microscopy in a STEM. All the work was carried out on a VG HB5 STEM at the University of Glasgow. A schematic of this microscope is shown in figure 2.7. It has been extended and modified to allow a complete range of imaging

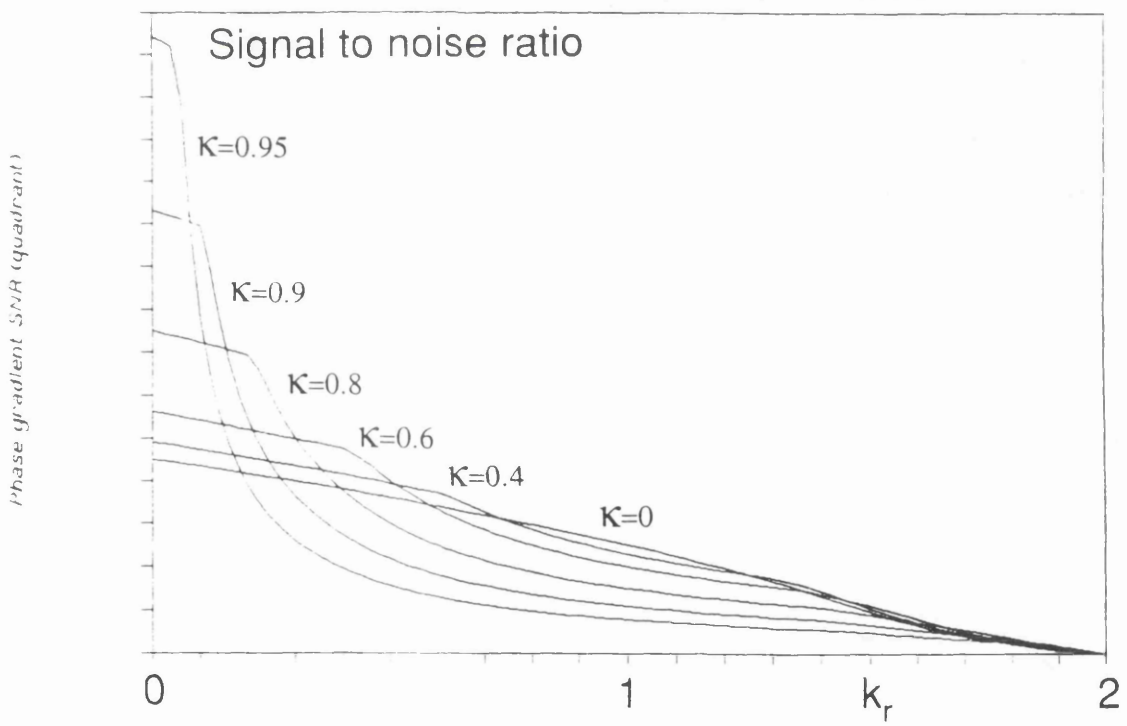

Figure 2.6 Variation of the signal to noise ratio with reduced spatial frequency for detectors with different values of κ.

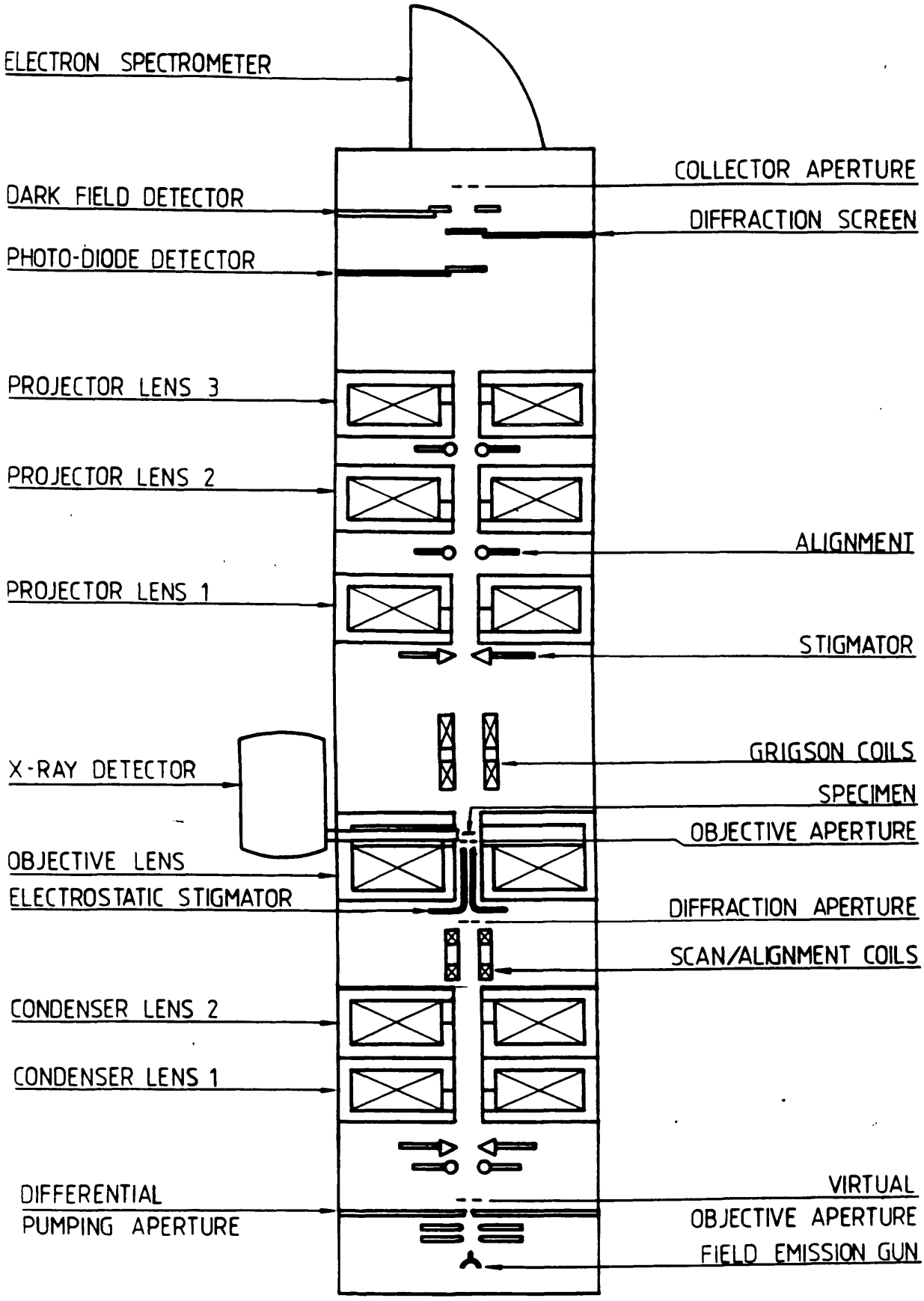

Figure 2.7 Schematic showing various components of VG HB5 STEM.

and analytical techniques to be implemented, in particular DPC microscopy.

A high brightness electron source is required for DPC imaging. The electron source in the HB5 microscope is a field emission gun (Crewe 1971), which consists of a single crystal tungsten wire (radius 100nm) held at a negative potential of ≈3kV with respect to the extraction anode. This creates an electric field of $>5x10^9$ Vm^{-1} which produces tunnelling emission of electrons. A second anode accelerates the electrons through 100kV. This configuration of electrodes has the effect of an electrostatic lens and the electrons appear to originate from a virtual source of ≈6.5nm diameter.

The specimen is illuminated by a system of three independent lenses; two condenser lenses C1 and C2, plus an objective lens. These three lenses give flexibility in the probe forming optics, dependent on the imaging mode and specimen in question. In normal mode a single condenser together with the objective may produce a focussed electron probe of <1nm diameter. However, to achieve such a small probe size the specimen must be immersed in the magnetic field of the objective lens (≈0.8T) which would destroy the domain structure in most films of interest. Therefore, for suitable magnetic domain imaging with DPC, two alternative modes of operation can be used. The first makes use of a special specimen cartridge which raises the height of the specimen by ≈10mm. With the objective weakly excited, it is then possible to obtain probe diameters of ≈2nm. The main disadvantage of this mode is that it does not allow tilting of the specimen. For that reason, the other mode of operation has been used throughout this study. Here, the specimen is situated in its normal position and the objective lens is simply switched off so that the probe is formed by a single condenser lens. The smallest probe diameters now available are ≈10nm, which although much greater than the 2nm achieved with the other mode are sufficient for most ferromagnet films of interest.

In this mode, the condenser lens forms a demagnified image of the source on the specimen and the probe angle is defined by the selected area aperture (SAA). Morrison (1981) calculated probe angles and sizes for a number of configurations. The optimum probe semi-angle α_o is defined as:

$$\alpha_o = \left(\frac{4\lambda}{C_s}\right)^{\frac{1}{4}} \qquad (2.15)$$

The closest experimental conditions that gave good agreement with theory were found using C2, in conjunction with a 100μm SAA (Morrison 1981). This resulted in a value of 0.5mrad for α_o. The coherent probe size is also dependent on C_s and is defined as:

$$d_c = (C_s\lambda^3)^{\frac{1}{4}} \qquad (2.16)$$

and for C2 this is approximately equal to 10nm.

For the study of Co/Pt ML a 50μm SAA was used to define the probe. This resulted in lower current, therefore C1 was used in conjunction with the aperture to increase current levels back to normal. For these probe forming conditions, a semi-angle of 0.3mrad results. The coherent probe size d_c is ≈18nm. The incoherent probe size d_i, is found from geometrical considerations (d_i =m x 6.5nm, where m is magnification) and is equal to 5nm. The total probe size is found by summing the two quantities in quadrature and gives a resolution of <20nm for the above configuration, which is sufficient for studying magnetic domains. The probe is then scanned in a regular raster fashion across the specimen by coils situated in front of the objective lens.

After transmission through the specimen, the electron beam passes the descan coils, whose purpose was described in an earlier section (2.3). A series of post specimen lenses (PSL) then transfer the electron distribution to a detector situated in the far field with respect to the specimen. These PSL's are required to match the angular distribution of the scattered electrons to the physical dimensions of the detector in use and result in a wide range of possible camera lengths. Throughout this study the most commonly used excitations of the PSL's for optimum DPC contrast from Co/Pt ML were: P1:+6, P2:+6 and P3:+8, giving κ to be approximately 0.9.

2.5.2 Detection and image acquisition

For modified DPC microscopy an eight segment detector is used as shown in figure (2.5). The detector, which was supplied by Link Analytical, comprises two sets of four silicon p-n junction photodiodes, split into quadrants by 200μm wide inactive strips. The outer set, in the shape of an annular detector was placed on top of, but electrically isolated from, the inner set which was in the form of a standard quadrant detector. The inner and outer radii of the detector were 4 and 13mm respectively, although in normal use the latter was reduced to 8mm by a shield. This was to prevent thermal diffusely scattered electrons from dominating the signal. The electrons incident on the detector generate currents from the photodiodes. These signals were fed to eight matching pre-amplifiers, converted into voltages and routed to a mixer unit from where a wide range of signal combinations could be subsequently used to form images.

All the DPC images displayed in this work were acquired on a Link eXL digital acquisition system. This is a dedicated computer for the acquisition, processing and storage of digital electron images (and x-ray spectra). In operation, the computer overrides the video signals, diverting them from the viewing screen of the microscope, digitising them and sending them directly to its memory, from where they can be recalled for observation and analysis. Further back-up storage takes place using quarter inch data tapes. During imaging, the operator has the choice of selection over the resolution (up to 512^2 pixels), precision (up to 16bits/pixel) and pixel dwell time (usually 51μs) to be used. The eXL is an updated version of the Link AN10000 system as used by McVitie (1988) and Rogers (1990) in earlier DPC investigations. The main advantage of the eXL is that it now allows up to five images to be acquired simultaneously. The images are in perfect registration, making detailed analysis, for example, of the physical and magnetic microstructure of a single area of interest easier. The experimental time is also reduced with simultaneous acquisition. The typical acquisition time for images averaged over four frames is ≈150s.

Chapter 3

Initial studies on Co/Pt multilayers

3.1 Deposition and Characterisation

As discussed in chapter 1, there are many material systems that have been proposed as suitable future media for MO recording. The study in this thesis concentrates on one type of material and this chapter describes that work carried out on Co/Pt multilayers. The deposition and characterisation of the media are dealt with first, followed by some preliminary results taken from the electron microscopy of these multilayers.

All MO materials can be characterised by the following bulk quantities: saturation magnetisation M_s, remanent magnetisation M_r, anisotropy constant K_u, coercivity H_c, nucleation field H_n, Kerr rotation θ_k, reflection coefficient R and Curie temperature T_c. These properties may be tailored to some extent by adjusting the deposition process. In Co/Pt multilayer films, these quantities may be further modified by changing the individual Co and Pt layer thicknesses and also the overall multilayer thickness during deposition.

Co/Pt multilayers are produced by two different deposition techniques; sputtering and electron beam evaporation (vapour). Although sputtering is preferred in commercial manufacture because of superior control and reproducibility, the best MO properties have been found in vapour deposited multilayers (He et al 1991). Stronger perpendicular magnetic anisotropy is achieved due to sharper interfaces between the Co and Pt layers. A sufficiently large coercivity is also found in the vapour deposited multilayers compared with similar films sputtered in argon gas. It is possible to enhance the properties of sputtered films if other high purity gases (Kr, Xe) are used, but it is not cost effective to mass produce films in such a manner. All the multilayers investigated in this study were produced by vapour deposition and the technique

is explained below.

The vapour deposition technique is carried out at room temperature in a vacuum system. Separate Co and Pt sources are used and the pressure inside the vessel is $5x10^{-7}$mbar. The deposition rates are kept constant at a value between 0.1 and 0.2nm.s^{-1} by quartz crystal controllers, the vapour streams being interrupted alternately for pre-programmed times with mechanically driven shutters.

Usually the films are deposited onto glass or silicon substrates so that recording experiments can take place. However this creates difficulties if the film is to be investigated in an electron microscope, since the specimen must be sufficiently thin as to appear transparent to the electron beam. Consequently films should be deposited in such a manner that it is possible to separate the film from its bulk substrate. This is not always suitable for studying recording materials, since in many instances the substrate has a bearing on the magnetic properties of the film.

A technique to overcome this difficulty in specimen preparation was developed by Jacobs and Verhoven (1986) and applied to MO media by Greidanus at al (1989). They proposed a method for the preparation of a special substrate which was suitable for close imitation of the actual MO recording process, while permitting direct observation in the electron microscope. A 3in. 380μm thick Si wafer covered with a 50nm thick Si_3N_4 layer is used as the substrate. The silicon is etched to form a matrix of pyramidal holes, leaving flat Si_3N_4 membranes. The MO film can then be deposited on top of this layer by either evaporation or sputtering and recording may take place, if required. The wafer is then split into single windows which are immediately suitable for investigation in the electron microscope. Figure 3.1 shows plan and elevation views of a window with the typical dimensions marked.

In order to better understand the bulk magnetic and MO properties of the deposited multilayers, it is necessary to carry out a number of measurements which yield information on the important parameters which were listed initially. Apart from the magnetic and MO characterisation, which will be discussed in

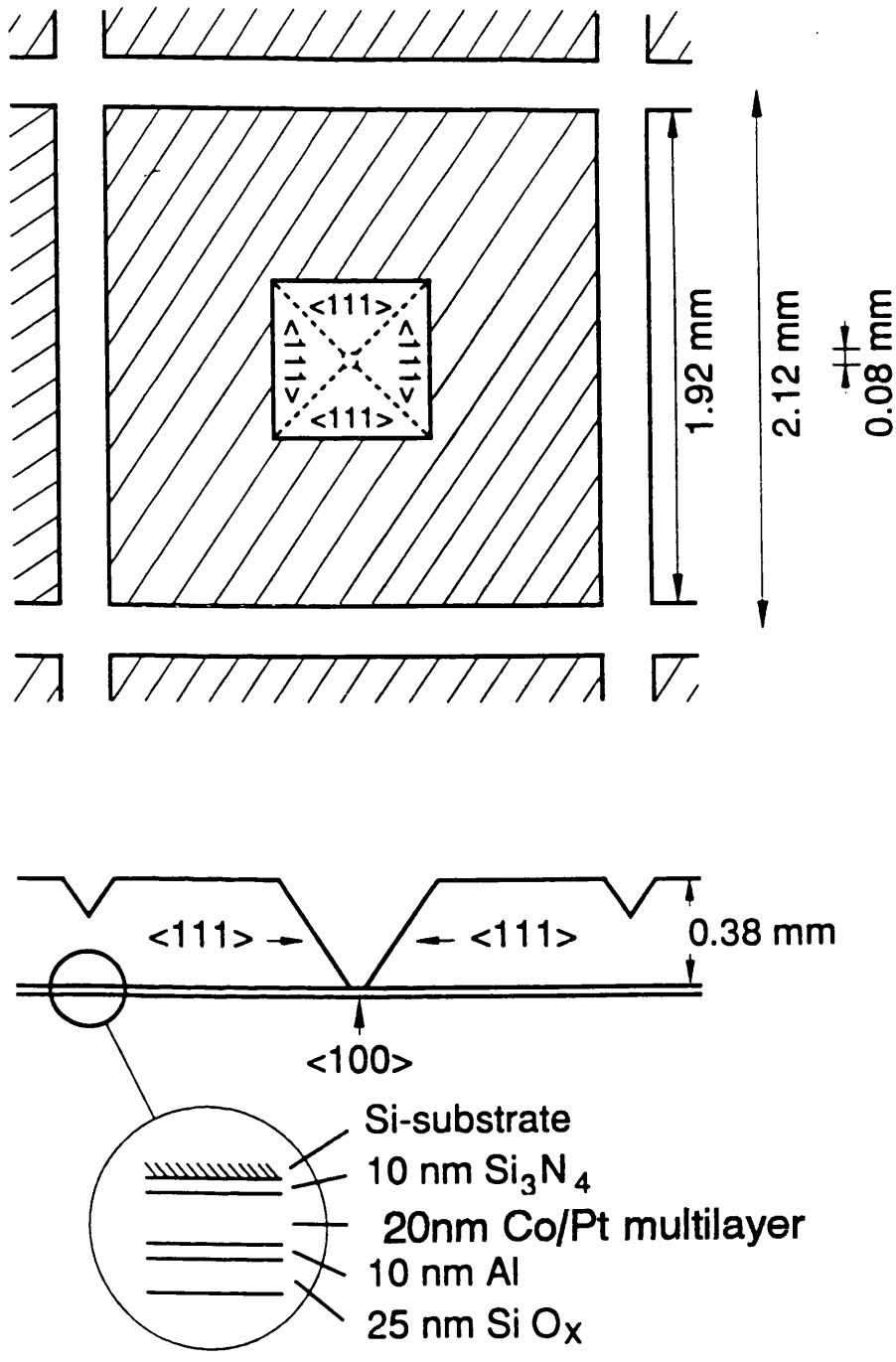

Figure 3.1 Plan and elevation views of a specially prepared Si_3N_4 membrane to enable direct observation in the electron microscope. Typical dimensions are given.

detail below, the physical structure of the multilayers is investigated. The individual metal layer thicknesses are obtained from the absolute masses of Co and Pt determined by chemical analysis. The periodic structure and any texturing within the film is analysed by x-ray diffraction.

Most of the required magnetic data can be obtained from measured hysteresis loops. The loops measure the magnetisation or Kerr rotation angle of the sample as a function of applied field. The former is most commonly measured in a vibrating sample magnetometer (VSM) (Foner 1959), although in this project hysteresis loops were also measured using an alternating gradient force magnetometer (AGFM) (Zijlstra 1970). It is also possible in the AGFM to measure additional magnetisation curves and these will be addressed more fully in the next chapter. The hysteresis measurements allow M_s, M_r, H_c, H_n and also, importantly, the shape of the loop to be determined. For a MO film with perpendicular anisotropy, the ideal hysteresis loop should have a rectangular shape, as shown in figure 3.2.

The VSM used in this project is shown schematically in figure 3.3 and was built at Philips Research Laboratories (Bernards and Schrauwen 1990). The measurement of a M-H hysteresis loop is based on the principle that a moving magnetic specimen will induce a current in coils that are placed around it. The current is proportional to the perpendicular component of magnetisation of the sample. Experimentally, the sample is held in a fixed position (either in-plane or perpendicular) between the poles of an electromagnet. The sample is vibrated at 80Hz in a vertical plane and the applied field from the electromagnet is varied. The sample magnetisation is then measured from the small detection coils. In this manner it is possible to measure volume hysteresis loops which provide a great deal of macroscopic magnetic information.

Bulk M-H loops were also measured using the AGFM at the University College of North Wales. The AGFM is a type of VSM which has at best a sensitivity of $\approx 10^{-11}$emu. The magnetometer used to measure the loops has a sensitivity of 2×10^{-8}emu, making the AGFM $\approx$1000 times more sensitive than a standard commercially built VSM. To measure the magnetisation curve, the

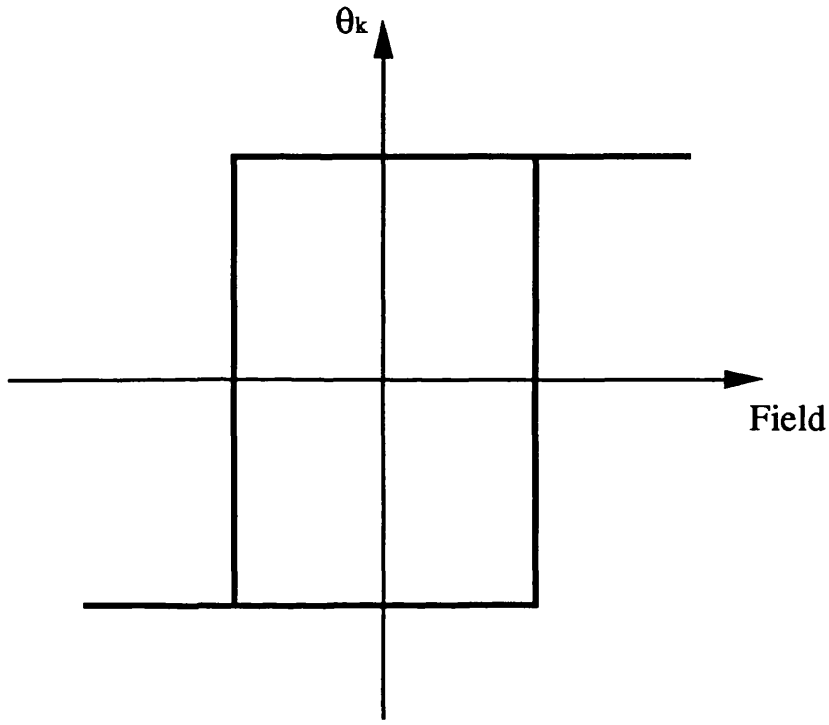

Figure 3.2 Schematic of idealised Kerr hysteresis loop for a magneto-optical material.

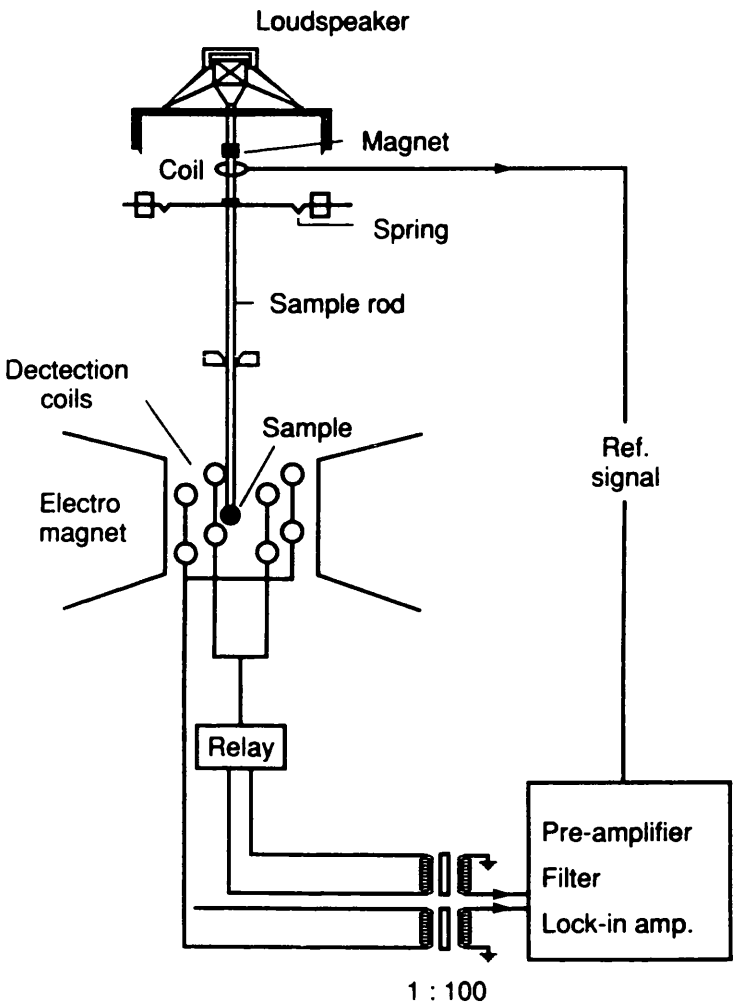

Figure 3.3 Schematic of VSM built at Philips Research Laboratories.

† The slight drop in M at high H can be attributed to experimental errors and the diamagnetic contribution from the holder not being fully compensated for

* H_n, the nucleation field is defined as the point on the loop where domain reversal from a saturated state first occurs

sample is placed at the end of a cantilever rod, which incorporates a piezoelectric element. The sample is magnetised by a dc-field and simultaneously subjected to a small alternating field gradient. This gradient leads to an alternating force on the sample which is proportional to the magnitude of the field gradient and also to the magnetic moment of the sample. The deflection of the rod is detected by the voltage output of the piezoelectric element. A complete M-H loop, corrected for the diamagnetic contribution from the specimen holder can be produced very quickly (≈100s) and with great precision. A hysteresis loop, for a multilayer of composition 9*(0.35nm Co + 1.7nm Pt), produced using this technique is shown in figure 3.4. This figure shows clearly that the M-H loop is very square, with $M_r/M_s \cong 1$ (implying 100% remanence). Although squareness is necessary for any MO recording media, it alone is not sufficient to judge whether a material is suitable, since squareness is consistent with any $H_n^* > 0$. Therefore a more appropriate parameter to characterise the hysteresis loop is the rectangular ratio defined as $r=H_n/H_c$. For an ideal MO media, r should be as close to unity as possible. The loop in figure 3.4 satisfies both criteria and therefore this film is a prospective MO media.

The surface MO Kerr loops were obtained using a spectrometer built by Zeper (1991) and of similar design to that of Sato (1981). A hysteresis loop was produced by monitoring the Kerr rotation at one wavelength (usually 530nm) and sweeping the external magnetic field. All measurements were carried out at room temperature. A typical MO loop for an Co/Pt multilayer is presented in figure 3.5 and once again it exhibits extreme squareness and rectangularity. The directionality of the loop is determined by the sign (negative in this case) of the Kerr rotation.

The most common method to measure the anisotropy constants of the multilayers was by torque magnetometry (Chickazumi 1964). The sample is held between the poles of an electromagnet in a holder suspended from a torsion wire. The torque required to hold the sample either in the plane of, or perpendicular to the applied field is measured as the magnet is rotated through 180°. From the resultant torque curves it is possible to calculate the anisotropy

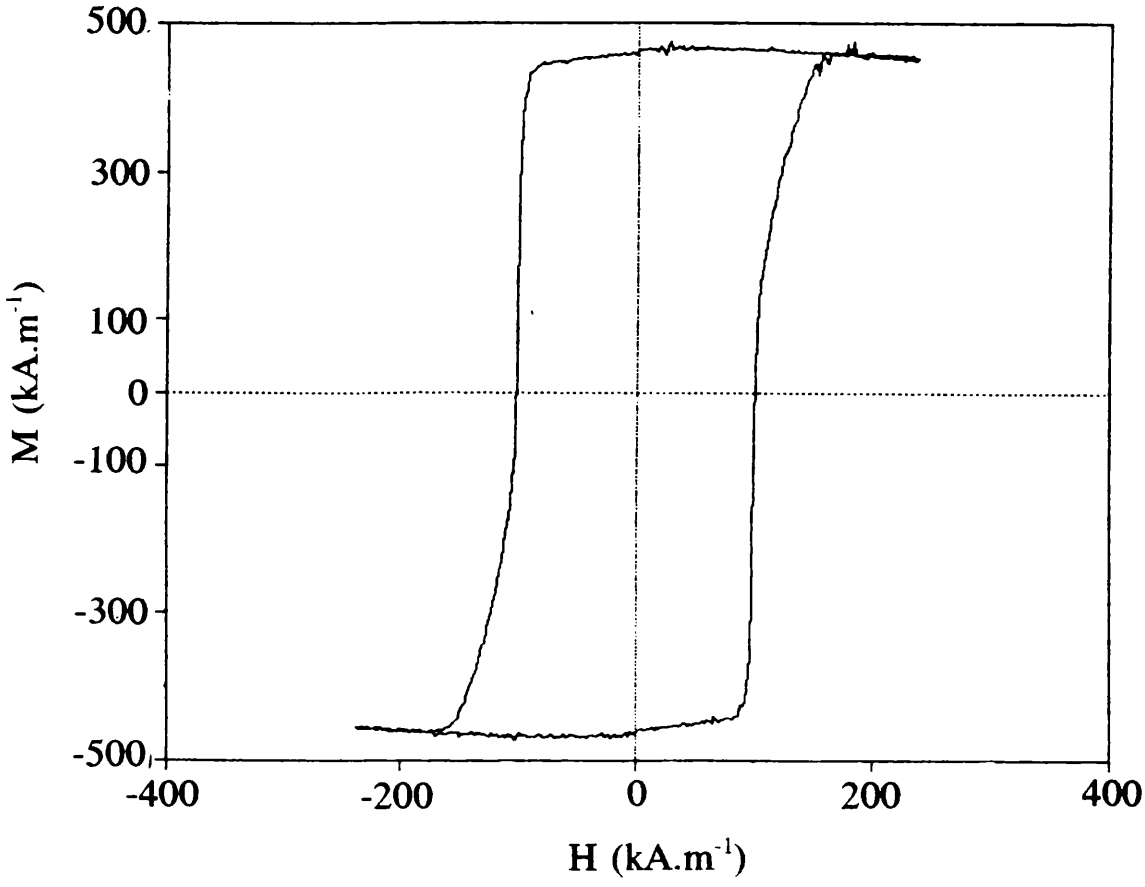

Figure 3.4 Hysteresis loop measured on an AGFM for a 9*(0.35nm Co + 1.7nm Pt) multilayer.

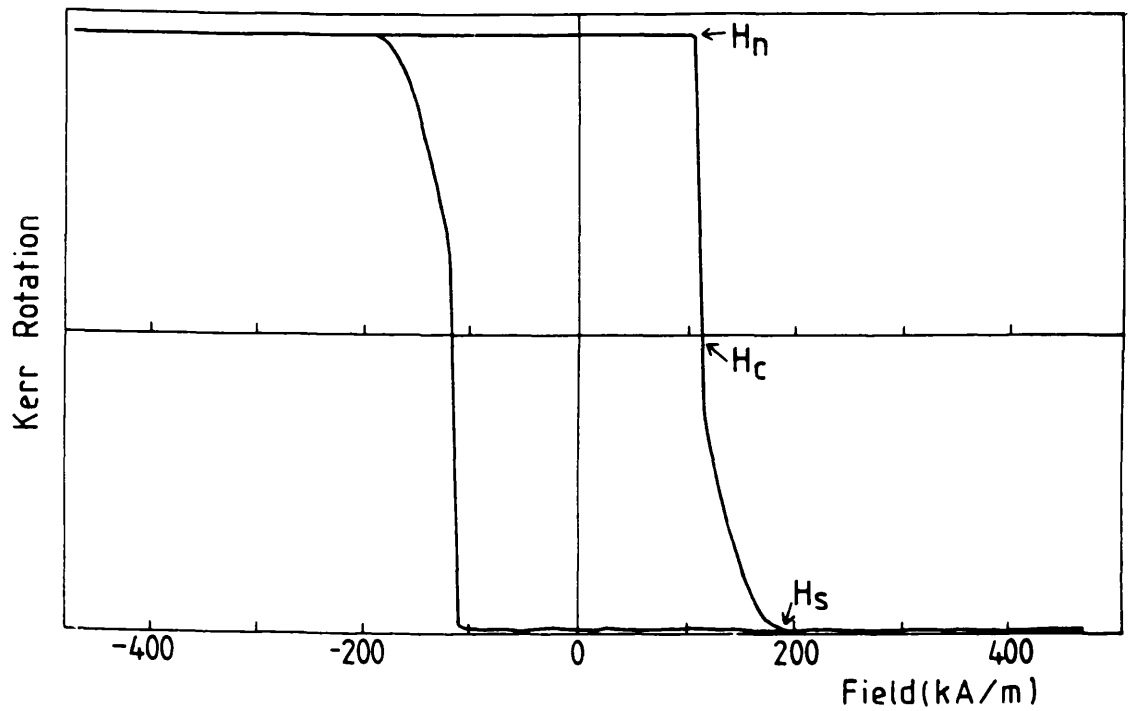

Figure 3.5 Typical MO Kerr loop for a Co/Pt multilayer.

constants.

The individual layer thicknesses (T_{Co} and T_{Pt}) and overall multilayer thickness T_{ML} (where $T_{ML}=N*(T_{Co}+T_{Pt})$), play a significant role in determining the shape of the hysteresis loop and the magnitude of the magnetic and MO parameters. Zeper et al (1989) showed that for increasing Co layer thicknesses (0.24-2.0nm), the hysteresis loops firstly became more sheared (implying that the film is harder to magnetise perpendicularly) and then lost their 100% remanence. A similar trend has also been found in multilayers that have the same bilayer composition (0.4nm Co +1.0nm Pt) but different overall thickness in the range 10-105nm. Figure 3.6 presents the series of loops and it is clear that the hysteresis loops become more rectangular for thinner multilayer films. This phenomena may be explained by the increase in magnetostatic energy contribution as the film thickness increases. The coercivity and the Kerr rotation also depend on the overall film thickness. For the same set of multilayers, H_c, r and θ_k are plotted as a function of N in figure 3.7. The coercivity rose sharply from the very thin layers and seemed to level off at d=70nm. This tendency is similar to that found by Zeper (1989) and Weller et al (1992). The latter suggested that defects on a nm scale are responsible for pinning sites and the large coercivity as the number of bilayers increases. The Kerr rotation generally increases for thicker films. Hashimoto et al (1990) related this increase to the optical properties (optical interference and multiple reflections) and found it independent of the multilayer structure.

The work of several other authors (Zeper 1991, Ochiai et al 1989, Lin et al 1991) has shown that a Co/Pt multilayer suitable for MO recording should have an overall thickness $T_{ML}<30$nm, with the bilayer composition made up of $T_{Co}<0.4$nm and T_{Pt} between 1.0 and 1.5nm in order to attain perpendicular magnetic anisotropy together with 100% remanence. A vapour deposited multilayer with such a composition has a coercivity in the range 100-140kA.m^{-1} and a Kerr rotation of $\approx$-0.13° (at 800nm). With these properties the multilayer may be employed as a MO media.

To gain more insight into the microscopic nature of the physical and magnetic

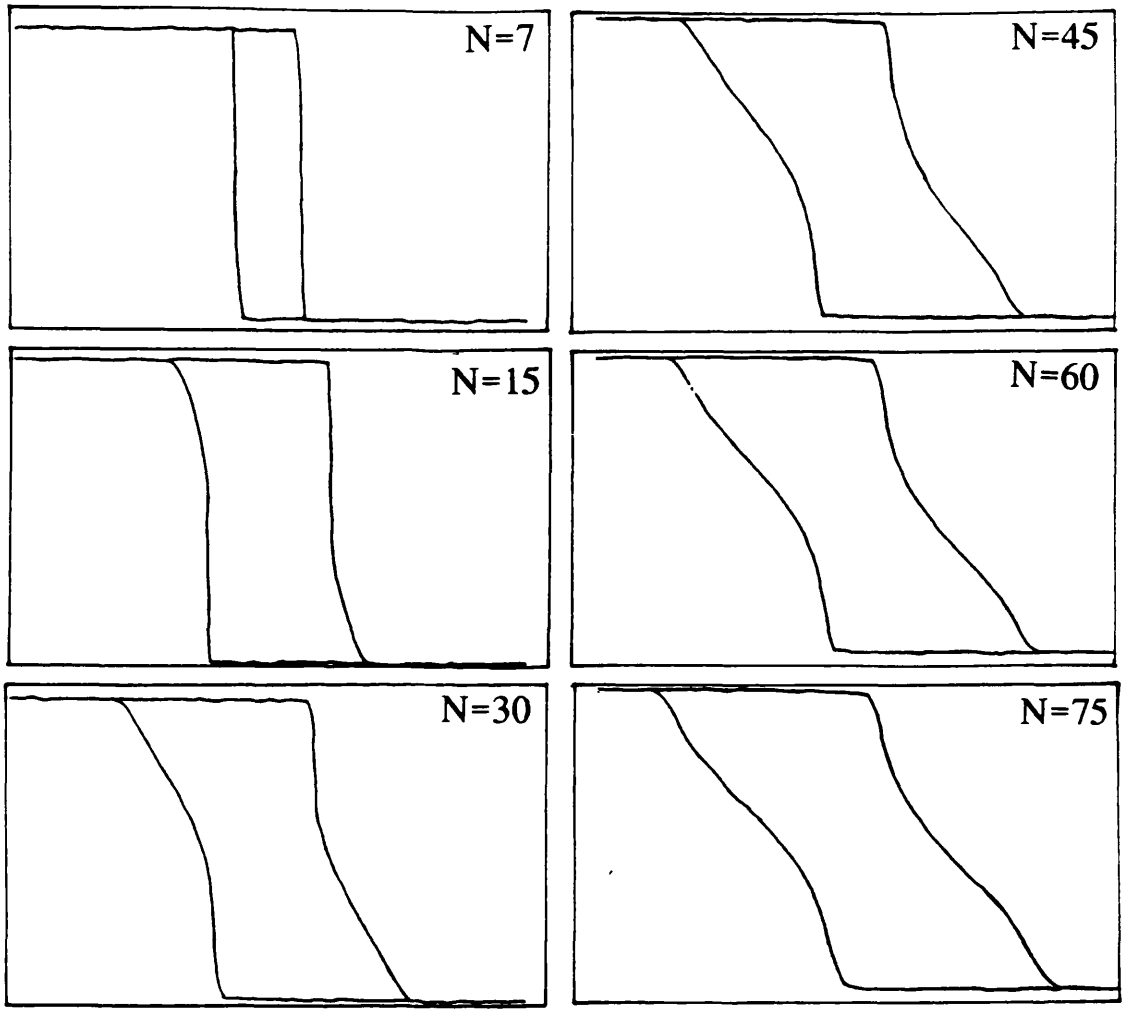

Figure 3.6 A series of MO Kerr loops for Co/Pt multilayers with composition N*(0.4nm Co + 1.0nm Pt).

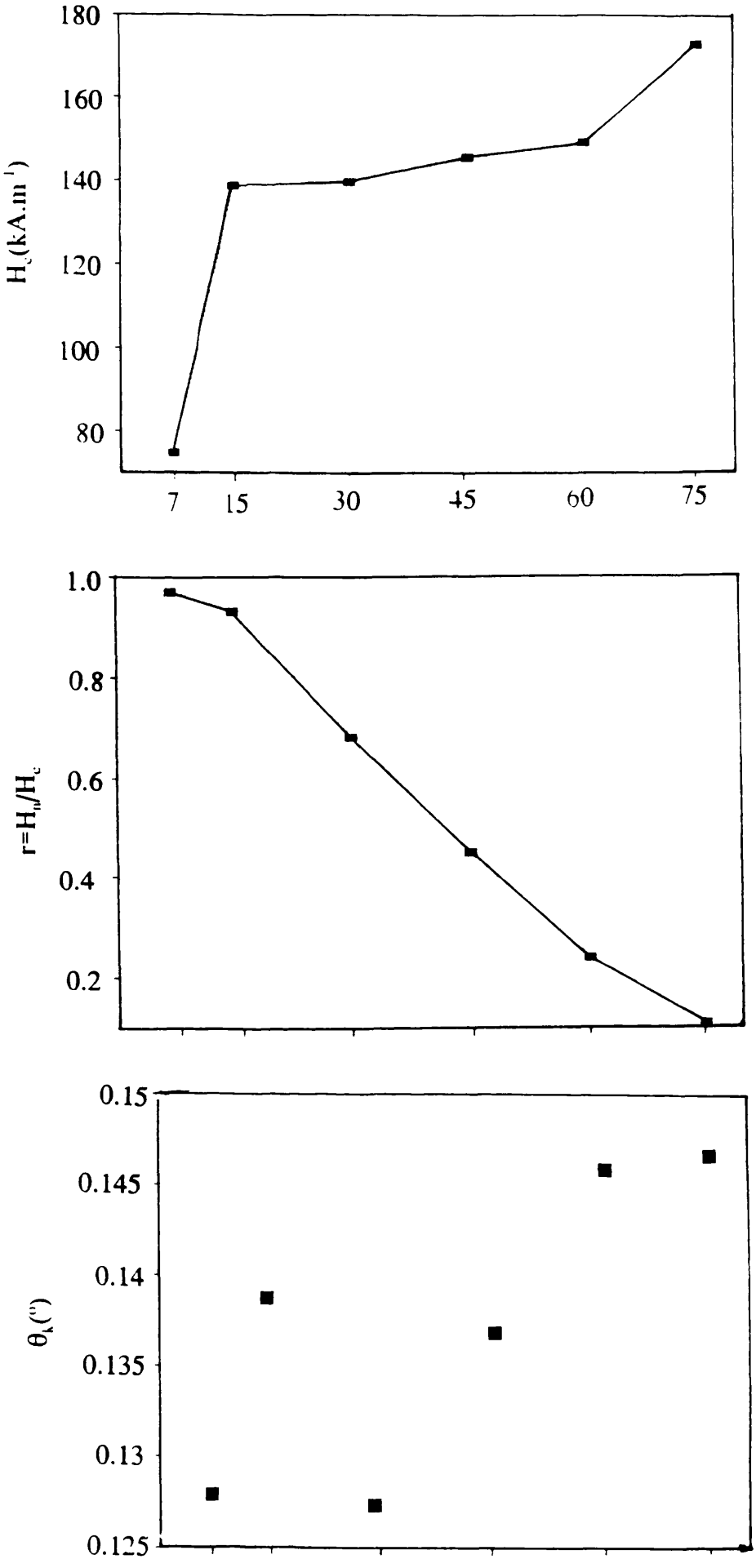

Figure 3.7 Coercivity, rectangularity and Kerr rotation as a function of N for the multilayers whose Kerr loops were presented in fig 3.6.

properties of these multilayers it is necessary to carry out more detailed characterisation. In this project, this has been done using electron microscopy techniques. The following sections describe the methods used and the results achieved.

3.2 Microstructural studies in the electron microscope

A major drawback of Co/Pt multilayers for MO recording is that they are polycrystalline in nature instead of the preferred amorphous type material such as RE-TM alloys. This means that the film is composed of very small grains. It is these grains which cause the inherent noise found in the recording process. The bulk magnetic properties, which were discussed in the previous section may vary by a change in the crystal structure of the film. Li and Carcia (1992) showed, using high resolution electron microscopy (HREM), that microstructural differences, related to the deposition process caused differences in the magnetic properties. The grain boundaries are also important to the microscopic magnetic nature of the multilayers. Grain boundaries and defects in the crystal structure are often the cause of pinning sites for domain walls and nucleation centres. In this section, a number of multilayers have been investigated using standard electron microscopy techniques such as; bright-field (BF) microscopy and selected area diffraction (SAD). At all times, planar sections were studied, which had been deposited on Si_3N_4 windows at Philips. The electron microscopes used were a JEOL 1200EX and a JEOL 2000FX, operated at 120 and 200kV respectively.

Zeper (1991) has shown that the grains in Co/Pt multilayers grow as columns through the entire film. The microstructural contrast observed in the CTEM is a projection of the grains through the entire film thickness and are presented in figure 3.8. This figure (of a multilayer with composition 9*(0.35nm Co + 1.72nm Pt)) was typical of all those grown for TEM observation on Si_3N_4. Although there was a degree of variability in their individual shape (most of the grains are polygons with number of sides between 5 and 8), the grains were

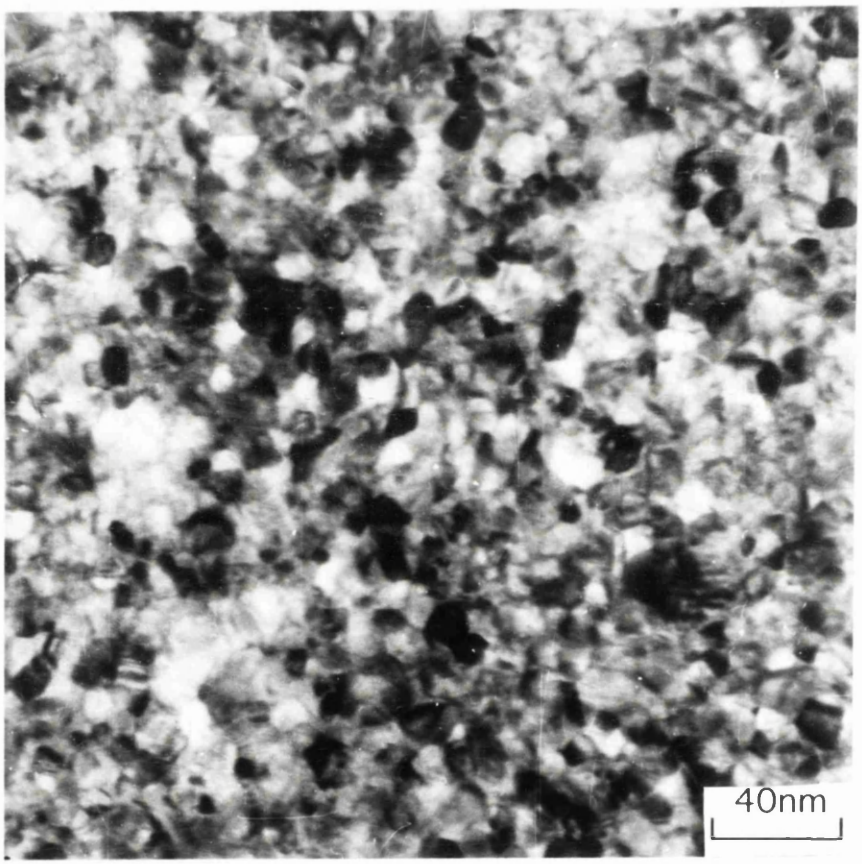

Figure 3.8 Typical CTEM bright field image of a Co/Pt multilayer, revealing the nature of its polycrystalline structure.

well defined. The size was also not constant, but by averaging over a large area (≈0.25μm) a mean value was easily calculated. For the multilayer shown in the above figure, the measured mean grain size was ≈10nm.

The mean grain size was measured for a number of multilayers, some of which had been deposited upon thin (1.0-1.5nm) platinum seed layers. From the measurements, there appears to be no discernible difference in grain size between those deposited on platinum or not. This was not unexpected because a much thicker (>20nm) platinum layer was required for such textured growth. Films produced with thick underlayers usually have larger grains (Lin et al 1991). The overall thickness of the multilayer film also did not effect, to any great degree, the size of the grains.

The planar section diffraction pattern of an evaporated Co/Pt multilayer, presented in figure 3.9 shows the typical ring spacing associated with fcc polycrystalline structures. From this diffraction pattern, taken when the film was untilted, a lattice constant of 4.00±0.02Å was calculated. Very similar values were found for other films. When the multilayers studied in this project were tilted no signs of textured growth were observed. This was most probably because the platinum seed layer was not thick enough to promote textured growth.

3.3 Magnetic studies in the electron microscope

3.3.1 CTEM modes

The three modes of Lorentz microscopy which were described in chapter 2, were all employed during the investigation of the detailed magnetic structure of the Co/Pt multilayers. The two most familiar modes (Foucault and Fresnel) were generally applied initially on the JEOL 2000FX CTEM because of their operational simplicity. This microscope also allows for swift specimen changes, thus many specimens could be studied in a short space of time. The above two modes provide an efficient method for observing the domain structure over a large area in a short space of time, before more detailed work was carried out

Figure 3.9 Typical diffraction pattern found from Co/Pt multilayer.

in the STEM using DPC imaging.

The best Lorentz imaging conditions (for this microscope) were achieved with a small (≤70μm) condenser aperture in conjunction with a smaller spot size (2 or 3) than would be used for standard bright field imaging. To produce Fresnel contrast from a magnetic film, the main imaging lens must be defocussed. This was done by simply altering the current through the lens so that the object plane was no longer coincident with the specimen. Finally the illumination was spread by the condenser to provide near-plane wave electron illumination. The above conditions result in low current densities on the imaging screen and therefore the images were recorded on X-ray film (CEA Reflex-15). This was much faster than ordinary Kodak 4489 film and resulted in exposure times being reduced to ≈5 seconds from ≥60 seconds.

In Fresnel imaging, the observed domain pattern depends on the degree of defocus of the main imaging lens (in this case the objective). In figure 3.10 a series of images shows the effect of this on the observed contrast for a multilayer of composition 20*(0.3nm Co + 0.6nm Pt). For bright field imaging in the JEOL 2000FX, the standard setting of the objective lens was obtained when a current of 3.05A passes through it. A series of Fresnel images were taken with objective current values in the range of 2.8A to 3.3A. The most satisfactory Fresnel contrast was found when the objective lens current was 2.9A.

To implement the Foucault mode, the same condenser aperture and spot size were used. With the objective aperture removed, the diffraction pattern was observed. Although with the available camera lengths it was impossible to view with the eye, the central spot of the diffraction pattern of a magnetic specimen was split into several smaller spots because of the Lorentz deflections. The objective aperture was brought into place and then focused. The diffraction pattern was then brought into focus on this plane using the condenser lens. Finally the aperture was placed in a position such that it intersects the central spot in the direction in which induction was to be mapped. Once in the imaging mode, Foucault contrast was observed. The direction of mapping could be

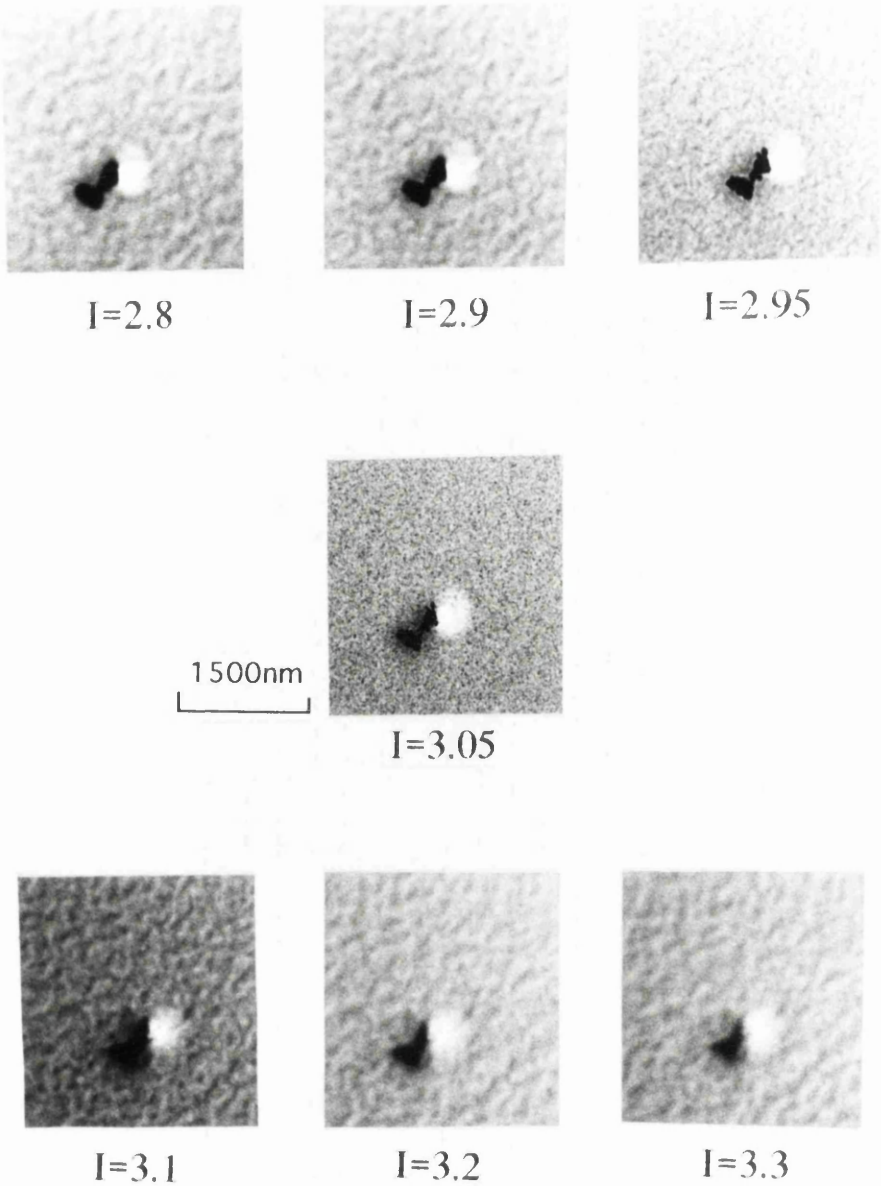

Figure 3.10 A series of Fresnel images of a 20*(0.3nm Co + 0.6nm Pt) multilayer using different defocus values.

changed by manually repositioning the aperture. To obtain constant illumination across the area imaged, the current through the condenser lens was adjusted slightly. In general, two Foucault images were taken for each area; they mapped induction in two orthogonal directions, to provide a better overall picture of the magnetisation distribution within the film.

Co/Pt multilayers, produced for use in MO recording, have their easy direction of magnetisation perpendicular to the plane of the film. Thus, if the film remains in an untilted position, the electrons will pass straight through without being deflected. In this situation it would be expected that some Lorentz contrast would be noticed at the domain walls. If Bloch walls are assumed then there should be a component of magnetisation perpendicular to the beam. However, at no point during all of the Lorentz microscopy was any wall contrast observed. Therefore before implementing Lorentz imaging modes the films were tilted. A range of angles was tested and figure 3.11 shows the effect of tilt angle (0-40°) on the domain contrast for Fresnel imaging. The optimum tilt was found to ≈20°. At this tilt good domain contrast could be observed (in either mode) and with only slight foreshortening there was little loss of geometrical information. From all of the above, the best conditions for the Fresnel and Foucault imaging of Co/Pt in the JEOL 2000FX CTEM were determined and are summarised in table 3.1.

The specimens, following deposition usually arrive in a magnetically "as-grown" state. Although most of the imaging throughout this chapter concerns demagnetised films (see later), it is also interesting to view the domains when the film is in this virgin state. To observe such a distribution (or any other) in the electron microscope, the films were placed in a standard rod which can be tilted about its axis by ≈40° in either direction and either of the two CTEM Lorentz modes were then employed.

Figure 3.12 shows two Foucault images and one Fresnel image of an area acquired under the optimum conditions. The domain structure was complex for these multilayers. It was not well defined in either shape or direction. Across the whole of the film, the domains have irregular boundaries which change

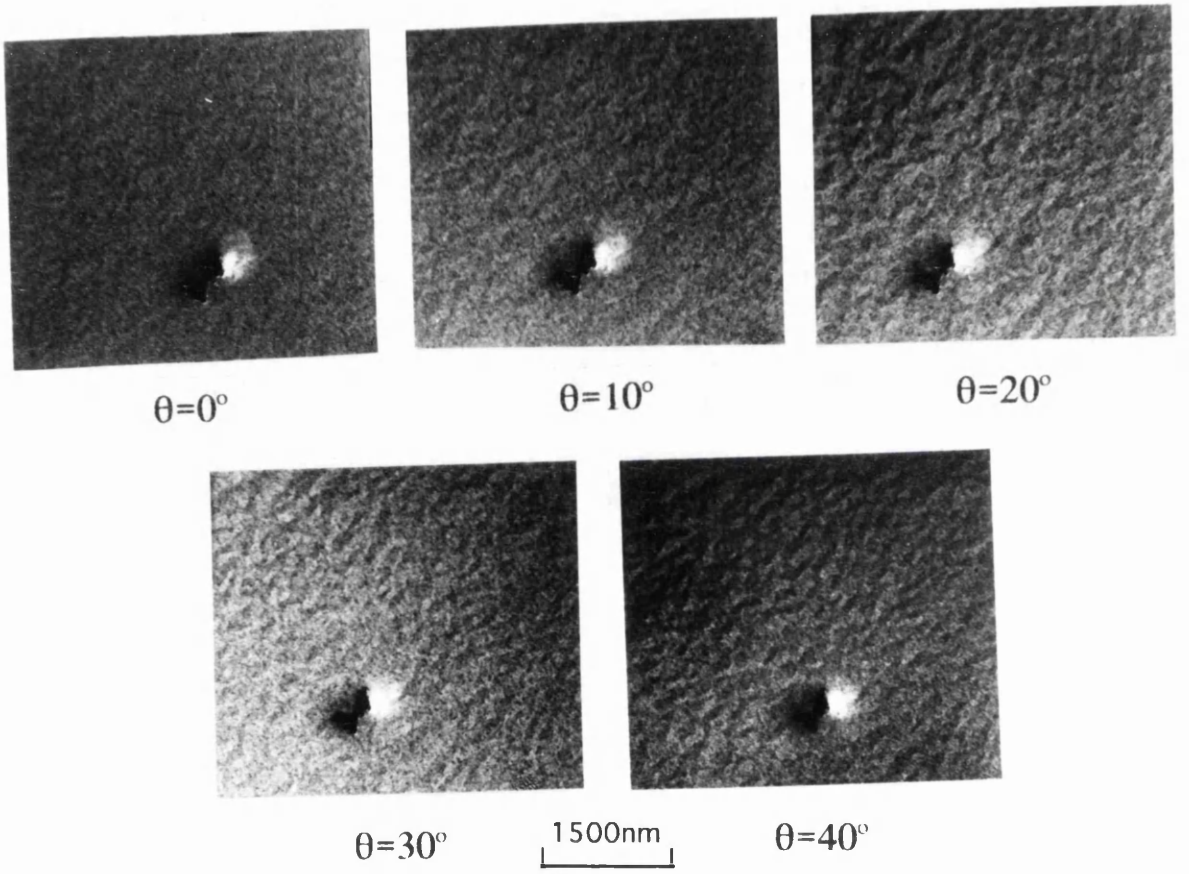

Figure 3.11 A series of Foucault images of a 20*(0.3nm Co + 0.6nm Pt) multilayer using different tilting angles.

	Spot size	Tilt	Aperture	I (OBJ)
Foucault	2/3	≈20°	70μm	3.05
Fresnel	2/3	≈20°	70μm	2.90

Table 3.1 Optimum Lorentz imaging conditions achieved on the JEOL 2000FX CTEM.

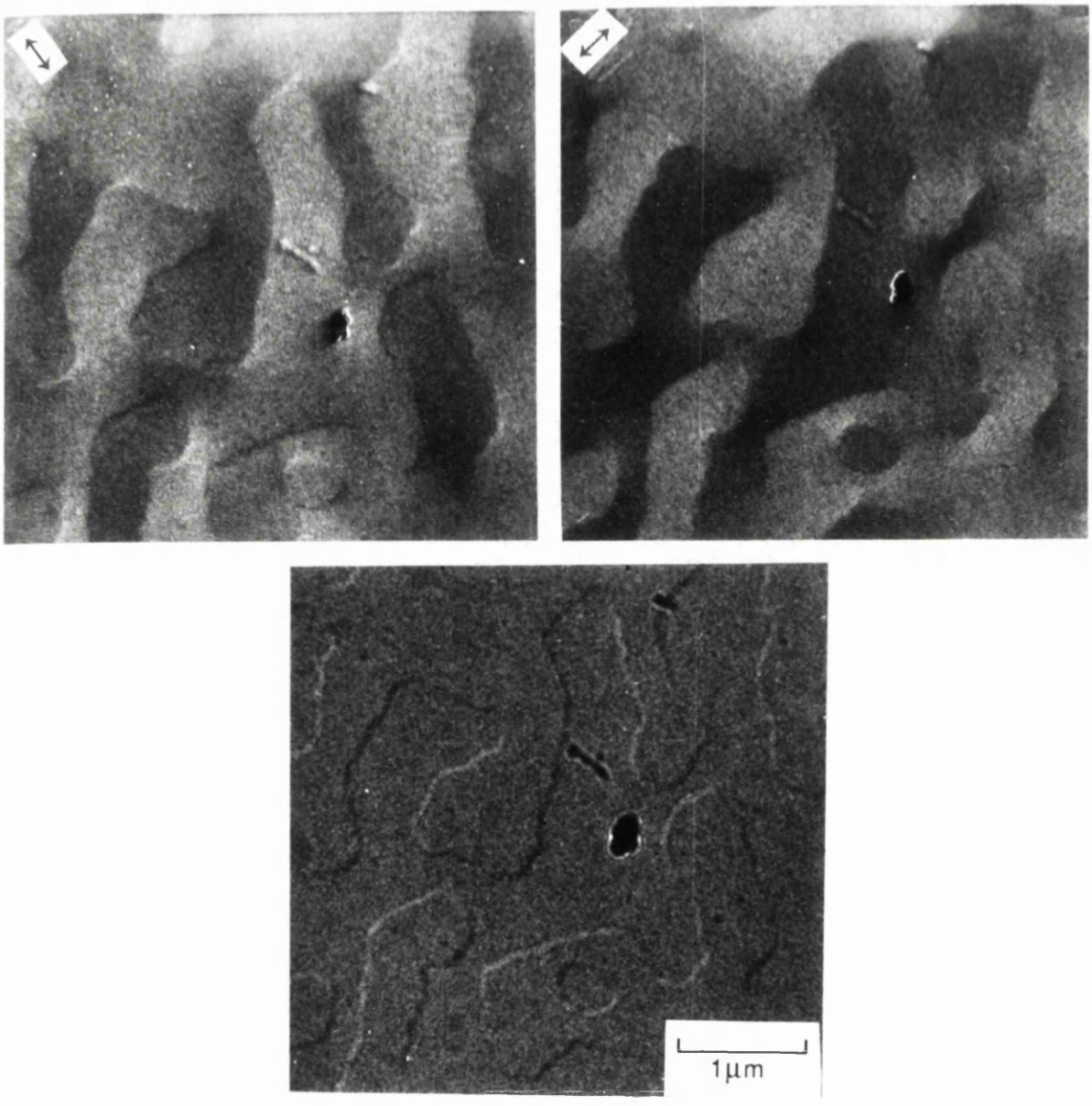

Figure 3.12 Two Foucault images and one Fresnel image of a 14*(0.4nm Co + 0.9nm Pt) multilayer taken under optimum conditions.

direction in many places. The characteristic size of the pattern also varied among multilayers of different composition. Throughout the thesis this type of structure will be called maze-like.

To check for the possibility of lower energy domain configurations the specimens were ac-demagnetised to bring them into an equilibrium energy state. The most usual procedure for ac-demagnetising a magnetic specimen was to apply an alternating magnetic field and then decrease its amplitude toward zero. This resulted in an isotropic distribution of domains which could then be imaged.

This procedure was implemented at Glasgow by placing the specimen between the poles of an electromagnet, whose maximum field (measured by a Hall probe) was >1T. To ensure that the specimen experiences an alternating field, it was spun, by a small motor at ≈1000rpm. By reducing the field slowly, it was possible to reproducibly create an equilibrium domain structure.

When the multilayer was imaged, following ac-demagnetisation, the form of the domain structure was qualitatively the same as in the as-grown state. The mean domain widths were compared, for a series of films, in both the as-grown and ac-demagnetised states. This data is presented in figure 3.13. There was no clear trend to the size of the domains, following demagnetisation. The mean domain period for the thinnest film in its as-grown state was much lower than when it was ac-demagnetised. An explanation for this may be that many island like nucleation points may be formed due to the extreme thinness of the film during initial deposition, thus allowing a smaller domain period. The other films apart from the thickest display near-parity in domain sizes between the as-grown and ac-demagnetised states. One possibility for the thickest film may be due to heating during deposition.

To check that the energy state achieved via the above method was truly a minimum, the multilayers were demagnetised using a hard axis technique. The specimen was saturated with its hard magnetic axis (in-plane) aligned along the field lines of the electromagnet. The field was then removed and the magnetisation was allowed to relax back into its easy (perpendicular) axis.

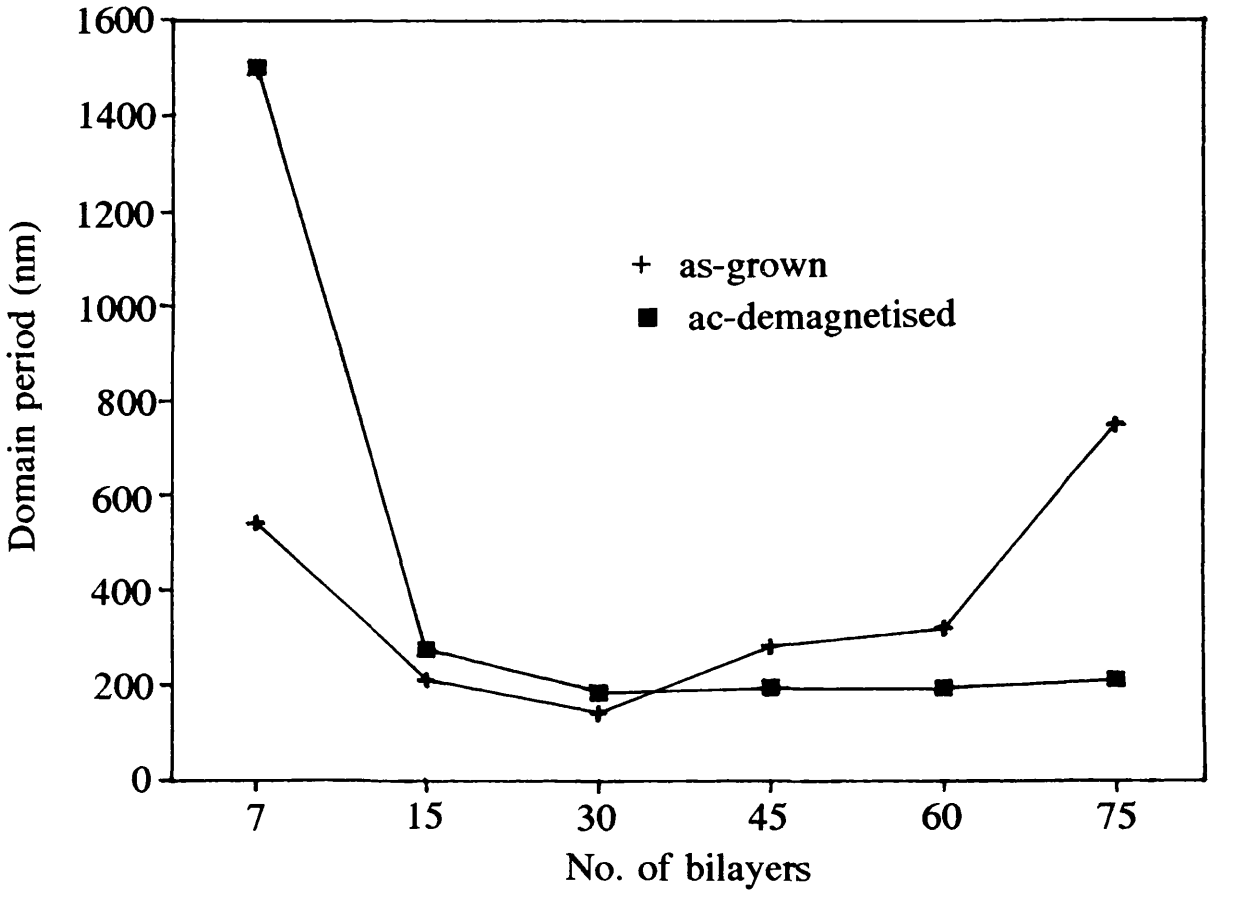

Figure 3.13 Domain periods in both the as-grown and ac-demagnetised states for a series of films whose composition varies as a function of N.

Figure 3.14 presents two Foucault images (mapping induction perpendicular to the tilt axis) of the same multilayer, which had been demagnetised using the two above methods. From the figure it was clear that the resultant domain structures were very similar and difficult to distinguish visually. This suggests that an energy minimum had indeed been achieved.

This section has shown that the CTEM modes of Lorentz microscopy are extremely useful for the quick and efficient observation of magnetic domain structures. However for more detailed investigations and any quantitative analysis, it was necessary to employ the DPC (MDPC) mode in STEM. The next section details how this was carried out on Co/Pt multilayers and reports on some initial results.

3.3.2 STEM modes

As explained in chapter 2, all MDPC imaging was implemented on the VG HB5 STEM. The specimen was placed in a microscope cartridge that allowed tilting of ±60° in both the x and y directions. To make overall comparisons easier, the specimen was usually tilted about the same axis and through the same angle each time. For Co/Pt multilayers, a tilt of ≈20° about the x-axis was used.

In order to optimise the magnetic contrast observed, the correct configuration of lenses and apertures in the STEM was of paramount importance. The difficulties when imaging Co/Pt multilayers arose because of the very small Lorentz deflection angle (<2μrad) produced. This was due to the actual amount of magnetic material (cobalt) being very small (≈5nm) and the fact that it was always surrounded by non-magnetic platinum. The following outlines the most commonly used microscope set-up for imaging Co/Pt multilayers. A 500μm virtual objective aperture (VOA) was used as a spray aperture and the probe was formed with the C1 lens in conjunction with a 50μm selected area aperture (SAA). This resulted in a probe semi-angle α, subtended at the specimen of 0.25mrad. The resolution limit is given by $\lambda/2\alpha$ where λ is the electron wavelength. The electron energy in the HB5 STEM is 100keV (λ=3.7pm) and a value of 7.5nm was obtained for the resolution limit. Due to the very small

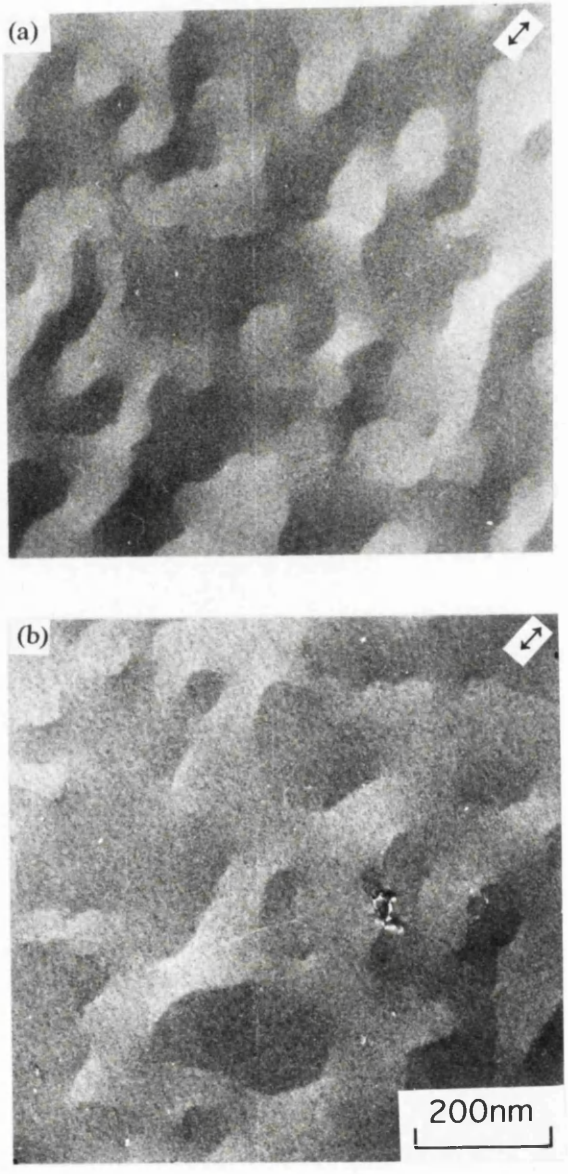

Figure 3.14 Two Foucault images (mapping induction perpendicular to the tilt axis) of the same multilayer (15*(0.4nm Co + 1.0nm Pt)) which has been demagnetised by (a) the ac and (b) hard axis methods.

Lorentz deflection from the cobalt layers, all three post specimen lenses (PSL) must be engaged to provide a large enough camera length. The typical settings were; P1:+6, P2:+6, P3:+8. With such a camera length, $\kappa \approx 0.8$ ensuring that there is no loss of signal on a scale of ≈20nm whilst that on a smaller scale was substantially reduced. Some multilayers imaged in this study had thicker platinum layers (≈1.5nm) and in order to maintain the same contrast levels as before, the microscope configuration must be altered. Firstly, a smaller (25μm) SAA was used to form the probe. The camera length is also increased by changing the excitation of the PSL's to; P1:+9, P2:+6, P3:+9. Once good magnetic contrast was observed on the viewing screen of the microscope, MDPC imaging could take place.

It was possible, using the Link eXL acquisition system, to collect a variety of difference (and sum) signals simultaneously. For the MDPC imaging of Co/Pt multilayers, three images were acquired together. Two provided maps of magnetic induction parallel and perpendicular to the tilt axis and the third was a bright field image revealing crystallite contrast. Different information was gained from each of the maps of magnetic induction. The image which contains the most useful information was always the one which mapped induction perpendicular to the tilt axis. In the other image, cancelling effects due to stray field contributions from components of induction promoted by tilting about a particular axis conceal important magnetic information.

A typical threesome is shown in figure 3.15, together with the detector arrangement. The composition of the film imaged was 15*(0.35nm Co + 1.08nm Pt). All the images are in perfect registration (as observed by the small defect on the left hand edge of each image) and were acquired over four frames in ≈150s. The resolution of these images was ≈20nm. As explained, the B-D (upper left) image was of most use for analysing the domain structure. The black and white areas within the image correspond to domains of opposite polarity (up or down). Once again, the maze-like pattern was observed. Although not a conventional stripe domain pattern, it was still possible to determine a mean domain spacing for each multilayer imaged. This

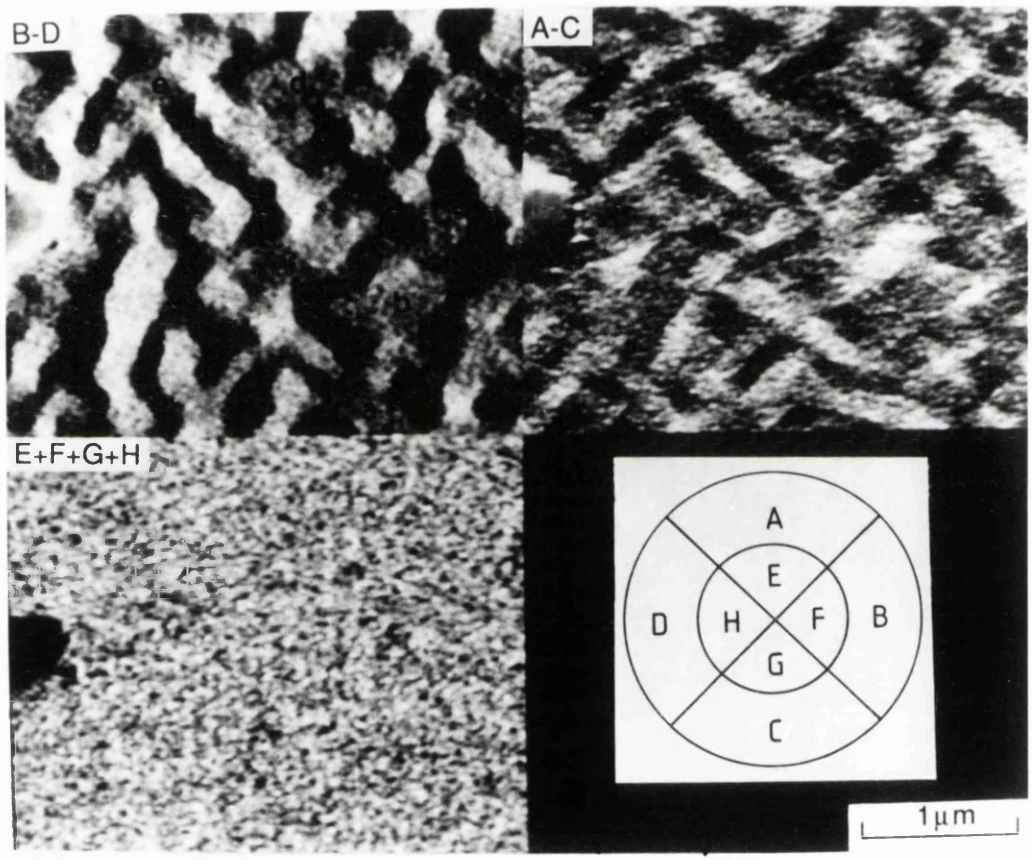

Figure 3.15 Typical MDPC threesome showing magnetic contrast in two orthogonal directions (B-D, A-C) and crystallographic contrast (E+F+G+H). The detector arrangement is also shown.

measurement will be employed in determining domain wall energies for a series of multilayers in chapter 6.

Upon closer examination, an interesting feature was seen in the B-D image (figure 3.16). Many small areas (marked a-d) of the image appear without strong contrast. These "grey" areas correspond to the electrons experiencing a near null Lorentz deflection as they travel through the multilayer. The first explanation for this phenomenon was that the domains in each individual cobalt layer were not in exactly the same lateral positions.

However, a more realistic explanation for the "grey" areas becomes apparent when the tilt axis was changed. This is demonstrated in figure 3.17. Between the arrowed spots on the upper image, which has been tilted about the y-axis, a "grey" areas exists. When an orthogonal tilt axis was used (lower image), it was clear, despite the foreshortening that strong contrast now exists between the same two spots. Thus these areas may be attributed to the domain structure lying in a particular direction and the tilt axis chosen.

3.4 Summary

This chapter summarised the deposition and bulk (physical and magnetic) characterisation of the multilayers carried out at the Philips Research Laboratories. In order to more fully understand the bulk properties, electron microscopy techniques were applied. Standard imaging techniques revealed the polycrystalline nature of the film and allowed grain sizes and lattice constants to be calculated. Specialised magnetic imaging techniques were employed to allow the complicated domain structure to be observed with a resolution of ≈20nm. Mean domain widths could be measured from images and will be used in chapter 6 to calculate domain wall energies. The next two chapters investigate, in more detail, the domain structures of the multilayers. Chapter 5 studies the in-situ magnetising of the domain structures seen in this chapter, while in chapter 6 thermomagnetically written domains are investigated.

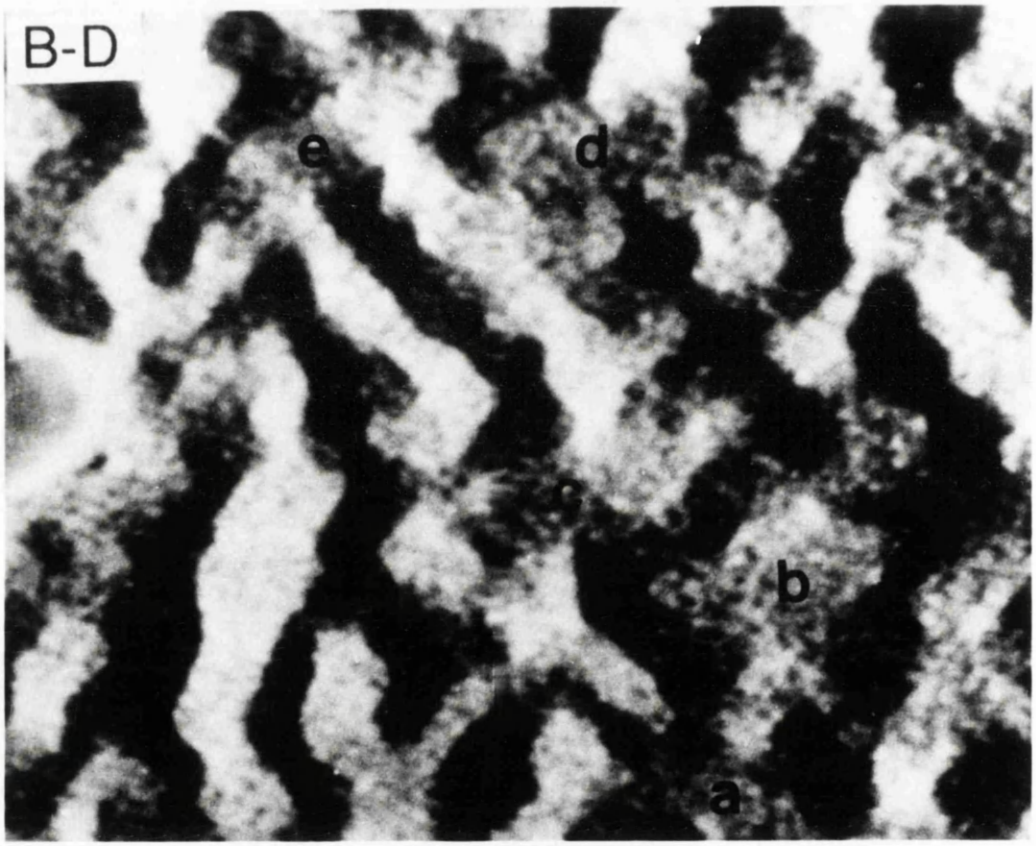

Figure 3.16 B-D image from figure 3.14, enlarged to reveal numerous "grey" areas which represent a near null deflection for the travelling electrons.

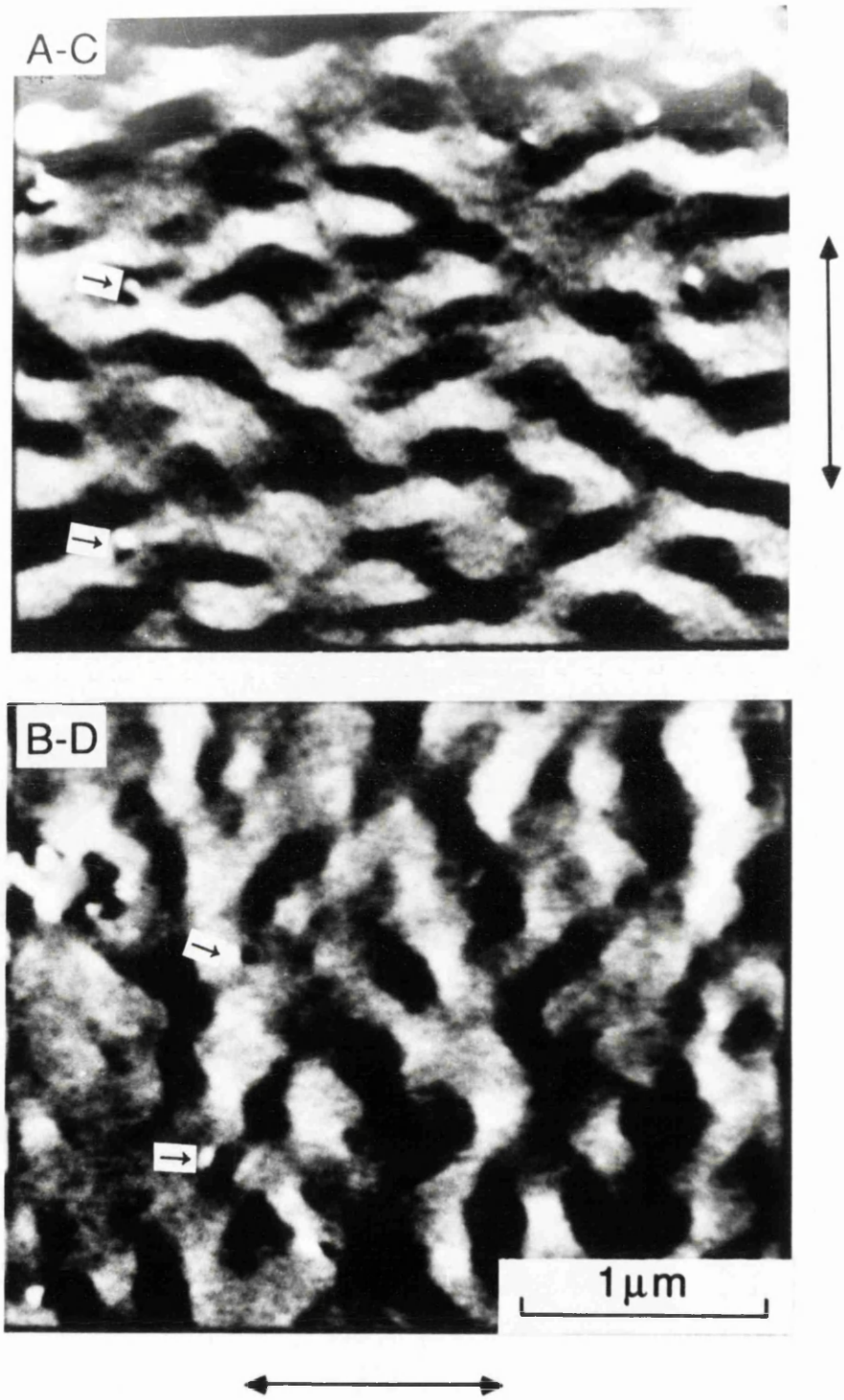

Figure 3.17 Two MDPC images of the same area, tilted about orthogonal axes to reveal the nature of the "grey" areas.

Chapter 4

In-situ magnetising experiments in STEM

4.1 Introduction

Information is stored in MO media in the form of thermomagnetically written domains (bits). The dimensions of these bits can be less than a micron given favourable conditions. The size, shape and magnetisation of the written domains must be regular in order to minimise the read-back noise in the recording set-up. From an understanding of the thermomagnetic writing process by which the marks are formed, it is possible to lessen the effects of the noise contributions. Another important consideration is the stability of the domain after writing has taken place and the effects that external magnetic fields have on it. Before studying thermomagnetically written domains, this chapter investigates the two above phenomenon for naturally occurring domain structures in Co/Pt multilayers.

MDPC Lorentz microscopy was implemented (at room temperature) to investigate the detailed magnetisation processes that occur in these multilayer films produced for use in MO recording. This was achieved by the application of in-situ magnetic fields and observing the domain distribution in a number of remanent states around the M-H loop of the films.

The modelling of the magnetisation process within MO media has been previously carried out by Mansuripur (1987). He modelled the mechanism of magnetisation reversal in amorphous alloy films (TbFe, GdCo, GdTbFeCo) and compared this with the observed (Kerr microscopy) behaviour of the media at nucleation and during the growth of the domains under externally applied magnetic fields. Lin et al (1988) examined experimentally the different micromagnetic processes in amorphous Tb-Fe films that occurred when the films had either a square or non-square hysteresis loop. They applied in-situ magnetic fields and made observations using the Fresnel mode of Lorentz

microscopy. Although this study proved successful, two drawbacks do exist when using this imaging technique. Fresnel imaging has limited spatial resolution, since the objective lens cannot, under normal circumstances, be used as the imaging lens. This is an important consideration for this investigation because we are interested in studying the domain structures of these films at high spatial resolution (magnification in the range x20k-x50k). By implementing MDPC microscopy however, it is possible to examine with higher resolution (≈20nm) the domain structures in each remanent state.

For each multilayer investigated in this study, in-situ magnetic fields were applied and MDPC images were taken at various points around the cycle. The remanent domain structures were observed and following digital image processing, remanence loops were created. Their shape was compared with the actual magnetisation curves measured by the AGFM.

4.2 Experimental

The magnetisation processes within two Co/Pt multilayer films (samples I and II), which had different physical and magnetic character were investigated in similar experiments. Table 4.1 summarises the physical, magnetic and MO properties of the two films. The Kerr hysteresis loops for each film, which were measured at Philips, are shown in figure 4.1. Before any micromagnetic observations were made in the STEM, bulk magnetisation curves were measured for both films and the next section outlines the experiments undertaken.

4.2.1 Bulk magnetising measurements

It has been shown (Liu et al 1991) that the shape of bulk magnetisation curves has a direct bearing on the recorded signal from MO media. For that reason, isothermal remanence (IRM) and dc-demagnetisation (DCD) measurements (O'Grady 1990) as well as standard M-H hysteresis loops, were carried out using the alternating gradient field magnetometer (AGFM) (Zijlstra 1970, Flanders 1988) at the University College of North Wales, Bangor. The

	Sample I	Sample II
T_{Co} (nm)	0.37	0.35
T_{Pt} (nm)	1.72	1.08
N	9	15
initial layer	Co	Pt
K_{eff} ($MJ.m^{-3}Co$)	0.72	1.00
θ_k (°) λ=633nm	0.11	0.14
H_n ($kA.m^{-1}$)	93	119
H_c ($kA.m^{-1}$)	101	139
H_s ($kA.m^{-1}$)	169	247
d (nm)	370	280

Table 4.1 Measured parameters for samples I and II.

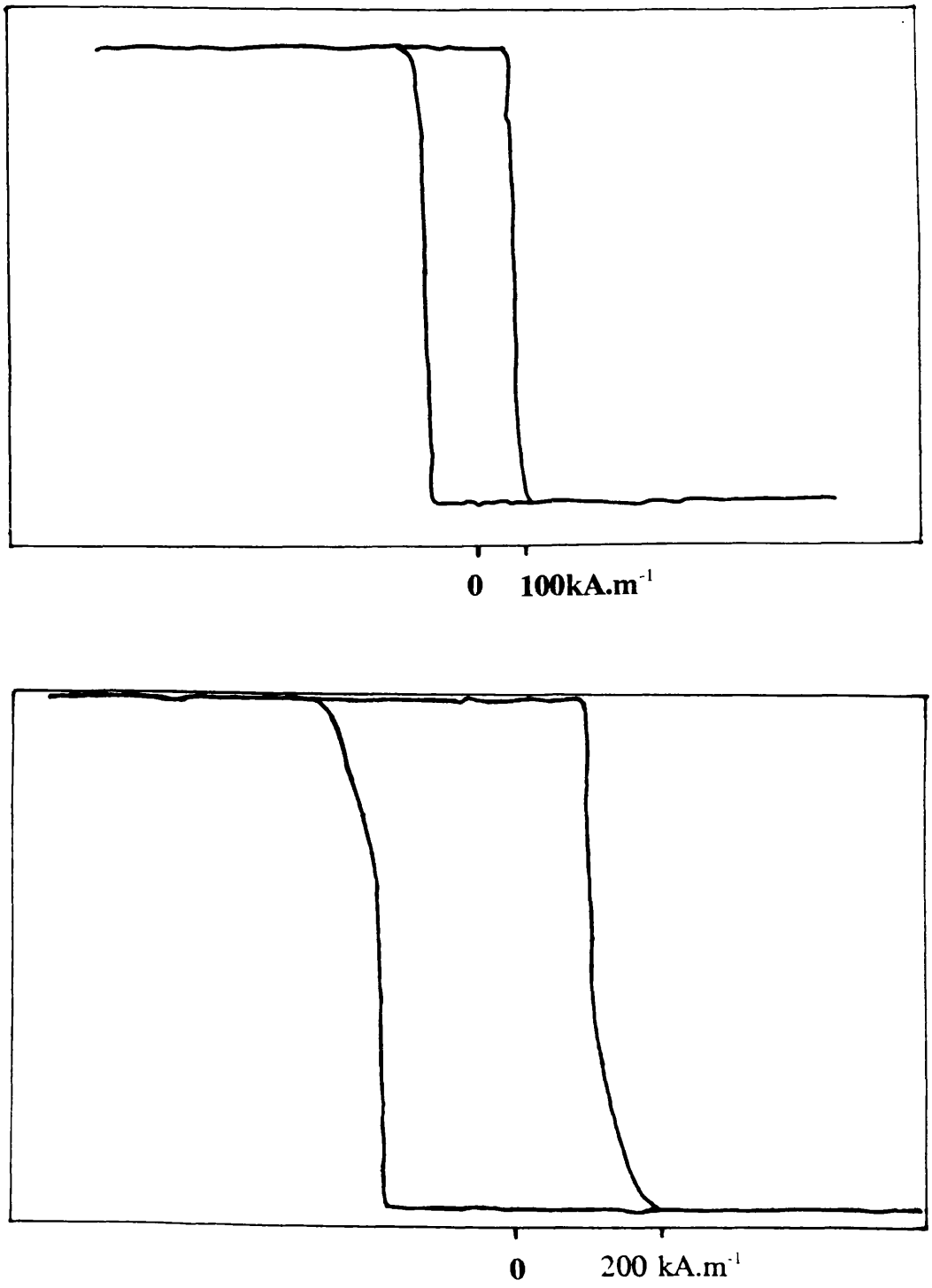

Figure 4.1 MO Kerr hysteresis loops for sample I (top) and sample II measured at λ=633nm.

mechanism for measuring M-H loops using an AGFM has already been described in chapter 3. A complete M-H hysteresis loop can be produced very quickly (≈100s) and with great precision using such a technique.

The starting point for an IRM curve was a state of demagnetisation (usually ac-demagnetised, as explained in chapter 3). From there, a positive field was applied, then removed after which the remanence is measured. For the two films investigated, this process was repeated with ever increasing positive fields until saturation was reached. Saturation was the starting point for measuring a DCD curve. It measures the field needed to go from saturation in one direction (positive) to saturation in the other (negative). Therefore, the remanence was measured after the application of ever increasing negative fields. IRM and DCD curves were measured for both films and they are presented together with the M-H loops in figures 4.2 and 4.3.

The shape of the hysteresis loops measured by the AGFM were very similar to the Kerr loops produced at Philips. Both exhibit extreme squareness (≈100% remanence) and rectangularity r (as defined in chapter 3) close to unity, with a sharp nucleation point and a long tail approaching saturation. During the in-situ magnetising of the films, it was at strategic points around the IRM and DCD curves that the remanent domain pattern was observed by MDPC microscopy to provide direct information on domain nucleation and the development of the domain structure as saturation was approached.

4.2.2 In-situ magnetising measurements

In the STEM, the samples were subjected to vertical field variations which closely resembled those in the IRM and DCD measurements, which were described in the last section. This was realised by pulsing the objective lens for constant short periods (pulse duration ≈1s) at variable excitations. The procedure for the magnetising and subsequent imaging of the multilayers was as follows: the microscope was configured (as described in chapter 3) with the objective lens off to provide the best possible magnetic contrast for the film under investigation and an identifiable area of the sample (eg small hole, dirt speckle

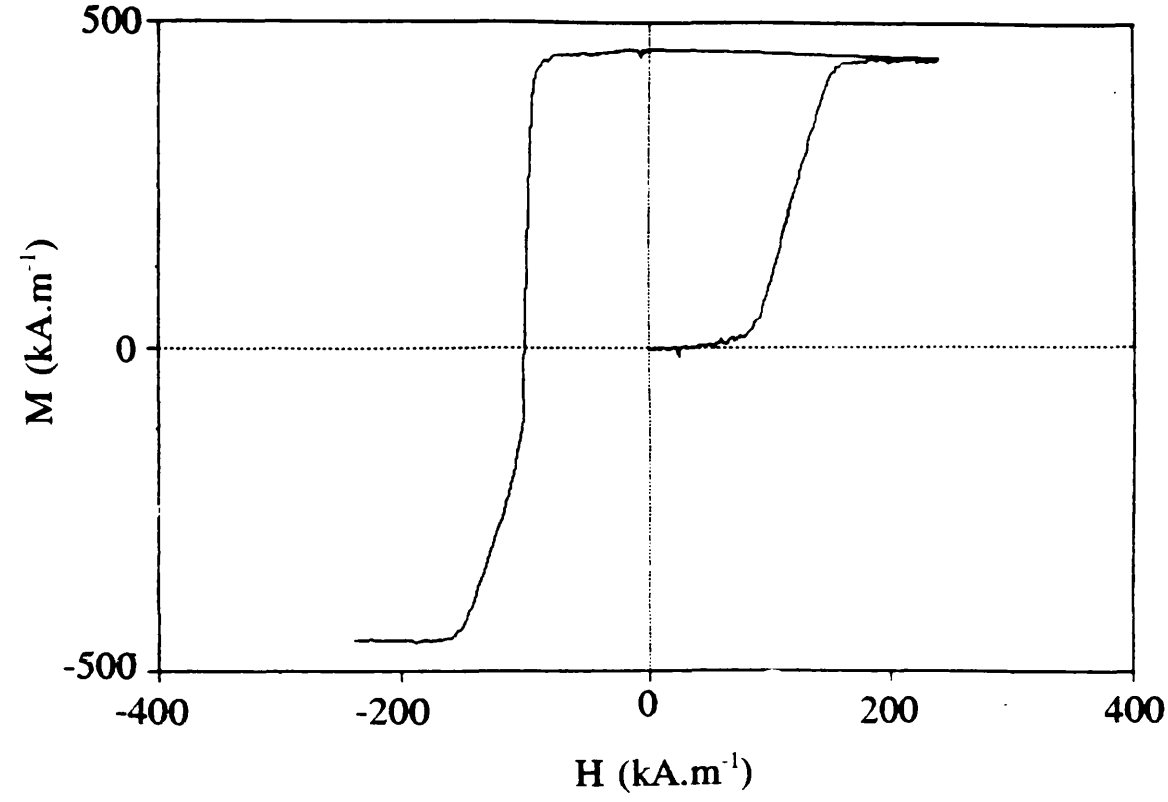

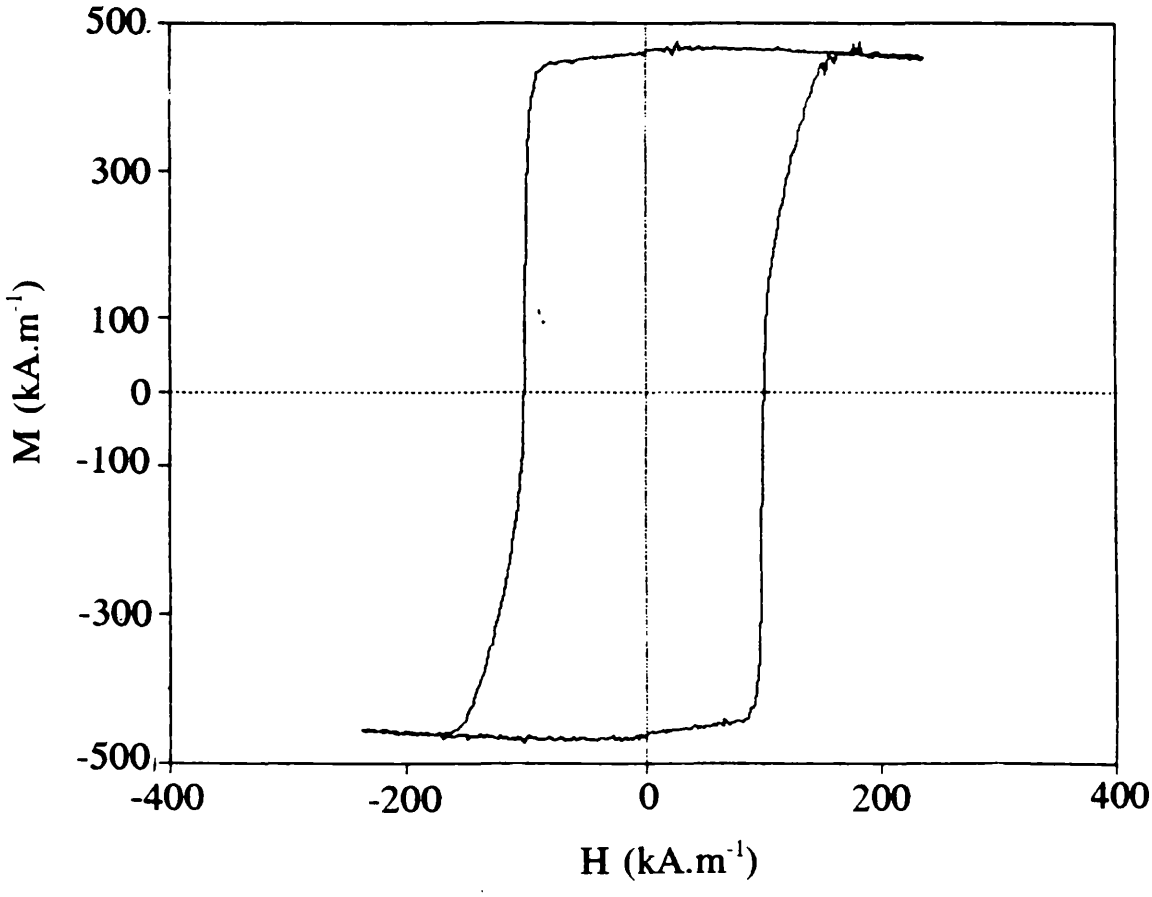

Figure 4.2 IRM, DCD curves (top) and M-H hysteresis loop for sample I.

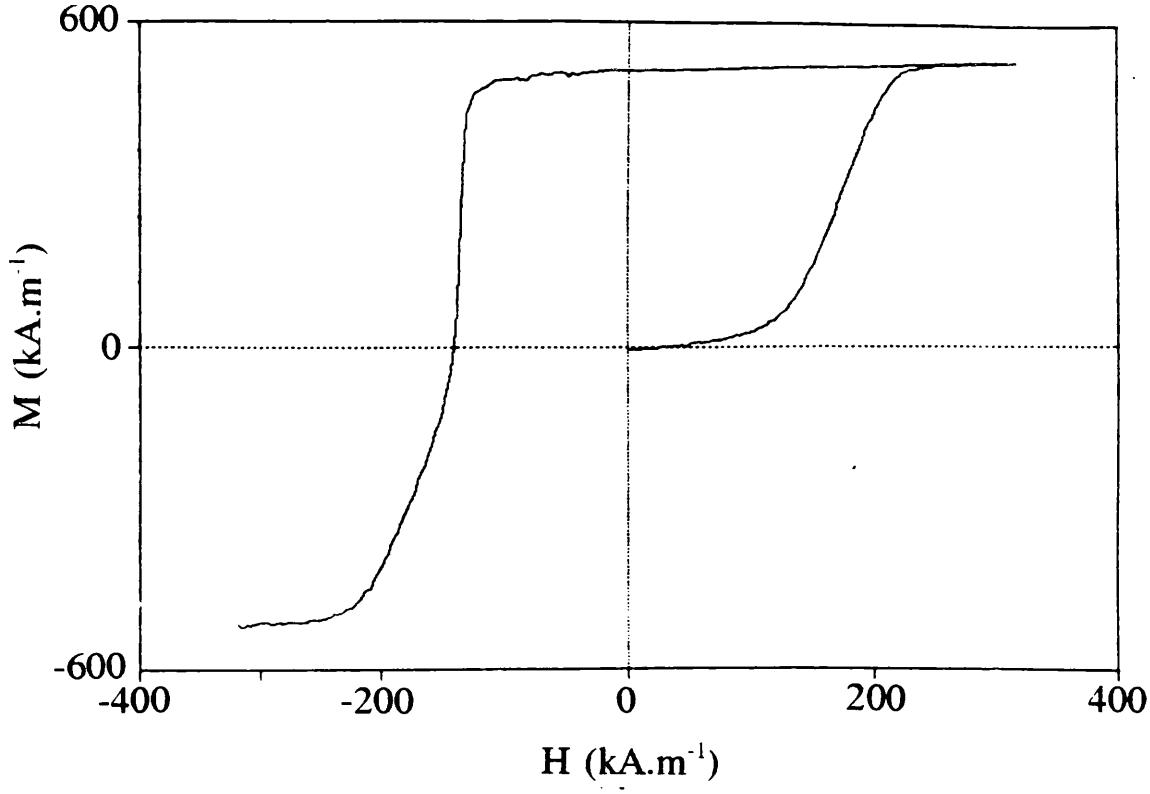

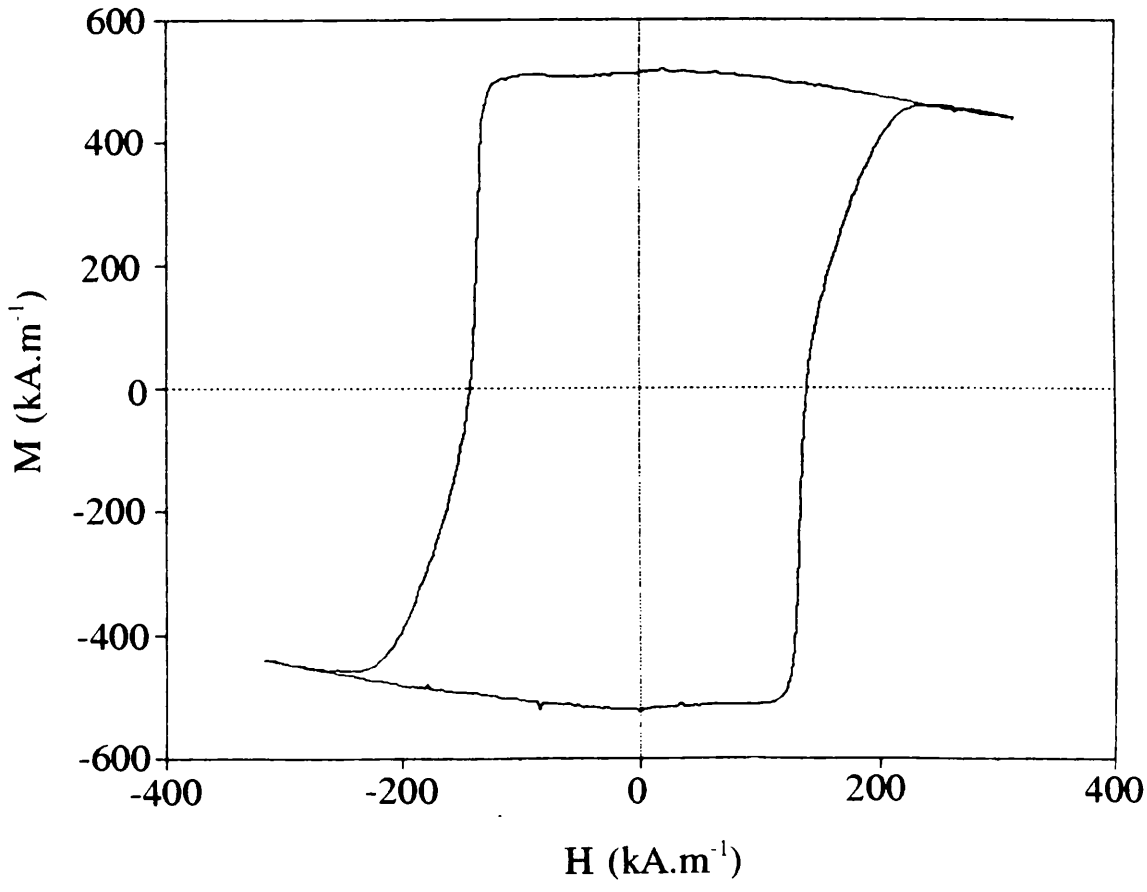

Figure 4.3 IRM, DCD curves (top) and M-H hysteresis loop for sample II.

on surface) was positioned towards one side of the viewing screen on the microscope. This was to ease the task of locating the area that was being repeatedly imaged, allowing observations of the same area to be made after each field application. Starting from an ac-demagnetised state, the sample was slowly magnetised by increasing the current through the objective lens in each pulse. After each field application, the objective lens was switched off. Following slight repositioning and focusing (necessitated by hysteresis in the objective lens and a resulting small residual field) the sample was imaged in the usual manner by MDPC microscopy, averaging over four frames in order to reduce noise. The process was repeated until saturation was reached in the positive direction. The field direction was then reversed and the procedure repeated until saturation in the opposite direction was attained. Finally the sample was again subjected to fields in the original positive direction until saturation was reached once more in that direction. In this way, domain distributions in a number of remanent states around the complete remanence loop were directly observed by MDPC microscopy.

4.3 Results

4.3.1 Observations from MDPC images around remanence loop

4.3.1.1 Sample (I)

Once MDPC images of remanent domain structures had been collected from around the complete remanence loop, it was possible to arrange them into the montage shown in figure 4.4. This facilitates observations of the changes of the domain structures. In the ac-demagnetised state, the characteristic maze-like domain pattern (chapter 3) was observed. The film had a mean domain period d (averaged over 20-30 domains) of 370nm. The domain period was defined as twice the domain width. This magnetic state of the multilayer is shown in the top left corner of figure 4.4. The remainder of the image corresponds to the various remanent state images around the loop with the applied field values for each image given in $kA.m^{-1}$. It should be noted that the small vertical lines

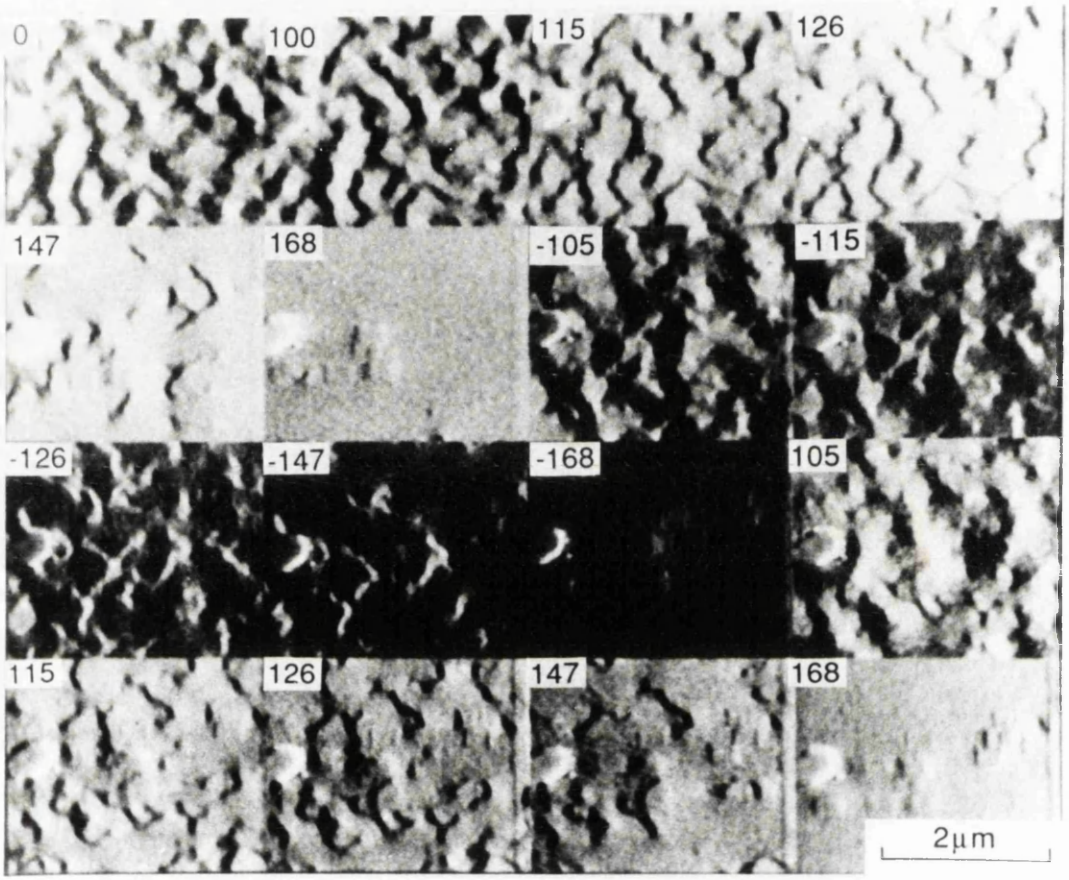

Figure 4.4 Montage of MDPC images taken at various positions around the remanence loop of sample I.

visible in increasing numbers as the series progresses (and most apparent in the images of the saturated states) are due to the fixing of mobile contaminants in the microscope and have nothing to do with the magnetic structure of the film.

Following the application of a field (H_{ext}), there was little or no change in the domain structure until a field of comparable value to the coercivity was applied. For sample (I) with a coercivity of 101kA.m^{-1} the first noticeable change occurred when a field H_{ext}=100kA.m^{-1} was applied. Beyond this point, as larger fields were applied, the domain structure changed steadily as it approached a state of saturation. From the images in figure 4.4, it appears that following the application of successively higher magnetic fields (H_{ext}=100, 115, 126kA.m^{-1}) the domain walls move perpendicular to their length to allow growth of those favoured domains in which the magnetisation direction lies parallel to the applied field. For most domains in this distribution, their overall "skeletal" shape remains substantially unchanged during the early approach to saturation and it was only their relative dimensions which alter. This is indicative of there being a high density of wall pinning sites and walls tend to move without significant distortion, at least on a scale somewhat less than 100nm. Beyond applied fields of 126kA.m^{-1}, the rate of approach to saturation increases and substantial domain annihilation occurred. It was noticeable however, at these higher fields, that not all domains, or even parts of the same domain were annihilated with comparable ease and magnetic fields very close to saturation must be applied in order for this to arise.

Following saturation, domains were renucleated by the application of negative magnetic fields. The application of fields just below the nucleation field (H_{ext}=0.95H_n≈95kA.m^{-1}) left the domain structure of the film unchanged in its saturated state, whilst the application of H_n led to the sudden appearance of domains across the whole area of the film. At the point of nucleation the form of the renucleated domain structure had changed quite considerably from any of the structures observed before. Although still approximately maze-like, the domains appeared more ragged and large areas of the pattern remained unreversed. On application of higher negative fields (H_{ext}=-126kA.m^{-1}) domains

were formed whose style resembled that of domains formed at comparable fields during the initial magnetising process (IRM). The actual dimensions and distribution of these domains (as well as their polarity) did however differ from those formed at H_{ext}=126kA.m^{-1}).

After saturation in the negative direction, domains were once more renucleated when a positive field of H_{ext}=105kA.m^{-1} was applied. The latter part of this second approach to positive saturation showed the same trend as the first.

A more detailed investigation of the nucleation process at a particular location in the film was also carried out. The multilayer was subjected to a simple magnetisation cycle, which involved repeated saturation (in the positive direction) and domain nucleation. The magnetic field applied was H_{ext}= -120kA.m^{-1}, which is greater than H_n. This was done in order to produce a domain structure with more recognisable features. Figure 4.5 shows the results of four successive cycles for the same small area of the film. It was apparent that in many instances, domains nucleate from the same site (six such sites are marked a-f on figure 4.5) on each application of the field of -120kA.m^{-1}. Small differences in the detail of some of the repeatedly nucleated domains could be accounted for in terms of the strength of the nucleation centre.

4.3.1.2 Sample (II)

Sample (II) is the higher coercive film (H_c=139kA.m^{-1}) and its domain distribution around the M-H loop is shown in figure 4.6. The domain structure of this film shows broad similarities with sample (I) although as will be discussed below some significant differences did exist. Thus in the ac-demagnetised state, the domain structure could again be described as maze-like. However, upon closer examination, it was observed that the mean length along the domain wall before the direction changes, as well as the mean period (d=280nm), was significantly smaller than for the lower coercivity film (I). As expected, a much larger field (H_{ext}=140kA.m^{-1}) needed to be applied before any significant changes in the domain structure were observed. Following this, the same approach to saturation was observed, but was slightly more difficult to

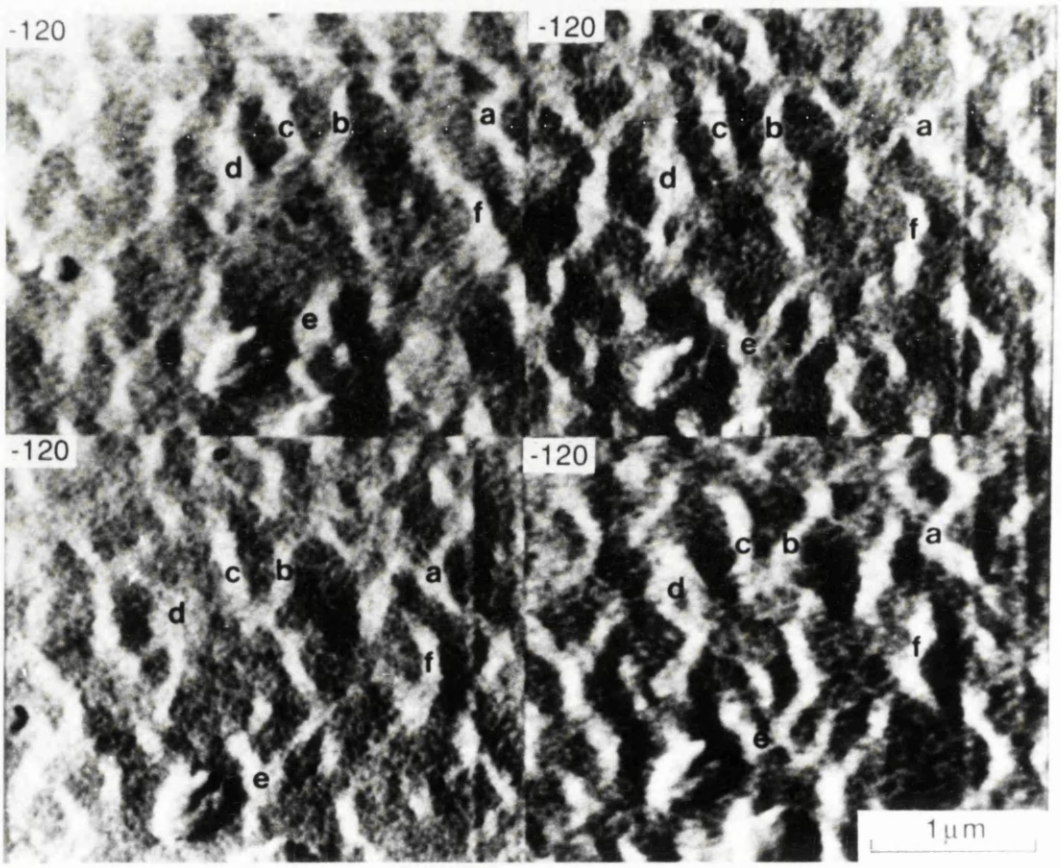

Figure 4.5 MDPC images of an area of sample 1 which was repeatably magnetised in the same direction with a field of 120kA.m^{-1}.

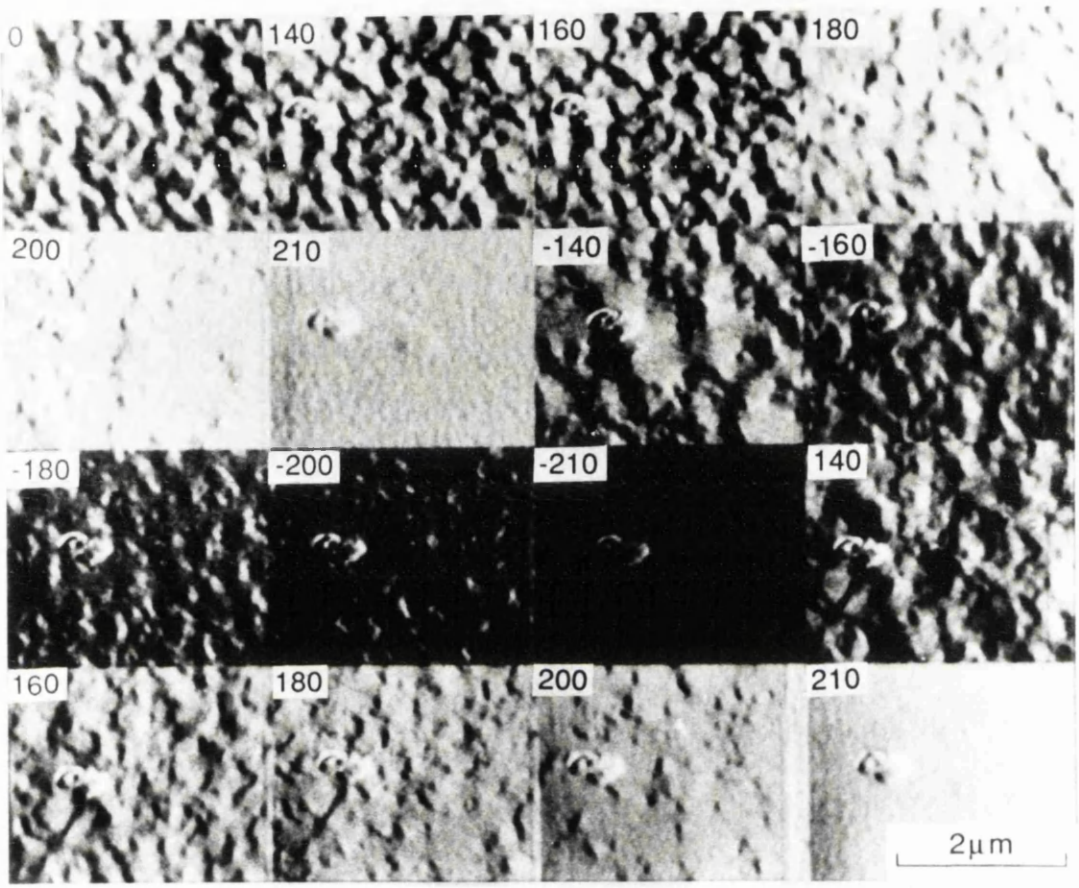

Figure 4.6 Montage of MDPC images taken at various positions around the remanence loop of sample H.

follow because of the reduced domain dimensions. Indeed a noteworthy feature of this film was its ability to support very small stable domains (after H_{ext}=200kA.m^{-1}) of size ≈50nm.

It is upon renucleation in the negative direction that the major difference between the two films was observed. Now a wide range of domain sizes were observed. Substantial local areas (up to 1μm in diameter) remain unreversed, whilst in other areas domains as small as 50nm (which stayed unchanged in the approach to saturation) could be observed. On application of a higher field (H_{ext}=-160kA.m^{-1}) previously unreversed local areas appear to switch rather than simply shrink as a result of growth of favourably orientated domains from already switched neighbouring areas. Such behaviour is once again indicative of strong wall pinning at a high density of local sites. After applying greater negative fields the domain structure acts in a similar fashion as in its approach to positive saturation. Once again very small domains are observed at H_{ext}= -200kA.m^{-1}

4.3.2 Determination of a remanence loop from a series of MDPC images

During the course of the in-situ experiments, figures 4.4 and 4.6 have shown that the domains within the multilayer grow and shrink according to the magnetic field applied. In order to compare the micromagnetic observations around the remanence loop with the actual bulk magnetisation curves of the films, a remanence hysteresis loop for each multilayer has been determined, with the help of some simple image processing, from the MDPC images in figures 4.4 and 4.6. A binary image for each MDPC image in the montages was created so that the area of magnetisation lying in each of the two directions could be measured from a histogram. An example of this is shown, for sample (I), in figure 4.7. Now it is possible to measure the net magnetic moment M, for each remanent state by summing all the areas which are designated as 1 in the binary image (ie where the magnetisation is parallel to the applied field, for instance) and subtracting the remaining areas (designated 0 in the binary images). Thus M can be expressed as:

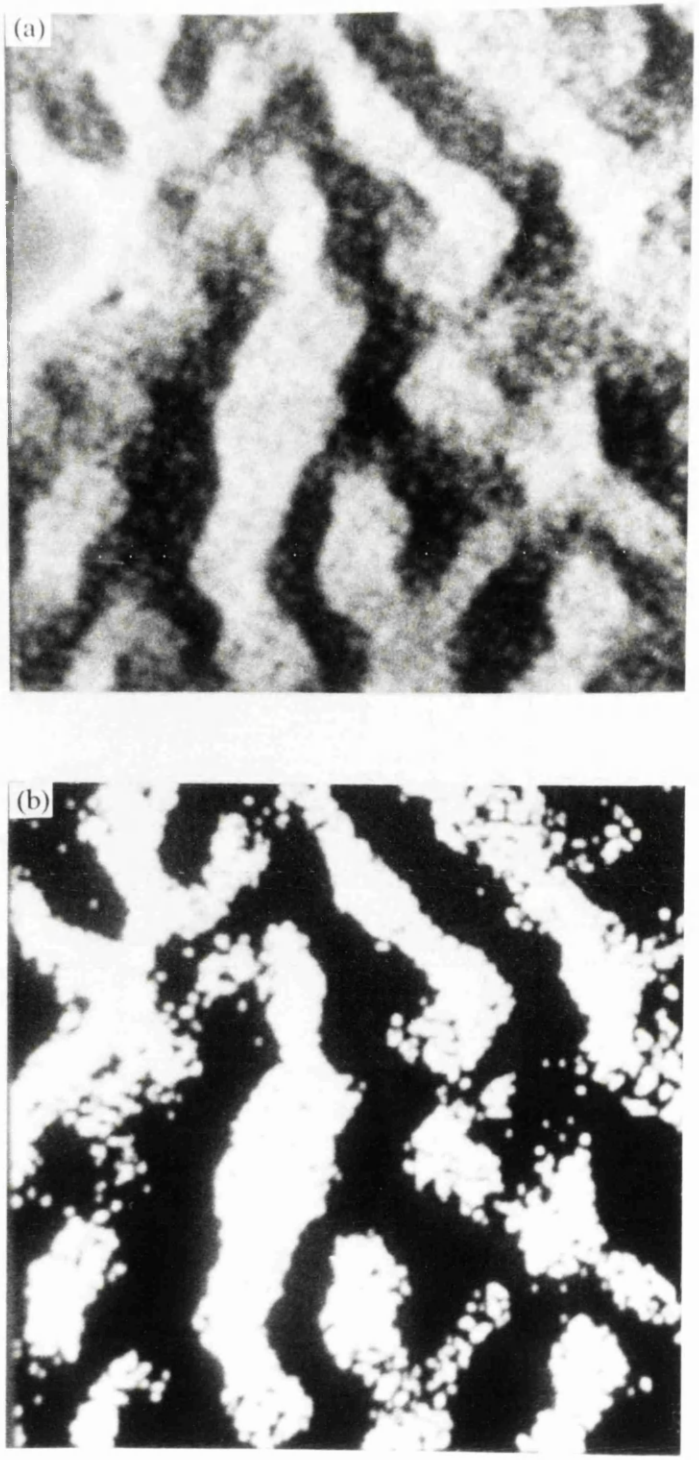

Figure 4. 7 (a) MDPC image of an area of sample 1

(b) Corresponding area transformed into its binary counterpart

$$M = \Sigma A_1 - \Sigma A_0 \qquad (4.1)$$

where A_1 denotes the area of domains lying parallel to the applied field and A_0 the area of those lying anti-parallel.

To produce the final remanence loop, this procedure was carried out for each applied field value and then M plotted as a function of the corresponding applied field. The loops for both films (together with the determined IRM curve) are presented in figure 4.8. The shape of the loops will be discussed in the next section.

4.4 Discussion

Both films exhibit the maze-like domain structure that has been observed for all Co/Pt ML investigated throughout this thesis. Such a domain structure, with its irregular boundaries, departs from the more usual stripe domain pattern seen in thin films and is a consequence of the strong perpendicular magnetic anisotropy.

As observed in sections 4.3.1.1 and 4.3.1.2 the domain walls do not always annihilate with comparable ease. Observations of this kind were made by Jakubovics (1991) who showed that for thin ferromagnetic films with in-plane magnetisation, the field required to annihilate a pair of 180° domain walls depends strongly on the sense of rotation of the spins in the domain walls bounding the domain about to collapse. Annihilation is likely to be easier to accomplish if the spins in the wall are parallel rather than anti-parallel. This is shown schematically in figure 4.9. for a pair Bloch walls separated by a domain about to collapse. This would seem to explain qualitatively the domain observations made here.

Although the montages of images shown in figures 4.4 and 4.5 show the development of the domain structure round the remanence loop, it is very difficult to observe what exactly is happening between each pair of images. One reason for this, is that the images are not exactly in registration, due to imaging difficulties. It is possible however, to align the images with some image

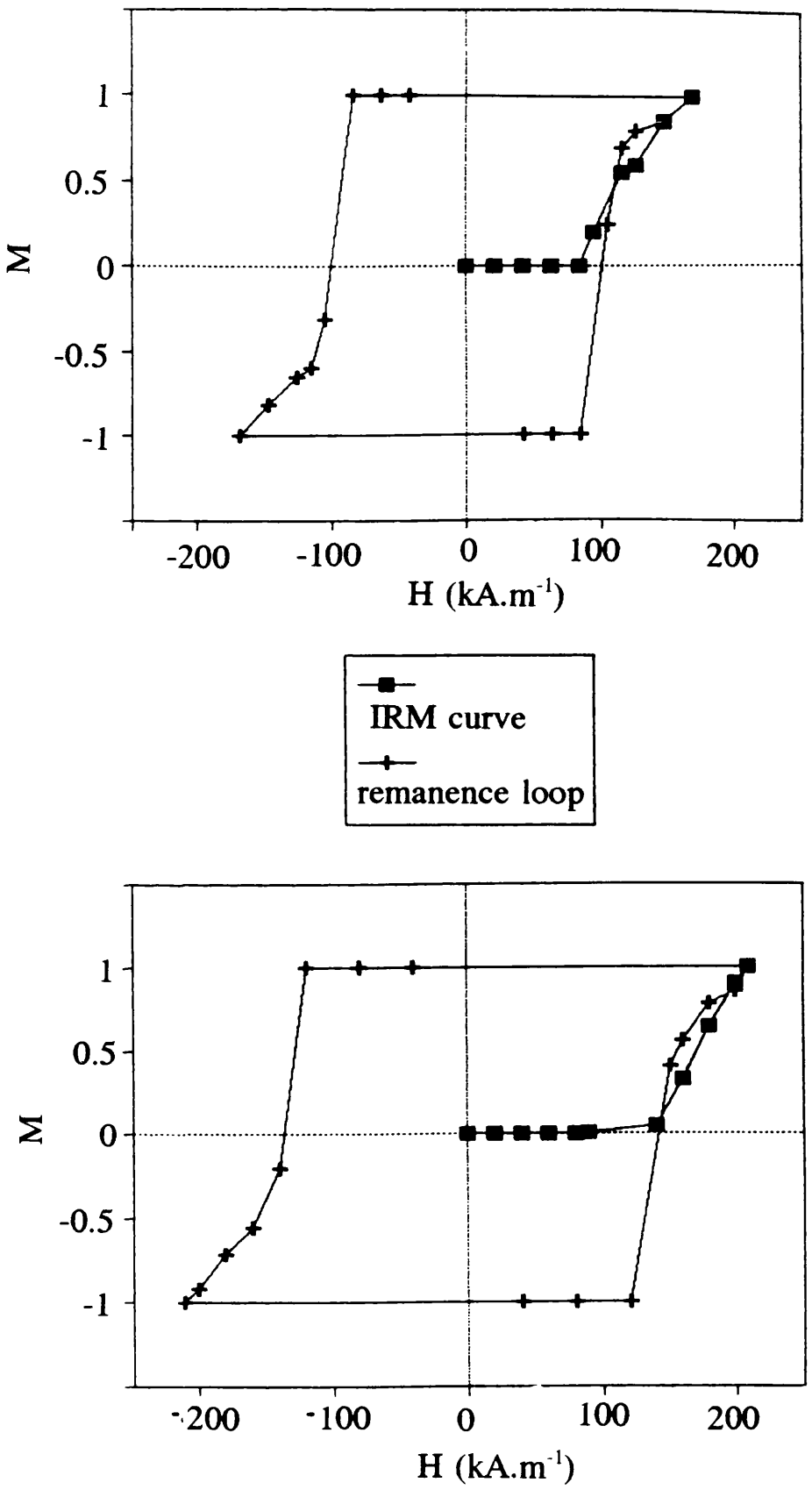

Figure 4.8 Remanence loops for both samples, constructed from the MDPC images presented in figures 4.4 and 4.6.

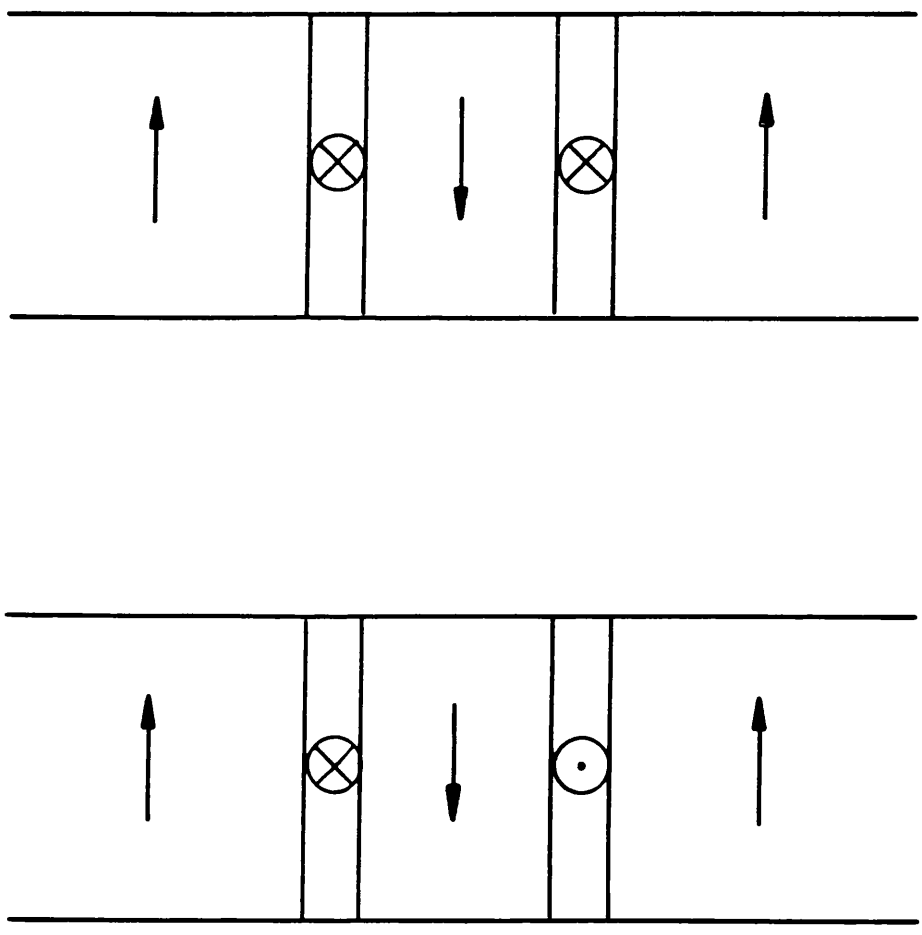

Figure 4.9 Schematic of domain annihilation, showing that it is easier to accomplish if the spins in bounding walls are parallel (top) rather than anti-parallel.

processing. This now allows the images to be observed one after the other (cine study) on the eXL and development of the domains closely examined. For sample I it is now clear that domain wall motion is indeed the reversal mechanism. It is less clear for sample II. Although this sample does have a platinum underlayer, it is too thin (1nm) to promote textured growth and the more particulate behaviour found in films with a thicker underlayer (Zeper 1991).

A measure of the consistency of the magnetisation reversal process can be gauged from comparing the last six images in each of figures 4.4 and 4.6 with the images from the initial magnetising process (from ac-demagnetised to positive saturation). They show what happens when the applied field is once again reversed and the films taken from negative through to positive saturation. The very similar domains that were nucleated after repeated magnetising of a local area, as shown in figure 4.5, were indicative of the existence of preferred nucleation sites within the film. Mansuripur (1987) found that for nucleation to arise in his model, "weak points" in the film needed to be included to start the reversal process. Such "weak points" in actual magnetic films are usually due to structural, rather than magnetic, defects.

The very small stable domains (≈50nm in diameter) which appear in sample (II) are an important consideration for MO recording on Co/Pt multilayers, since it shows that these multilayers can support very small domains. If the film could support written domains of this dimension then the recording densities would increase greatly.

The shape of the remanent loops produced from the MDPC images agree very well with the measured hysteresis loops from the AGFM. The shape of the loops, in each sample, were very similar. Both samples exhibit 100% remanence and rectangularity close to 1 as one would expect for a prospective MO medium. A very sharp nucleation point, where the first observation of domains across essentially the whole area of the films was found for both films. However to saturate the films fully much greater fields are required and this accounted for the tail on the loops.

4.5 Summary

Bulk magnetisation measurements on the multilayers were carried out using an AGFM. Following this, a series of in-situ magnetising experiments were undertaken in the electron microscope which closely simulated the fields to which the films had been subjected in the bulk measurements. The results from these loops show that bulk magnetic measurements are not always sufficient to distinguish the necessary characteristics of films and micromagnetic techniques are often required. The experiments provided considerable insight into the mechanisms that determine the shape of bulk magnetisation curves and could prove fruitful for investigations of a range of magnetic materials.

Chapter 5

Lorentz microscopy of thermomagnetically written domains

5.1 Introduction

The previous chapter dealt in detail with, the magnetisation processes of naturally occurring domain structures within artificial multilayers of cobalt and platinum. In this chapter we study thermomagnetically written domains in Co/Pt multilayers by Lorentz microscopy, while the energetics of such domains will be investigated in the next chapter. All three modes of Lorentz microscopy, Fresnel, Foucault and MDPC were employed, although the bulk of the work was carried out using MDPC because of its greater suitability for quantitative analysis. Most of the written domains were in the form of laser modulated spots, although a preliminary study of continuous lines was also undertaken.

Many other studies dealing with the observations of thermomagnetically written domains within MO media have been published and details of these are given below. The most commonly used techniques involve Kerr optical microscopy or the Fresnel mode of Lorentz microscopy (Ichihara et al 1988). The Fresnel mode allows all the basic geometrical data to be collected, but, as explained in chapter 2, prohibits any detailed quantitative results being attained. Kerr microscopy does not yield such high resolution, but one system (Clegg et al 1991) allows quantitative information such as bit size, signal level and signal to noise ratio to be extracted. More recently, van Kesteren et al (1991) used scanning magnetic force microscopy (SMFM) to observe written domains in Co/Pt multilayers. The greatest advantage of this technique is the possibility of using actual MO discs (upon which recording experiments can be carried out before imaging) without necessitating the removal of substrates. However it still cannot yield detailed analysis since the contrast mechanism is still not well understood. The resolution achieved by using SMFM techniques is typically ≈50nm. Aeschlimann et al (1990) used both Lorentz microscopy and SEMPA

to observe thermomagnetically written domains within TbFeCo. These two modes complement each other and it is possible to quantitatively analyse the magnitude and direction of the surface magnetisation using SEMPA.

The remainder of this chapter will show that MDPC microscopy is well suited to the task of imaging written domains in MO media. Better resolution is attained than that achieved with other domain imaging modes and because of the linearity of the technique, quantitative analysis can be carried out fairly easily.

5.2 Experimental writing details

This section deals with the experimental set-up at the Philips Research Laboratory for the writing of thermomagnetic domains in MO media. For direct observation in the electron microscope, the multilayers were deposited on a wafer of Si_3N_4 TEM windows as described in chapter 3. To record magnetic domains on the wafer, a modified MO Kerr microscope was used (Greidanus et al 1989) controlled by a personal computer. It is operated in the 'free running mode' because of the absence of pre-grooves in the wafer. The dimensions of the windows themselves are very small (side 200μm) and therefore transmission of the laser light through the window was used to properly position the window before writing commences. Various tracks were then written by mechanical positioning of the specimen. All of the thermomagnetic domains studied in this chapter were written by laser modulation and the static fields were applied using a coil supported by a soft iron core. An argon laser operating at 488nm was employed as the light source. Marks (domains) could then be written for different conditions (applied bias field and laser power).

5.3 Continuous lines

Continuous tracks were written on four films (A-D), whose composition and magnetic properties are summarised in Table 5.1. In all films, remanence was very close to unity, as required for prospective MO media. With the modified

Sample	A	B	C	D
T_{Co} (nm)	0.35	0.4	0.4	0.4
T_{Pt} (nm)	1.7	1.8	0.9	0.9
N	9	9	15	14
H_c ($kA.m^{-1}$)	63	70	64	90
H_s ($kA.m^{-1}$)	79	77	144	138
H_n ($kA.m^{-1}$)	56	60	49	82
M_s ($kA.m^{-1}$)	330	330	530	520

Table 5.1 Composition and magnetic parameters of the four multilayers with continuous thermomagnetically written lines.

MO recorder it was not possible to record with the laser continuously on. Therefore to write lines, the laser was pulsed at 50Hz, whilst moving slowly at a speed of $10\mu m.s^{-1}$. The pulse duration was 300ns and the beam moved a distance of 0.2μm between each pulse. This left marks (of the same polarity) overlapping each other and the appearance of a continuously written line. For each film, a perpendicular bias field of $25kA.m^{-1}$ was applied whilst tracks were written with laser powers ranging (in 0.5mW steps) from 2.0 to 6.0mW.

As was the case for all the films studied throughout this thesis, the tracks within the four Co/Pt ML were initially viewed in the CTEM using the Foucault and Fresnel modes of Lorentz microscopy. In order to view the tracks, it was important that their direction lay orthogonal to the tilt axis. Figure 5.1 is a Fresnel image of sample C showing all of the tracks written in this film. A Foucault image of a single track in sample A, mapping magnetisation perpendicular to the tilt axis is shown in figure 5.2. Its partner reveals no magnetic contrast due to the absence of a component of magnetisation in this direction. Little more than simple observations were possible from these two techniques; therefore, for more detailed imaging and analysis of the tracks, it was necessary to implement MDPC Lorentz microscopy in a STEM.

Each sample was positioned in the STEM such that when tilted about a horizontal axis on the viewing screen (typically through ≈20°) the tracks ran vertically. The same operating conditions were used for all four multilayers and are now described. The imaging lens was C1, a 500μm VOA was used as a spray aperture and the probe forming aperture was a 100μm SAA (giving α=0.5mrad). Using PSL settings of P1: off, P2: +6, P3: +8 gave good magnetic contrast in the final image. Three images were taken for each track; two mapping induction parallel and perpendicular to the tilt axis and one bright field image of the crystallographic features.

Figure 5.3 shows a typical MDPC threesome of a well defined track. As is clearly observed magnetic contrast is only visible in one image, due to the direction of the domains and tilt axis chosen. However, not all tracks are as well defined as the above. Figure 5.4 shows a set of images of 4mW tracks taken

Figure 5.1 Fresnel image of sample C, displaying all of the tracks written on this film.

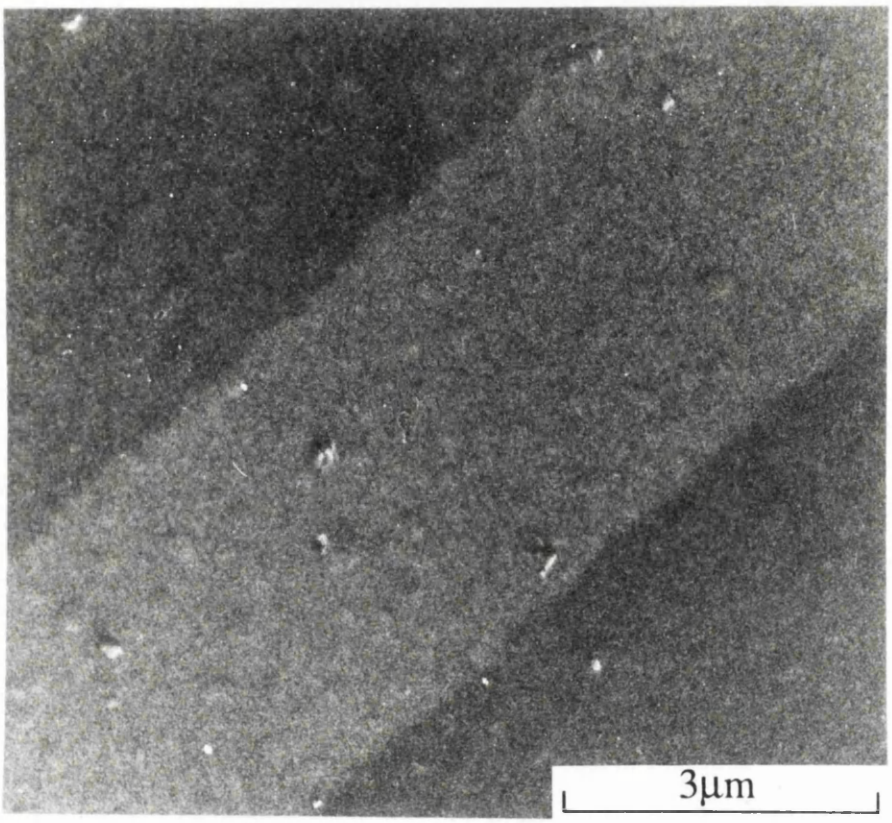

Figure 5.2 Foucault image of a single track in sample A.

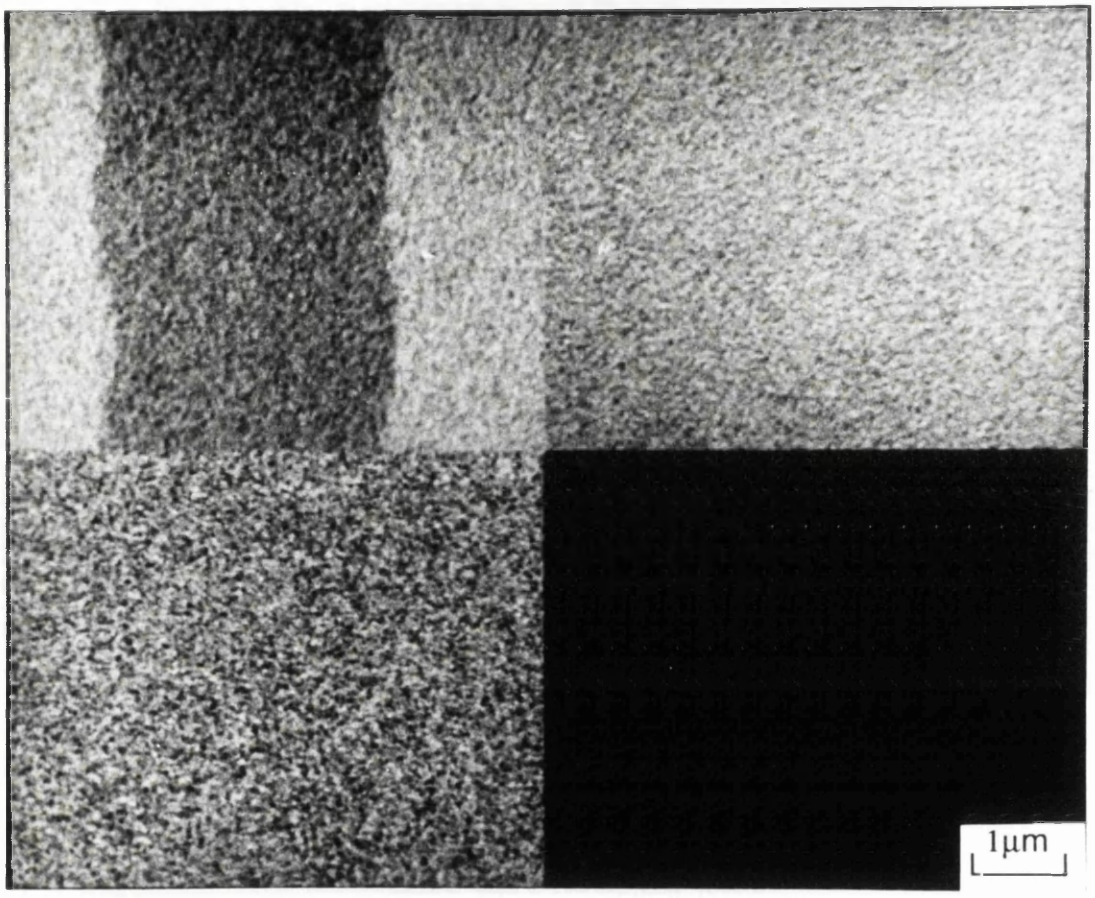

Figure 5.3 A typical MDPC threesome of a well defined written track from sample A.

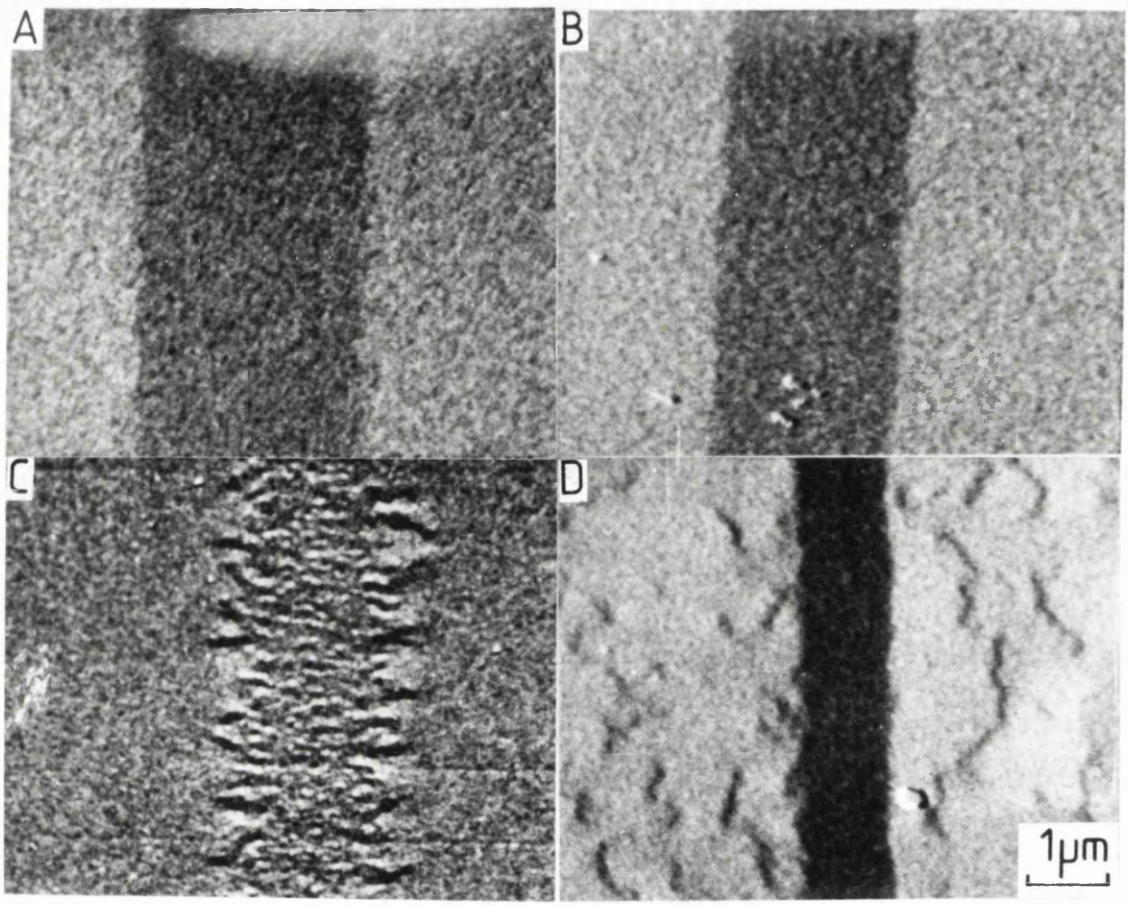

Figure 5.4 MDPC images of a 4mW tracks taken from each of the four multilayers (A-D).

from each of the four multilayers. Two of the samples show a tendency to form subdomains. Sample D had "wormlike" domains in the background region. A possible explanation for this phenomenon was incomplete erasure of the specimen before the writing took place. Such domains were observed in many remanent states of these films as shown in figures 4.4 and 4.6 from chapter 4. In contrast, sample C had many reverse domains within the written sector and an almost "zig-zag" transition region which appeared to support an appreciable in-plane component of induction (which could also be observed in its pair image). This was thought to be due to the sheared hysteresis loop of this sample, or degradation of the individual metal layers by the laser heating. In the other two cases a simple magnetisation distribution was observed in which the magnetisation direction was constant everywhere other than at the track edge where it changes abruptly from one orientation to the other.

From the MDPC images, measurements were taken of each track width and then plotted against the corresponding laser power. The results are presented in figure 5.5. It shows the expected monotonic decrease in track width with decreasing laser power (Greidanus et al 1989). The Curie temperature T_c, and the coercivity of the multilayer affect the width of a track written with a particular power. T_c increases for thinner platinum layers and smaller domains could be written for these multilayers at a given power. Similarly, the magnetisation within a multilayer with high coercivity is less easily switched, again resulting in smaller written domains. Both of these effects are displayed in figure 5.5. Also of interest was the width of the track when low laser powers are used. For the highest coercivity samples investigated, lines with dimensions of 0.5μm (the same order as those of the laser spot used to write the track) were observed. Only when the mean width fell below this figure did breaks appear in the track.

Although it has been possible to achieve some results from the imaging of these lines, information is not actually written in MO media in this manner. Usually it is in the form of laser modulated (LM) circular marks and the next section investigates these structures in detail.

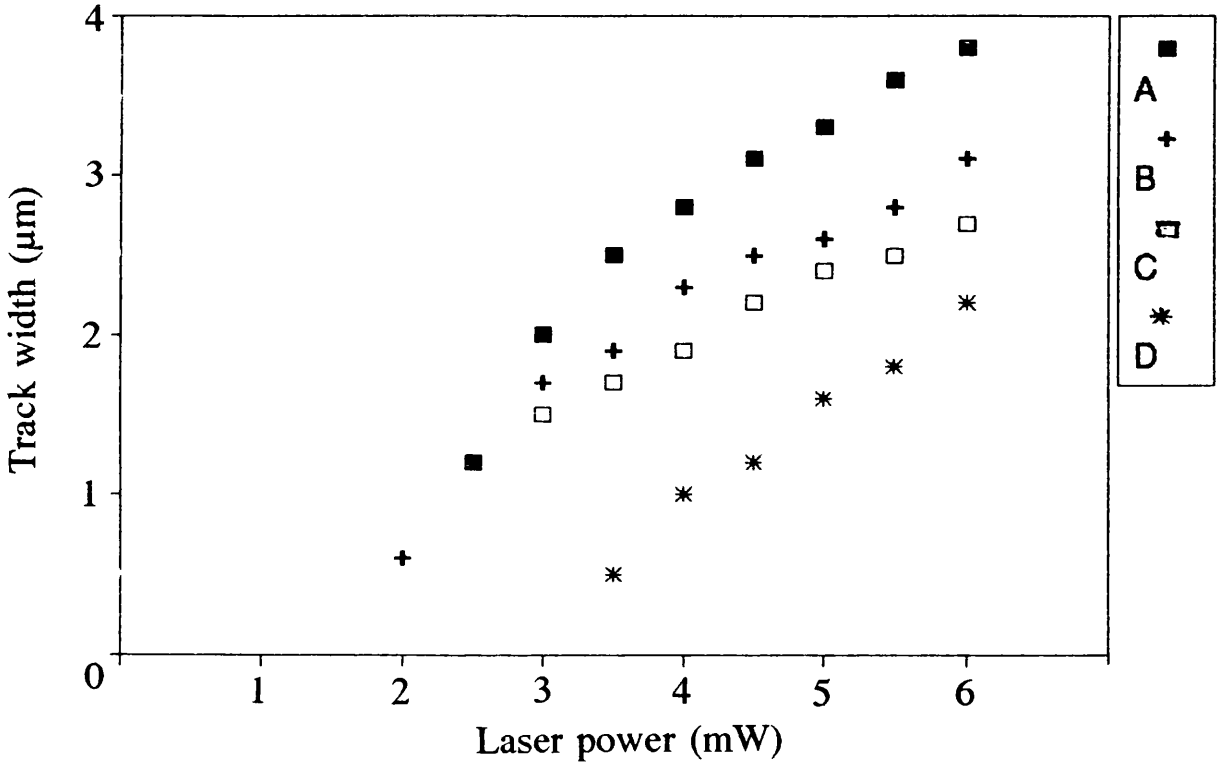

Figure 5.5 Track width as a function of laser writing power for all four samples (A-D).

5.4 Laser modulated marks

Laser modulated marks were written on two different specimens (E and F). The parameters for the two specimens investigated are shown in Table 5.2. To write LM marks involved different writing parameters than those used in the previous section. To leave discrete marks, the laser was pulsed at only 2Hz whilst moving at 17μm.s^{-1}. The pulse length was again 300ns and the marks were at a distance of 7μm from each other. Slightly modified MDPC STEM operating conditions were used to image these two multilayers, primarily due to the increased inelastic scattering arising from thicker TEM windows. The probe forming conditions were: C1, together with a 50μm SAA. Again a 500μm VOA was used as a spray aperture. A longer camera length was required, so the PSL settings for improved magnetic contrast were: P1: +6, P2: +6, P3: +8.

Marks were written in each film as a function of both the laser power and bias field. A number of properties of the written marks, which in real discs can affect noise contributions and therefore lower carrier to noise ratios (CNR), were investigated from the images acquired in the electron microscope. Through such a study it is hoped that optimised writing conditions may be found which improve the CNR.

5.4.1 Results

Figure 5.6 comprises a pair of low magnification MDPC images (sensitive to two orthogonal induction components) showing marks written with a laser power of 10mW in applied fields ranging from -10 to 50 kA.m^{-1} in sample E. The marks depart from the expected circular shape due to the necessary tilting of the specimen in the microscope. As well as strong contrast from the magnetisation within the written marks themselves, stray field contributions are clearly visible in the images around the edges of the marks. Similar marks were observed for sample F (figure 5.7), where the laser power used was 8mW. The contrast in the marks increases steadily with increasing bias field and was low

Sample	E	F
T_{Co} (nm)	0.35	0.4
T_{Pt} (nm)	1.08	1.5
N	15	10
H_c ($kA.m^{-1}$)	139	142
H_s ($kA.m^{-1}$)	247	251
H_n ($kA.m^{-1}$)	119	121

Table 5.2 Composition and magnetic parameters of samples E and F.

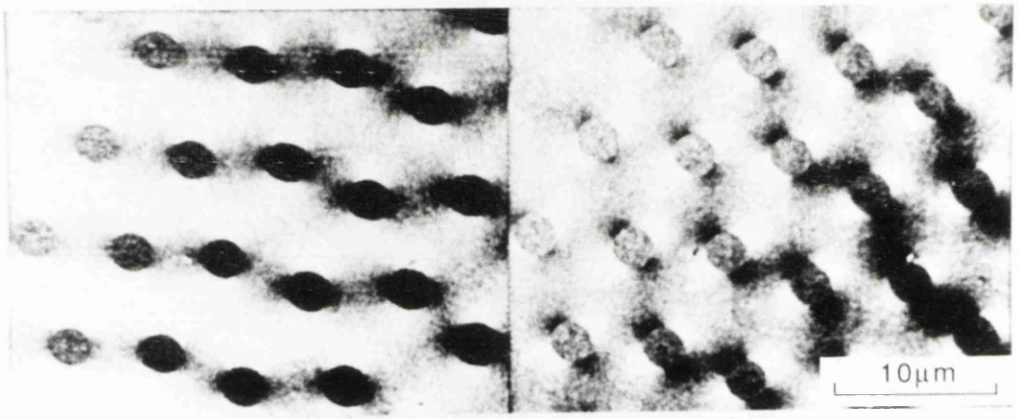

Figure 5.6 Low magnification pair of MDPC images showing marks written with varying laser powers and bias fields in sample E.

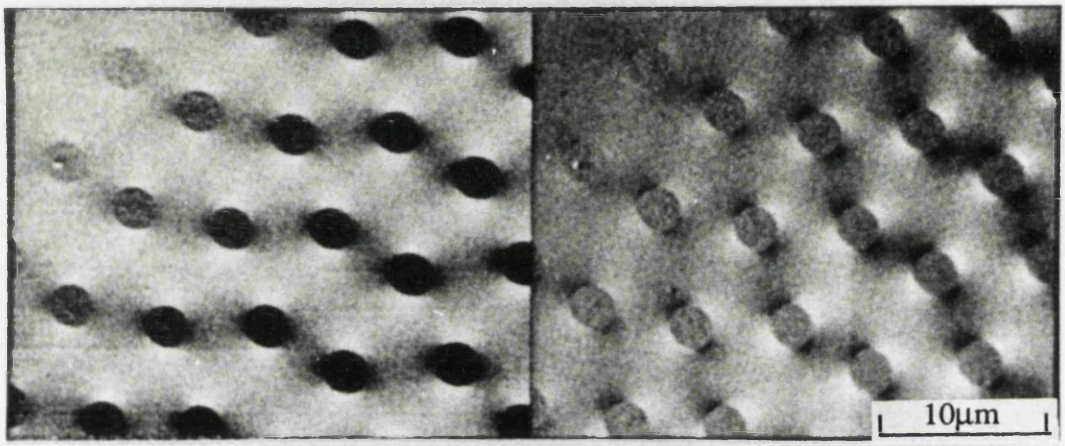

Figure 5.7 Low magnification MDPC images of marks written in sample F.

for marks with low or no bias because of the presence of reverse domains within the mark. The differences can be seen more clearly from the higher magnification images of figure 5.8, which show marks written with no bias and with a field of 50kA.m^{-1}. That writing occurs when no bias field is present is due to the high demagnetising field in the multilayers.

A detailed examination of a whole series of images of individual marks in both multilayers, confirmed that the mark size was weakly dependant on the applied field during writing. These results are presented in figure 5.9. Following Suits et al (1988) this suggests that the formation of these marks is dominated by nucleation processes whereby the writing process can be explained by a nucleation rather than bubble model. This will be discussed in the next section. More importantly however, it clearly shows that subdomains are present until the bias field exceeds 30kA.m^{-1}. Both of these findings are in accord with Greidanus et al (1989). This suggests the use of a high bias field to attain a sufficiently high CNR. However, as well as being uniformly magnetised, the geometry of the marks should be regular if the write noise is to be kept to a minimum. Whilst this appears to be the case for the mark seen in figure 5.8(a) it is not so for that in figure 5.8(b). Indeed the shape of the mark itself shows appreciable irregularity with departures from circularity on a scale of 200nm. Figure 5.10 shows the extent of the irregularity in high magnification MDPC images of a written mark. Furthermore, the extent of the irregularity increases with bias field. To explain in more depth the energetics of thermomagnetic domain formation, a discussion is given in a later section.

The written marks in both films were also studied as a function of laser power (the bias field in both cases was 25kA.m^{-1}). As in section 5.3, we found a monotonic increase in size with increasing laser power for the range of powers that were studied (4 -20mW). These results are shown in figure 5.11. For a particular laser power, the size of the mark was always larger in sample F. This was simply a consequence of the multilayer having a lower Curie temperature T_c, due to a smaller Co:Pt ratio. Figure 5.12 shows MDPC images of a mark from each sample written with a laser power of 8mW and bias field of

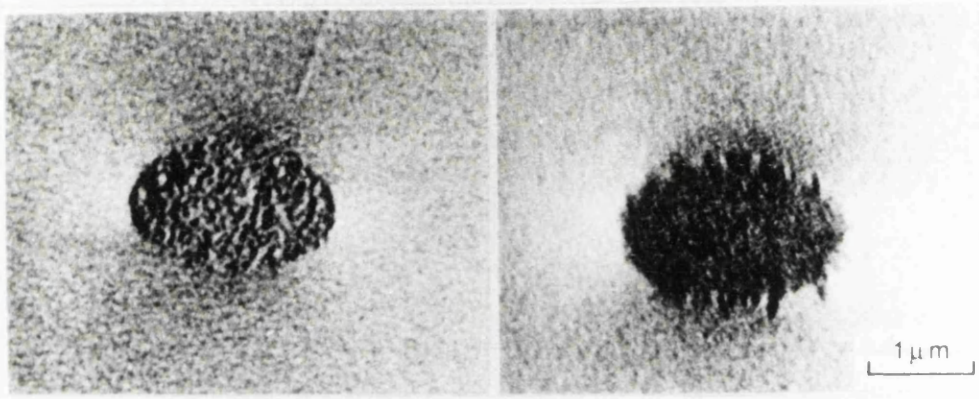

Figure 5.8 MDPC images of two marks in sample E written with bias fields of 0 and 50kA.m^{-1} respectively.

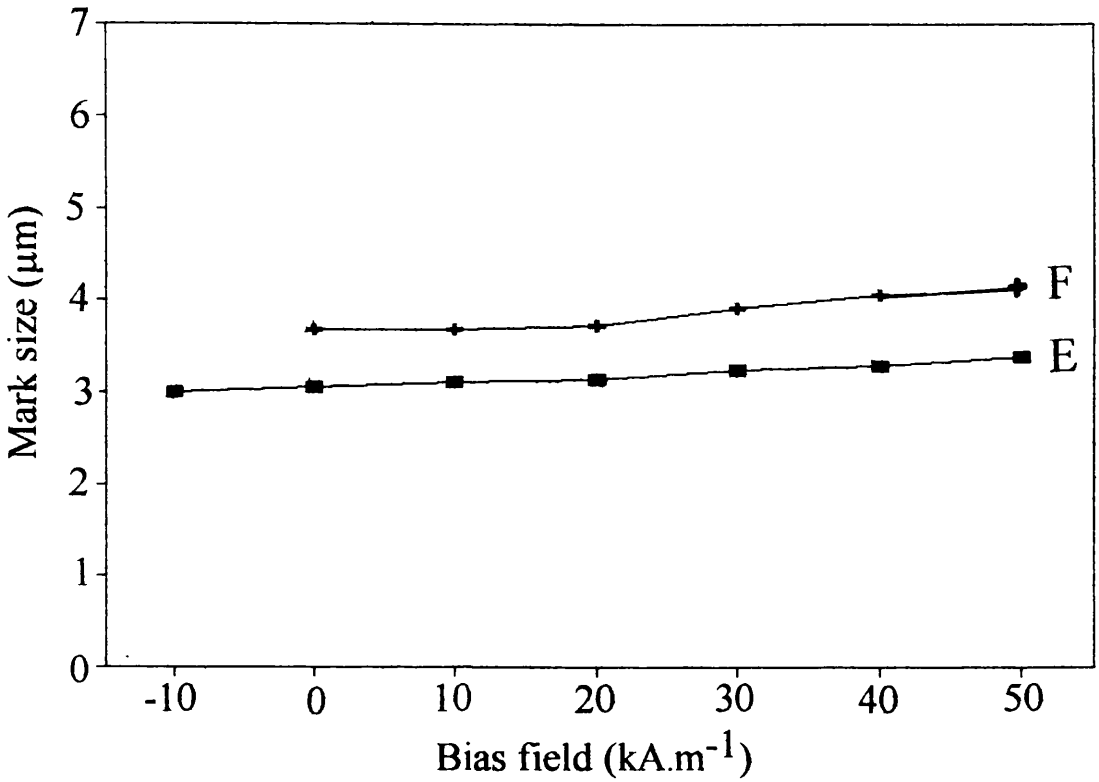

Figure 5.9 Mark size as a function of applied bias field during writing for samples E and F.

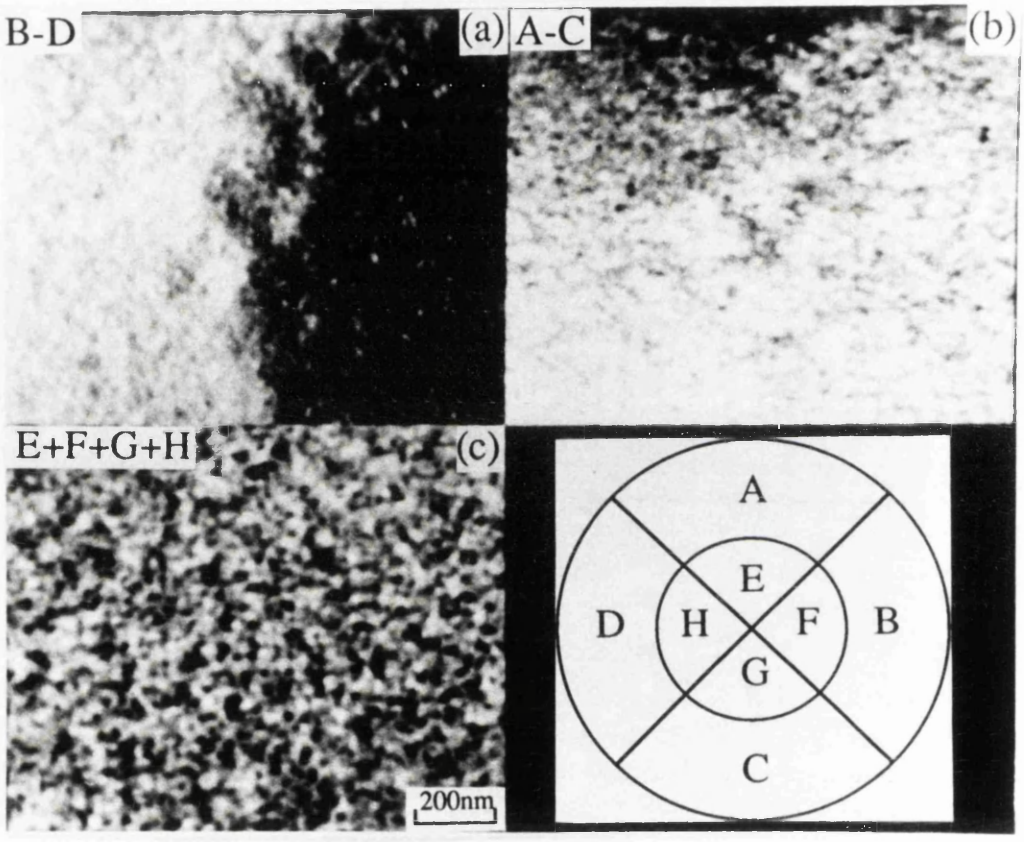

Figure 5.10 High magnification MDPC images of a written mark showing appreciable irregularity of the boundary.

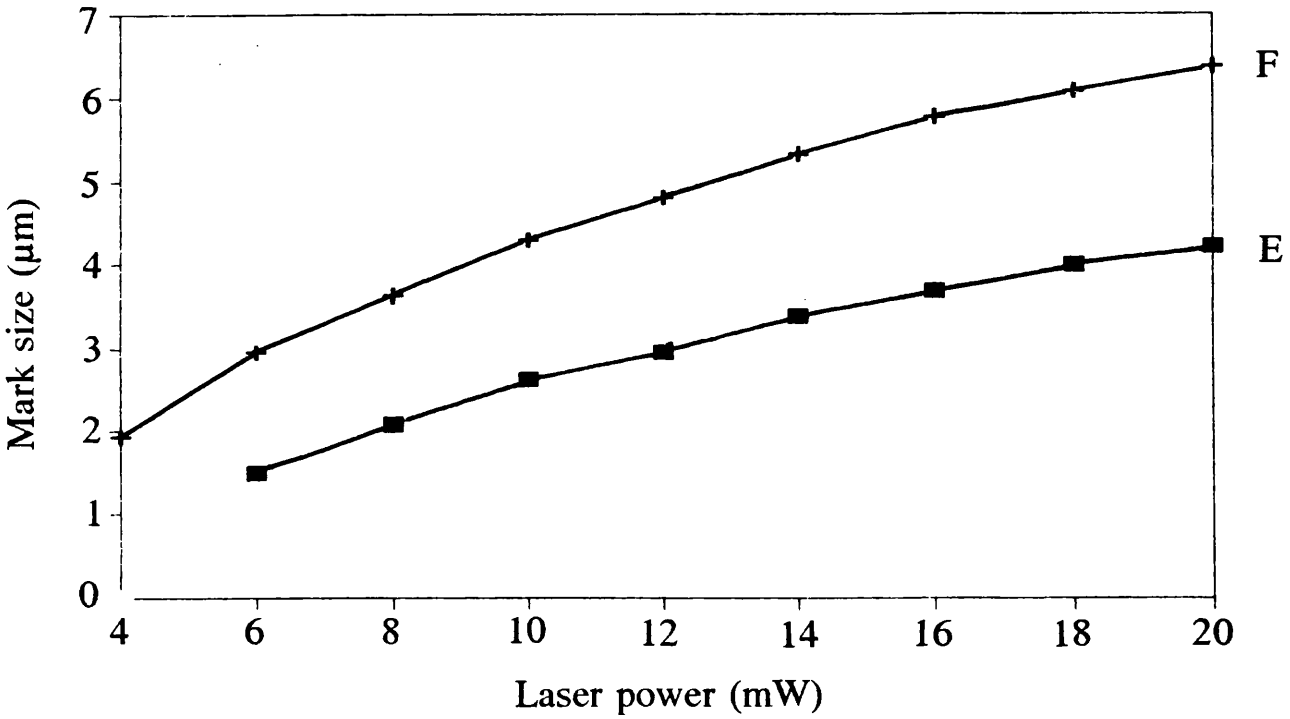

Figure 5.11 Mark size as a function of laser power for samples E and F.

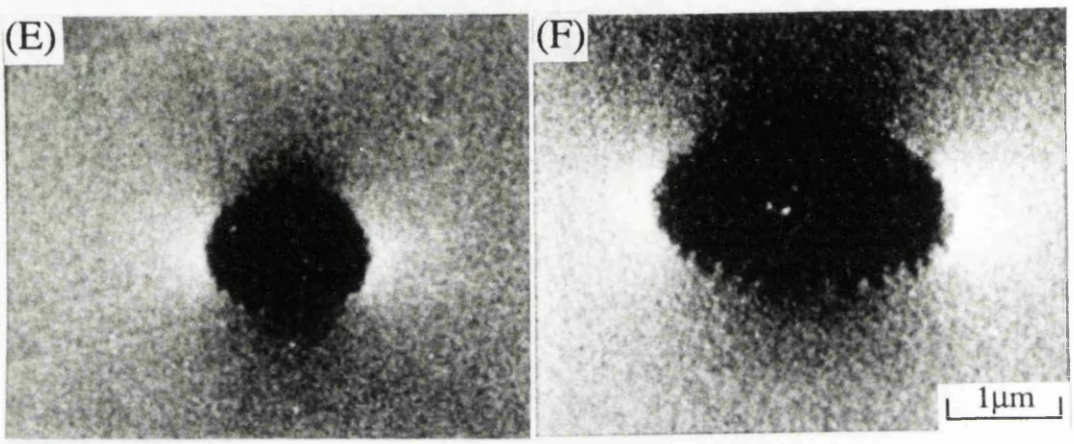

Figure 5.12 MDPC images of marks written with 8mW and 25kA.m^{-1} from each sample.

25kA.m^{-1}. When writing took place with a laser power equal to or greater than 10mW, an additional structure was observed in the centre of the mark, which was not magnetic in origin. Indeed, a bright field image of the same area (figure 5.13) clearly showed that in this region the higher laser power had caused annealing of the grains and brought about a growth in their size to ≈50nm, an increase of a factor of five.

All of the phenomenon discussed above are most clearly illustrated in figure 5.14, which presents all the written marks on sample E. The weak relationship between size and bias field, increase in boundary irregularity with increasing bias field, increase in size with laser power and additional structure in the marks at high laser powers can all be clearly observed.

5.4.2 Energetics of thermomagnetic domain formation

The process of thermomagnetic writing in MO media is controlled by the temperature profile of its magnetic properties, domain nucleation and domain wall motion. In order to understand the domain structures of written marks observed in MDPC images more fully, it is necessary to investigate these features.

Two models exist for the thermomagnetic writing process in MO films with strong perpendicular anisotropy. The first is a bubble model, developed by Huth (1974) and also used by Hansen (1987) and van Kesteren (1991), in which the multilayer is assumed to be a ferromagnetic layer with homogeneous magnetic properties. This is acceptable because we have seen from previous chapters that the Co layers are magnetically coupled through the non-magnetic Pt (ie the domain wall lie in the same lateral positions in each Co layer). Such a model assumes that the writing process can be described by domain nucleation followed by coherent rotation or domain wall motion.

From direct observations (Shieh 1987) it has been shown that domain nucleation occurs in the first 10-20ns of the laser writing pulse. Immediately after nucleation of the mark, the total force on the domain wall is given by the first derivative of the total energy of the system:

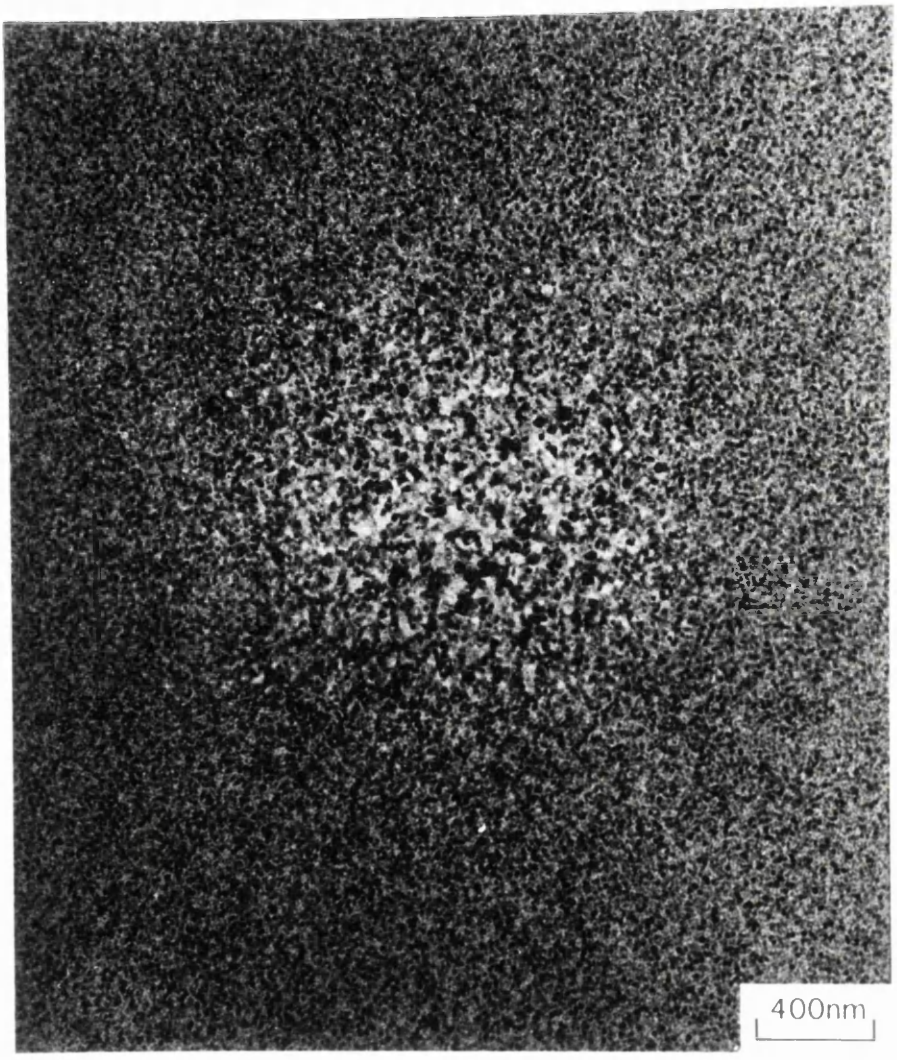

Figure 5.13 Bright field image of an area in which a mark has been written with too high a laser power, revealing a substantial increase in crystal size.

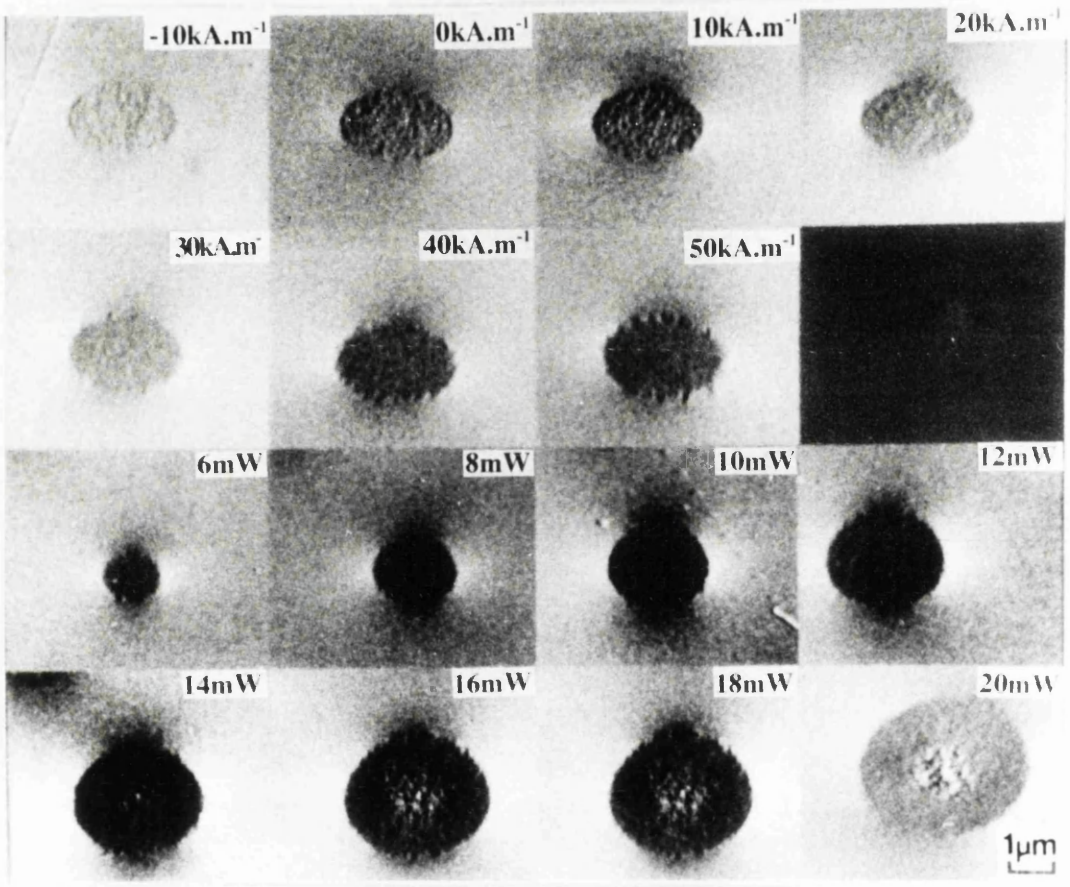

Figure 5.14 MDPC images of marks in sample E, written with varying bias fields and laser powers.

$$F = \frac{\delta}{\delta r}(E_w + E_H + E_D) = F_w + F_H + F_D \qquad (5.1)$$

where E_w is the domain wall energy, E_H the externally applied field energy, E_D the demagnetising energy and F_w, F_H, F_D the corresponding forces. Expressions for these energies are given by Hansen (1987). To understand the process of domain wall motion following nucleation of a mark, the forces acting on the wall must be considered. For a cylindrical domain, whose radius is equal to or larger than the film thickness, the total force is then, to a good approximation, given as:

$$F(T) = \frac{\delta E(T)}{\delta r} = 2\pi h\left[-\sigma_w(T) + 2r\mu_o HM_s(T) + \frac{h\mu_o M_s^2(T)}{(1+3r/2h)}\right] \qquad (5.2)$$

where σ_w is the domain wall energy density, M_s the saturation magnetisation, r the radius of the domain, h the ferromagnetic layer thickness, H the applied field and T the temperature.

The three terms in (5.2) equate to the forces relating to the domain wall, applied field and demagnetising energies. The wall term is negative and tends to shrink the domain whilst the other two terms represent an expanding force on the domain wall. After the magnetisation has been switched, the position and diameter of the written mark will be frozen if the total force on it is less than the coercive force. For Co/Pt multilayers the coercivity falls to zero at a temperature of ≈50°C below T_c (Greidanus et al 1989). Therefore it is possible for domains nucleated just below T_c to be unstable, allowing for domain wall motion, which would result in an irregular mark boundary. As the area cools down, a position will eventually be reached where the total force was less than the coercive force and the mark would be become fixed in that position.

It should be noted that the bubble model is only valid when the writing process can be described by the expansion or contraction of a single circular domain wall. This is clearly not the case in many of the written marks in Co/Pt

multilayers where subdomain behaviour was observed. To account for this type of behaviour, Suits et al (1988) introduced a nucleation field model. Now nucleation of microdomains is permitted at a number of sites within the heated region. With larger bias fields applied during writing, the density of these sites increases until the mark becomes a single domain. This phenomenon was observed in both samples E and F, where subdomains were present in the marks until the writing field exceeded $\approx 30 kA.m^{-1}$.

5.5 Edge Analysis

For data recording purposes, it is important that the geometry of the written marks is consistently circular in order to reduce further noise contributions. From the MDPC images already shown in this chapter, it is clear that at the present this is clearly not the case. It is important therefore to have some means of quantifying this degree of irregularity or boundary jaggedness by a single figure of merit pertaining to the domain wall shape. Bernacki and Mansuripur (1991) have already suggested that measuring the fractal dimension of the boundary wall can provide such a figure of merit.

This section now outlines another method that is being attempted using edge reconstruction techniques on digital electron images. This has been carried out in collaboration with our colleagues at the Department of Statistics, University of Glasgow. The procedure is explained below.

An original MDPC image of a written mark (figure 5.15 (a)) was split into four columns and using a parametric approach (Qian and Titterington 1992) edges were detected within each column. These were then recombined and an image is formed (figure 5.15 (b)) showing the original mark with the edge indicated. We now wish to know quantitatively how much this edge departed from the elliptical shape (due to tilting) expected. Therefore an ellipse was fitted to the edge shape (figure 5.15 (c)). For every point around the edge, the distance d between the point (x,y) and the ellipse (x_e,y_e) on a line through the centre of the ellipse is measured. This distance is then minimised (by Newton-

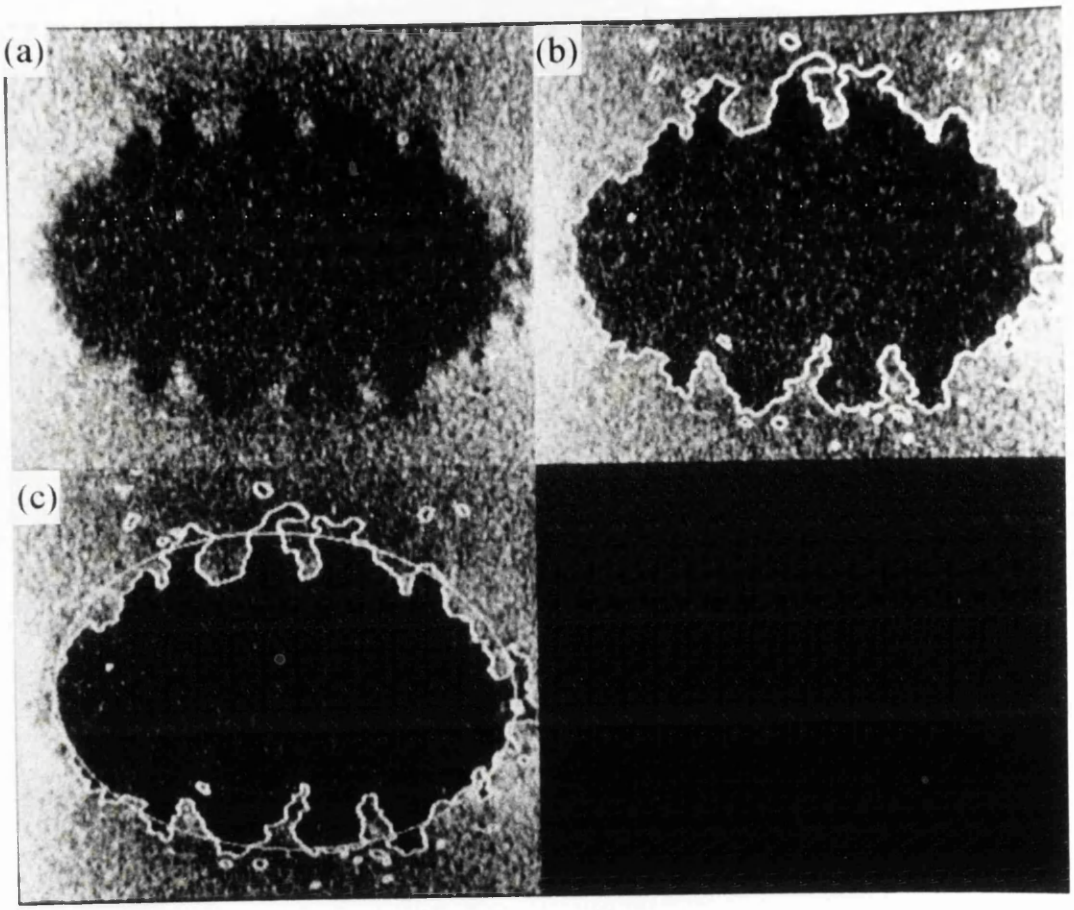

Figure 5.15 Images showing the steps involved in carrying out the edge analysis from the original image.

Raphson method) to give $\underline{d}$ which represents the average distance between the edge points and the ellipse. It is this value that is then used as the single figure of merit for the domain wall jaggedness. It is hoped that this method can be applied to series of marks written in MO media and will be discussed in more detail in the final chapter.

5.6 In-situ magnetising of written domains

Chapter 4 described a series of experiments in which the detailed magnetisation distributions, that occur naturally within the multilayers, were examined in a number of remanent states. This was achieved by subjecting the films to magnetic fields using the objective lens of the STEM. Also of interest is how written domains (both continuous lines and discrete marks) behave when subjected to similar magnetic fields as in chapter 4. This section reports on such an experiment on sample E.

The procedure for magnetising the marks was exactly the same as that performed in chapter 4. A suitable and easily recognisable mark was chosen. A magnetic field was applied for a short time and then the mark was imaged to check for any changes in its form or size. The marks written in the film investigated all had boundaries which departed from the expected circular shape. It may have been expected that the marks would grow (or shrink) in a monotonic fashion with applied field, but it was observed that as the magnitude of the field increased domains grew from the more irregular areas of the boundary and that a constant general growth was not noticed. Lin et al (1988) reported that ragged domain walls in MO media could be attributed to local variations in coercivity. This would help to explain why domain growth occurred initially only at the ragged regions. Domains also started to grow in the background region at higher fields. Figure 5.16 shows how the domains grow from the initial written state until a state of saturation was reached. Once in a state of saturation, the direction of the magnetic field was reversed. It was not possible to renucleate the mark because the writing process had not

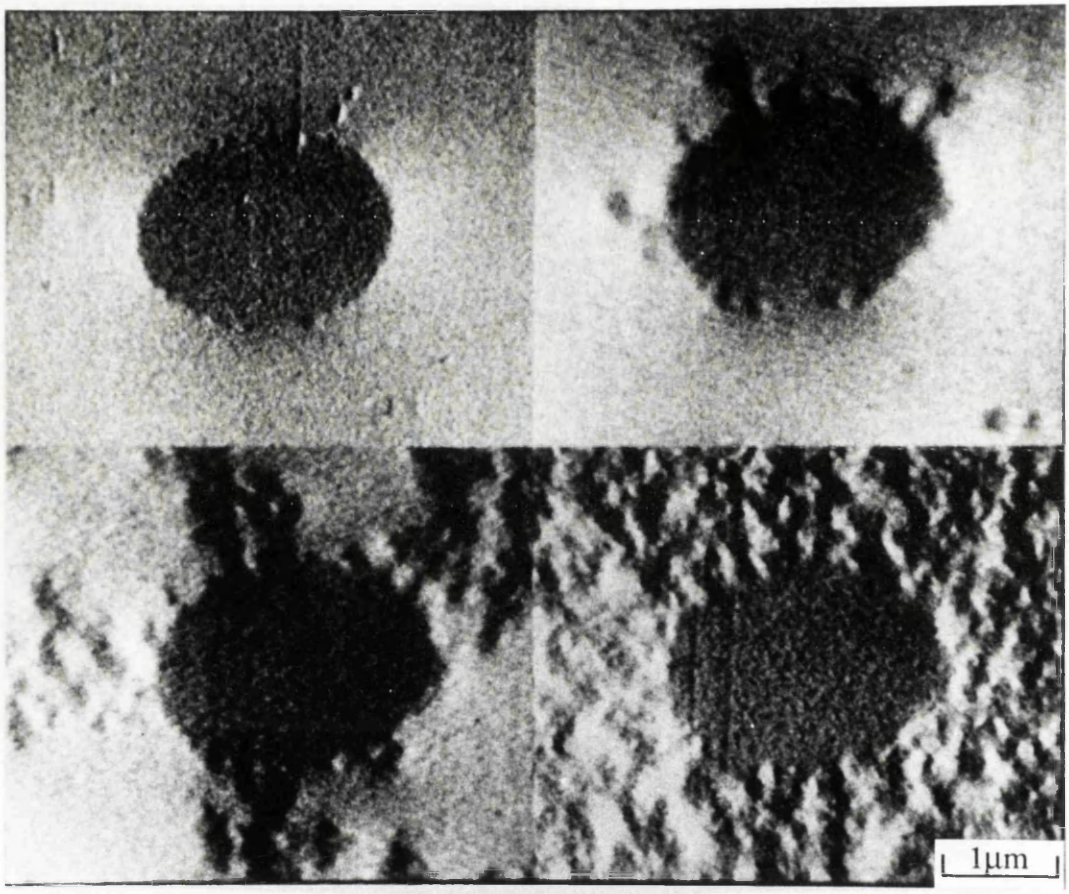

Figure 5.16 Four MDPC images showing how a written domain in sample E grew when subjected to increasing external magnetic fields.

influenced the physical structure of the film, and therefore not induced any change in the magnetic parameters. Marks such as that in figure 5.13 retain a magnetic memory when magnetised in different directions, because of the change in their magnetic structure.

5.7 Quantitative analysis of recording performance

The carrier to noise ratio is an important characteristic of any recording medium, as its increase is related to improved recording performance. To optimise the CNR, all sources of noise should be reduced or, if possible, eliminated. In MO recording media, the carrier signal is directly related to the Kerr rotation (and therefore the magnetic moment of the mark) of the written marks from within the film. Therefore the shape and internal structure of the written domains are important quantities which directly affect the signal levels recorded. Usually test recording experiments on MO media measure the CNR by writing at a single frequency and analysing both the carrier and noise levels with a spectrum analyser (Zeper 1991).

The experiment that was carried out in Glasgow attempted to relate the observations of signal levels from MDPC images of individual marks (written with different bias fields) to parameters relevant to the recording performance of similar films. This was done by calculating average pixel values from various positions in the digital MDPC images. The multilayer that was quantitatively analysed was sample E from section 5.4. The analysis was carried out using the image processing software available with the Link eXL acquisition system. Figure 5.17 is an aid to the analysing process. The average pixel values from an area within the written mark and in the background region (well away from all stray field effects) were calculated from histograms of each area. The standard deviation of the value was also determined. The quantity (denoted S) that we were interested in was the difference between these two values, normalised by the current in the electron probe (taken from a bright field image). S is therefore proportional to the magnetic moment of the mark, as

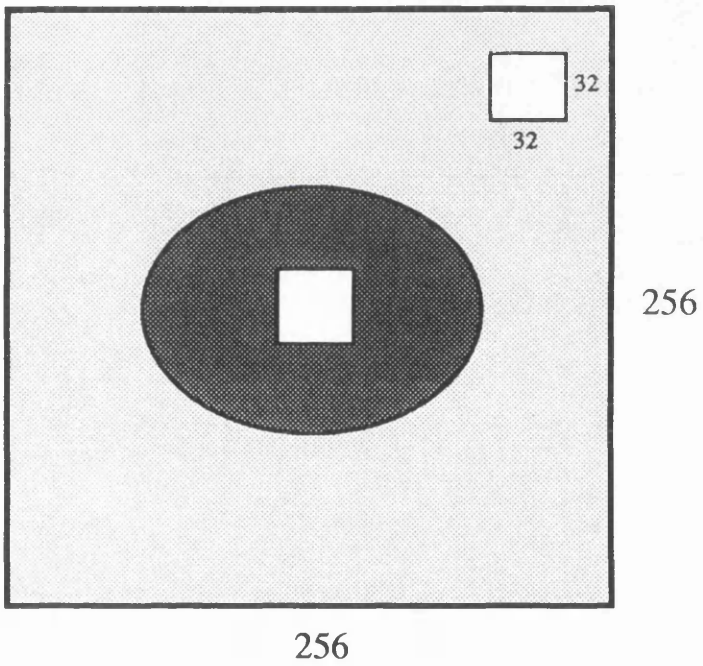

Figure 5.17 Schematic aid to the analysing process. From a 256^2 pixel image, two 32^2 pixel boxes are created, one inside the written mark and one on the background region. It is from within these areas that the average pixel values are gathered.

indeed is the carrier signal in a MO recording experiment. Figure 5.18 shows how S varies with bias field for the multilayer under investigation, together with the MDPC images from which the analysis was taken. For bias fields $\geq 40kA.m^{-1}$ S begins to level off and reach saturation. However for lower fields, S fell considerably and this reduction could be attributed directly to the formation of subdomains within the written marks. The shape of the curve was similar to the carrier variation measured in recording experiments detailed by Greidanus et al (1989). In their experiments, of course, the irregularity of the written mark also contributed to the noise levels and in theory would result in a lower recorded CNR. This analysis, is then further evidence that a high bias field ($>40kA.m^{-1}$) is necessary in order to reduce noise contributions from areas with reversed magnetisation.

5.8 Summary

The results from this chapter have shown that MDPC microscopy is well suited to the investigation of thermomagnetically written marks. Higher spatial resolution is achieved than is possible with other observational techniques and this allowed detailed analysis of the important features of the marks to be carried out. Quantitative analysis pertaining to the signal levels in each mark was undertaken with considerable success and a method for measuring the degree of boundary irregularity was also suggested.

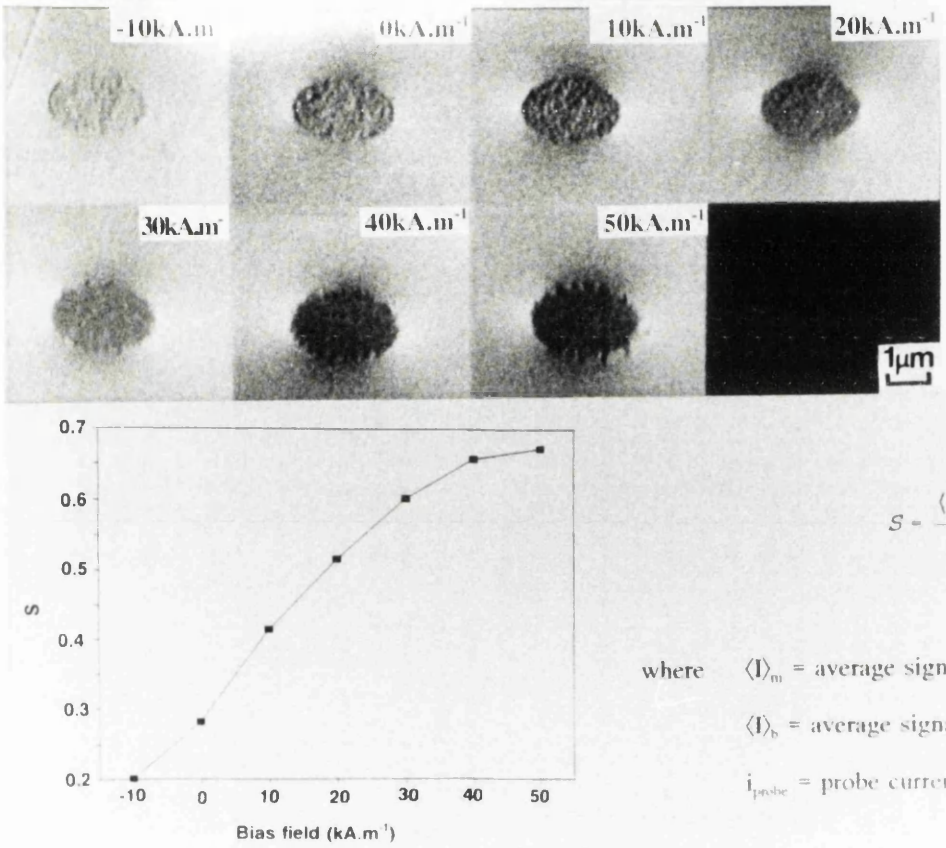

$$S = \frac{\langle I \rangle_m - \langle I \rangle_b}{i_{probe}}$$

where $\langle I \rangle_m$ = average signal level in a mark

$\langle I \rangle_b$ = average signal level in background

i_{probe} = probe current

Figure 5.18 S as a function of applied bias field, together with the MDPC images which yield this result.

Chapter 6

Domain wall energy calculations in Co/Pt multilayers

6.1 Introduction

The domain wall energy density σ_w, is an important recording characteristic of any magnetic or MO recording material. As explained in section 5.4.2, σ_w plays a significant role in determining the final state of the magnetisation within a thermomagnetically written mark. It also helps to determine the shape and size of naturally occurring domain structures. In this short chapter, the wall energy density is evaluated for a variety of multilayers, including the two films investigated in chapter 4. The insights gained from these values are also discussed. The method attempted in the search for σ_w made use of the classical Kooy and Enz model (Kooy and Enz 1960), adapted for multilayer structures (Draaisma and de Jonge 1987). This model was used to relate a characteristic magnetic length τ of the multilayer to the period of the stripe domain pattern observed from Lorentz microscopy.

6.2 The Kooy and Enz model

Wielinga (1983) and Bernards and Schrauwen (1990) showed that Co-Cr layers with low coercivity and suitable for perpendicular magnetic recording purposes could be described well by the Kooy and Enz model. Using this model, it was possible to infer the width of stripe domains in the film from the slope of the M-H hysteresis loop. Draaisma and de Jonge took a step further and modified the original model to take into account multilayer structures. The next section outlines how the model was adapted. The original model assumes that the homogeneous magnetic layer will have the following properties:

- uniaxial perpendicular magnetic anisotropy
- uniform thickness and infinite lateral dimensions
- a stripe domain structure (no closure domains) with 180° walls

- domain walls which are freely mobile (ie coercivity effects are neglected)

When a multilayer with N bilayers, consisting of a ferromagnetic layer of thickness t and non-magnetic layer of thickness s is encountered a further property is assumed:

- domain walls will be at the same lateral positions in each magnetic layer in order to reduce magnetostatic energy.

Figure 6.1 is a schematic of the resulting domain structure found in a multilayer which has all the above properties.

The net magnetisation within such a multilayer is,

$$\overline{M} = \left[\frac{d_1 - d_2}{d_1 + d_2}\right] M_s \tag{6.1}$$

where M_s is the saturation magnetisation within each domain.

The magnetic volume energy density of the domain structure contains three terms, magnetostatic E_d, domain wall E_w and applied field E_h energies. All three terms are normalised to the maximum magnetostatic energy $0.5\mu_o M_s^2$.

The magnetostatic energy can be written as,

$$e_d = \frac{E_d}{\frac{1}{2}\mu_o M_s^2} = m^2 + \sum_{n=1}^{\infty} \frac{4}{(n\pi)^3} \frac{d}{t} \sin^2\left[\frac{1}{2} n\pi (m+1)\right] f_n(d) \tag{6.2}$$

where

$$f_n(d) = 1 - \exp\left(-2n\pi \frac{t}{d}\right) + \frac{\sinh^2[n\pi(t/d)]}{\sinh^2[n\pi(D/d)]} \tag{6.3}$$

$$X \left\{\frac{1}{N}\left[1 - \exp\left(-2n\pi \frac{ND}{d}\right)\right] - \left[1 - \exp\left(-2n\pi \frac{D}{d}\right)\right]\right\}$$

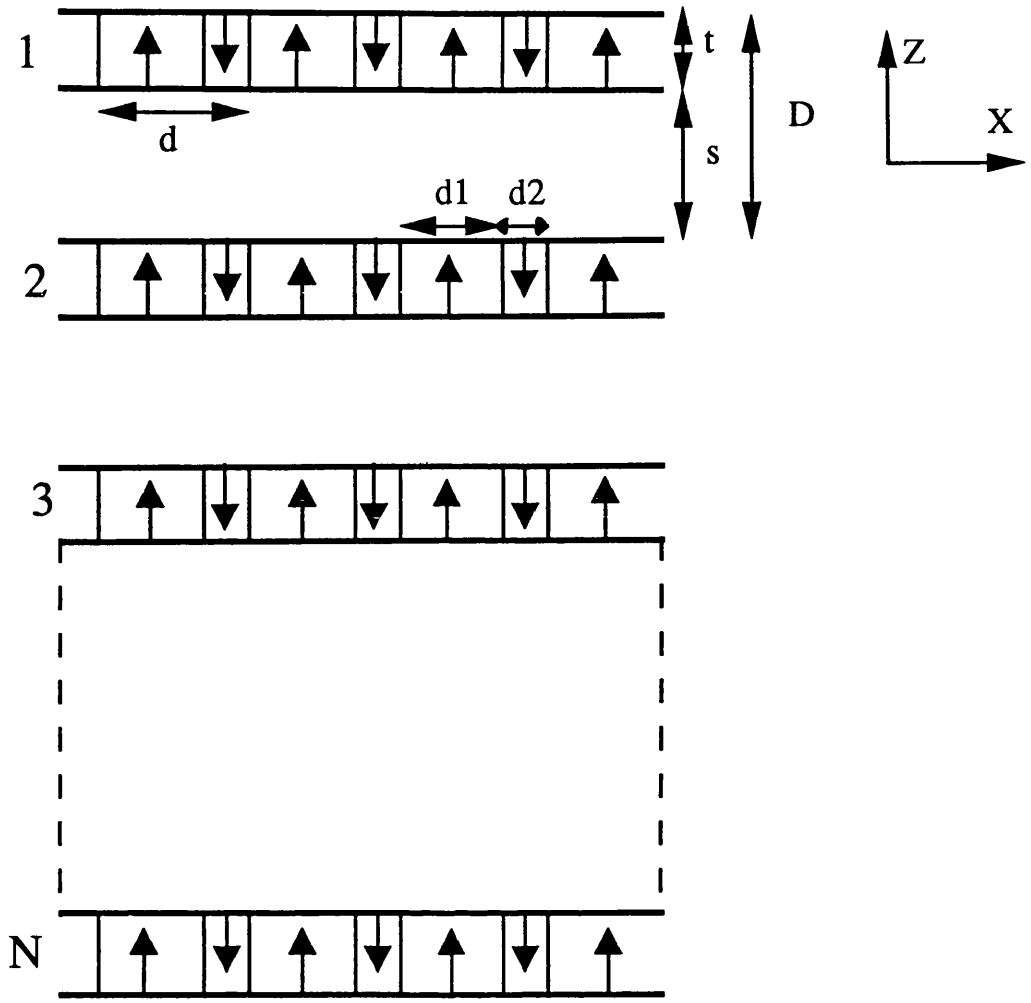

Figure 6.1 Schematic of magnetic domain structure which arises in a multilayer with perpendicular anisitropy consisting of N bilayers.

with $m=M/M_s$ as the relative average magnetisation. It should be noted that with N=1 this expression is in full agreement with that derived from the original model. A full explanation as to how equation (6.4) arises is given by Draaisma and de Jonge.

The domain wall volume energy density is expressed as

$$e_w = \frac{E_w}{\frac{1}{2}\mu_o M_s^2} = \frac{2\sigma_w}{d(\frac{1}{2}\mu_o M_s^2)} = \frac{2\tau}{d} \tag{6.4}$$

where σ_w is the specific wall energy and

$$\tau = \frac{\sigma_w}{\frac{1}{2}\mu_o M_s^2} \tag{6.5}$$

τ is a characteristic length of the magnetic material.

Finally, the applied field volume energy can be written as

$$e_h = \frac{E_h}{\frac{1}{2}\mu_o M_s^2} = \frac{-\mu_o HM}{\frac{1}{2}\mu_o M_s^2} = -2hm \tag{6.6}$$

where $h=H/M_s$ is the normalised field.

The total normalised energy density is $e=e_d+e_w+e_h$. If attention is restricted to films whose domain structure is in an equilibrium configuration and which is situated in zero field, the expression for the magnetic energy density contains only two terms, e_d and e_w. To try and achieve such an equilibrium configuration, the films were ac-demagnetised. By minimising the total energy density with respect to the domain repetition period d, the following expression can be obtained:

$$d = \left[\frac{2\tau}{\left(\frac{\partial e_d}{\partial d}\right)}\right]^{\frac{1}{2}} \tag{6.7}$$

From the above equation, d is expressed as a complex function of all the physical parameters (t, D and N) of the multilayer and the magnetic characteristic length τ. From this expression, it was then possible to evaluate the domain wall energy density σ_w for a film where all these parameters are known.

6.2.1 Procedure for evaluating σ_w

As explained above, the domain repetition period d, is a complex function of many variables when the energy density is minimised; therefore the calculating process was carried out using a simple Fortran program (program name: domain). The initial data given to the program was the cobalt layer thickness t, the bilayer thickness D and the number of bilayers N. An iterative calculating procedure was required ($\approx$5000 iterations needed) and the final result gave τ as a function of d for a given set of film parameters. To tie in with the experiments carried out in chapter 4 and to give more insight into the magnetising processing within the two multilayers, this approach was used to obtain values for the two films studied in chapter 4. For samples I and II with domain repetition periods of 280 and 370nm respectively, the calculations gave values of τ of 5.3nm and 6.7nm.

Before accepting the values of τ, it should be noted that not all of the assumptions made in section 6.1 hold for magneto-optical media, in particular Co/Pt multilayers. From torque measurements it is clear that these films have strong perpendicular anisotropy. The thickness is also expected to be uniform. The work presented in chapter 3 showed that the domains in each cobalt layer did lie in the same lateral position.

However, it should be noted that the real domain structures involve somewhat irregular maze-like domains rather than straight stripe domains, resulting in a slight change in the magnetostatic energy contribution to the overall energy density in the ac-demagnetised state. Chickazumi (1964) calculated magnetostatic energy densities for stripe and checkerboard domain patterns. He found that the latter resulted in a reduction of $\approx$38% in the magnetostatic energy

density. Moreover Goodenough (1956) found that the magnetostatic energy density of a wavy domain pattern (such as that seen in the Co/Pt multilayers) was more closely related to the checkerboard than the stripe pattern.

Furthermore, the Kooy and Enz model (and also the modified version by Draaisma and de Jonge) assumes freely mobile domain walls which was clearly not the case for Co/Pt multilayers as the magnetising experiments in chapter 4 demonstrated. This latter fact may not however, be of great importance as we had confined our attention solely to the ac-demagnetised state and, provided that this was a true energy minimum, the above analysis should not depend on whether the walls can move freely or not.

To check the applicability of the model, a different approach was adopted by studying a series of Co/Pt multilayers (of which sample II was the second in the sequence) which had the same bilayer composition (t, s and D the same in all films) but increasing numbers of bilayers (N) in the stack. The set of multilayers investigated all had a bilayer composition of (0.35nm Co + 1.0nm Pt). The number of bilayers N was in the range 7-75, resulting in overall film thicknesses from ≈10-100nm.

The process was undertaken for 6 films with N=7, 15, 30, 45, 60 and 75 in the stack. The domain repetition period d for each multilayer was measured directly from a series of Lorentz images. These values are shown as a function of N in figure 6.2 (a). From the calculations performed using the same algorithm as for samples I and II, d was then plotted as a function of N for various values of τ (τ=4, 6, 8, 10)nm and presented in figure 6.2 (b). It can be seen that the experimental curve lies between the theoretical curves for τ=6 and 8nm. By using smaller increments of τ, it was possible to attain a more detailed analysis and this is shown in figure 6.3. From these results, the best fit to the experimental results was obtained when τ=6.7nm. This value was in excellent agreement with the figure quoted for sample II in the previous section.

The final stage to calculating σ_w is simply found by manipulating equation 6.6 and multiplying τ by $0.5\mu_o M_s^2$. Initially, the saturation magnetisation of bulk cobalt (≈1400kA.m^{-1}) was used in the calculation, but following measurements

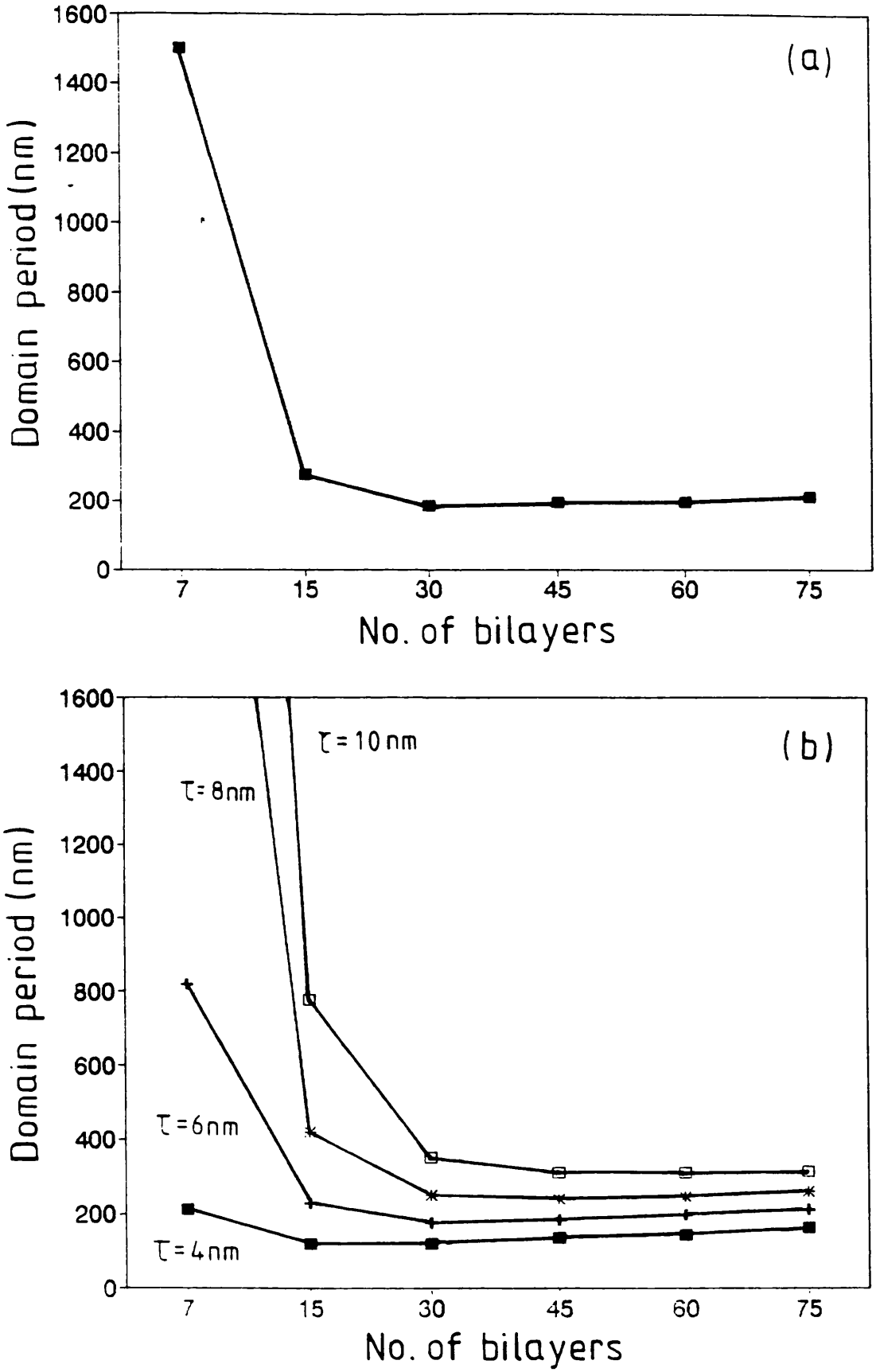

Figure 6.2 Experimental domain periods (a) compared with those calculated, using different values of τ, from the modified Kooy and Enz model (b).

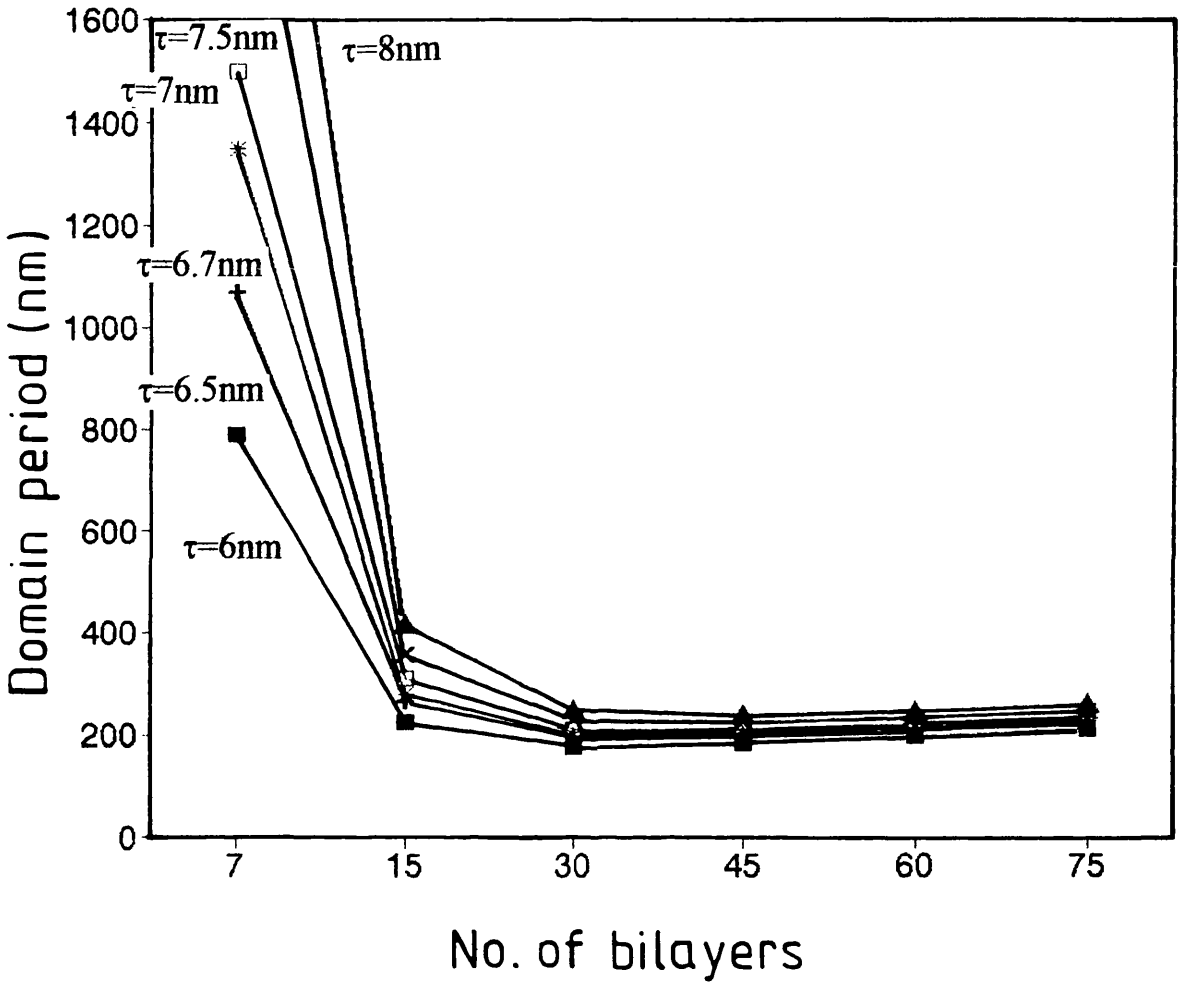

Figure 6.3 More detailed analysis of the calculated domain periods using smaller increments of τ.

carried out at Philips, it was clear that this value was too low and an increased figure was required. The actual values were 1920 and 1750kA.m^{-1} for samples I and II respectively. This was in good agreement with the findings of Lin et al (1991) who found that Co/Pt multilayers with more than a monolayer of cobalt (>0.2nm) in the bilayer had an increased (≈30%) saturation magnetisation. The enhancement is attributed to the magnetisation contributed by the polarised platinum atoms next to the cobalt layer (Schutz et al 1990). Using such an enhanced value of M_s allows the domain wall energy per unit area of cobalt to be calculated. The values obtained for each film were 12.3 (I) and 12.9mJ.m^{-2} (II). If it is accepted that the wall structure is Bloch like, then σ_w is given by:

$$\sigma_w = 4\sqrt{A.K_u} \tag{6.8}$$

where A is the exchange stiffness constant and K_u is the anisotropy energy density of the film.

With the known domain wall energy densities given above and the anisotropy energy from table 4.2, it is possible to relate the findings in terms of the exchange stiffness constant from equation 6.8. From the calculations, the values of A obtained for samples I and II were 1.3x10^{-11} and 1.0x10^{-11}J.m^{-1}. These values compare well with the exchange stiffness constant measured from bulk cobalt of 1.3x10^{-11}J.m^{-1} (Tannenwald and Weber 1961). The consistency of the results of this section and their agreement with the work of others suggests that this was a viable method for estimating domain wall energy densities in Co/Pt multilayers.

6.3 Magnetising written domains to calculate σ_w

The method described in this section for the calculating of domain wall energies in MO media by the application of external magnetic fields was first proposed by Mansuripur (1989). In his paper, thermomagnetically written circular domains (of radius r) were subjected to external magnetic fields and from Kerr observational techniques, the fields H_1, at which expansion and H_2 for the

contraction of the domains could be determined. Mansuripur calculated the outward forces on the domain and equated the two terms at the onset of expansion and contraction. With the cancellation of all terms involving the coercive force, a simple expression for the wall energy density was arrived at, from which it is possible to calculate σ_w from experimental data.

$$\sigma_w = 6\pi h M_s^2 + M_s r(H_1 - H_2) \tag{6.9}$$

In the experimental set-up at Glasgow, the field from the objective lens was once again used to apply external magnetic fields. The experiment was carried out for both continuous lines and discrete marks. As presented in section 5.6 (figure 5.16), the marks did not expand uniformly; instead domain wall motion only seemed to occur (initially at least) from the most irregular parts of the boundary. The same phenomenon was observed for the lines. The walls became more ragged before any expansion was noted. This type of behaviour made it impossible for us to make us of this method for estimating domain wall energies in MO media.

6.4 Summary

By balancing the domain wall and magnetostatic energy contributions of the multilayers it was possible to model domain periods in a low energy configuration and achieve a close fit with the experimentally measured domain periods. The results compared well with those from other authors. It was found unlikely that the method of Mansuripur could be used to estimate domain wall energy densities for these films.

Chapter 7

A comparative study of Co/Pt multilayers by SMFM and DPC

7.1 Introduction

Atomic force microscopy (AFM), first developed by Binnig (1986), is a new imaging technique with applications in many branches of science. It is capable of imaging conducting and insulating materials with atomic resolution. Its operation is based upon measuring the small forces which exist between a sharp tip (positioned on the end of a cantilever spring) and an object, which are placed close enough to each other so that the forces may be measured. Different types of forces may be measured, depending on the object being imaged and its separation from the tip. If the tip and object are in contact (or within a few angstroms) with each other, then it is possible to measure repulsive atomic forces. The nature of this force may be attributed to the Pauli exclusion principle, since at such close proximity the outer electron shells of the tip and object will overlap. In non-contact modes, longer ranges forces such as electrostatic (Martin et al 1988) and van der Waals (Martin et al 1987) may be measured. The above modes of force microscopy are generally employed to image surface topology of an object. However, if a ferromagnetic tip is used, then magnetic forces acting between the tip and a magnetic material may also be measured. The forces can be measured in two modes, static or dynamic. In the static mode, the force acting on the tip causes a deflection which can be measured by a sensitive motion detector. In the dynamic mode, a vibration is induced in the cantilever and the forces result in a change of the cantilever's resonance frequency, which is detected by interferometry, piezoelectrically or capacitively. In general, a control loop keeps the measured force at a constant value and an image is built up by scanning the surface of the sample below the tip in a regular raster.

Scanning magnetic force microscopy (SMFM) (Grütter et al 1992) is based on a modification of the AFM technique and has emerged as an effective method for observing magnetic domains with a resolution approaching that of many other magnetic imaging techniques (10-100nm) (Hobbs at al 1989, den Boef 1990). It was first implemented by Martin and Wickramasinghe (1987) to observe the contrast arising from a magnetic recording head. More recently, the technique has been widely used to image domain patterns which have been recorded for information storage. This is because it is possible to image the domain patterns in real tapes or discs with SMFM and relate the observations to recording characteristics such as carrier and noise levels. Such studies have been carried out on longitudinal CoPtCr media (Rugar et al 1990), perpendicular CoCr media (Bernards and Schrauwen 1989) and TbFe MO media (Martin et al 1990).

This chapter now deals with the instrumentation of a SMFM built at Philips Research by den Boef (1991) and the imaging of Co/Pt multilayers with this microscope. The results are then compared with DPC images of similar multilayers.

7.2 The scanning magnetic force microscope

The two main modes for the detection and measurement of magnetic forces are: measuring the constant force between the tip and object (static) or measuring the constant force gradient (dynamic). The stray field from the magnetic object attracts or repels the tip. In the constant force mode this deflection is measured with a very sensitive displacement detector (which must be able to measure motion in the sub-nanometre range). A control loop is then used to keep the force constant while the object scans below the tip in a regular raster.

The microscope used in this study has been described in detail by den Boef (1991). It is operated in the constant force gradient mode, in which the force gradient between the tip and specimen is kept constant by adjusting the tip-object separation. This mode of operation is preferred, because it offers better

sensitivity to long range magnetic forces (Binnig at al 1986). Magnetic forces can either be attractive or repellent, but the control loop in a SMFM responds properly only to attractive forces. Therefore, to insure a net attractive force that increases in magnitude as the object approaches the tip, a voltage U_b, of 2-3V is applied between the tip and the object. A spatially varying force (the force gradient) alters the effective spring constant of the vibrating cantilever (typically 0.1-1.0 N/m), resulting in a small change in its resonance frequency ω_r. From the theory of mechanical vibrations, it is known that:

$$\omega_r \propto \sqrt{K_c} \tag{7.1}$$

where K_c is the spring constant of the cantilever. As a result of the force gradient, the resonance frequency ω_r^1 of the cantilever is now given by:

$$\omega_r^1 = \omega_r \left(1 - \frac{K}{2K_c}\right) \tag{7.2}$$

where ω_r is the resonance frequency without any external force gradient and K is the shift in spring constant. For an attractive force, K is positive and the resonance frequency is then lowered. The shift K, can be measured by vibrating the cantilever with an angular frequency ω_e, which is usually slightly greater than ω_r ($\approx$10kHz for this microscope), and detecting the change of phase of the vibration. The vibration of the cantilever is sensed by interferometry and a control loop maintains a constant force gradient by adjusting the tip-sample separation. A schematic of the microscope used throughout this project is shown in figure 7.1 and its operation is explained below.

The object is mounted upon a xyz piezo-scanner and a sharp tip positioned on the end of a cantilever is placed in close proximity to it. Unlike most other SMFM, this microscope uses a copper plate to excite the cantilever, instead of a piezoelectric crystal. The copper plate, which is electrically isolated from the cantilever and has a sinusoidal voltage applied to it (frequency $\omega_e/2$), is brought close to the cantilever. The copper plate and the cantilever are capacitively

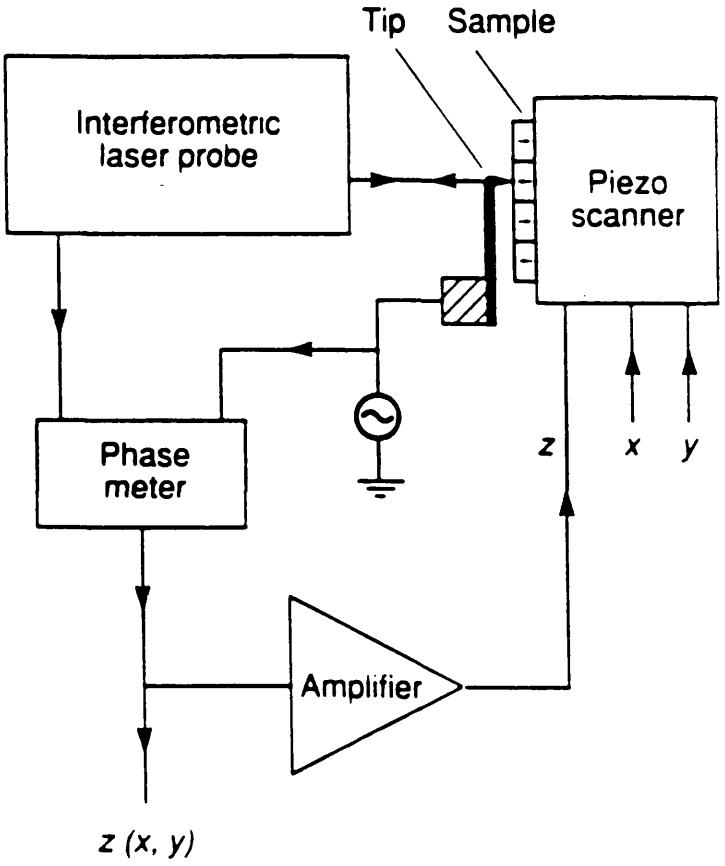

Figure 7.1 A schematic of the scanning force microscope used throughout this study.

coupled and an electrostatic force induces a vibration of several nanometres in the cantilever. Small forces present between the tip and object, result in a slight shift of the cantilever's resonance frequency ω_r. Cantilevers with high quality factor (Q=100-1000) are generally employed. By using such a cantilever, a small change in ω_r, results in a large variation of the phase α. The vibration is detected by interferometry and a phase meter used to detect α. A commercially available laser-diode, operating at a wavelength of 780nm (maximum output power 2mW) is used as the light source for the interferometer in this microscope. A polarising beam splitter splits the light into two orthogonal components; object and reference. Both beams pass through quarter-wave plates; the object being focused on the cantilever, while the reference is focused onto a mirror. The phase of the reflected reference beam can be changed by displacing the mirror with a piezo translator. Both beams return and mix at the beam splitter, with no light returning to the laser due to the quarter-wave plates.

Since the beams are now orthogonally polarised, a Wollaston prism is used to produce interference between them. This results in two spatially separated beams with intensities I_1 and I_2.

These intensities are given by:

$$I_{1,2} = (I_o + \Delta I_o)[1 + m^2 \pm 2m\cos(\phi)] \tag{7.3}$$

where, I_o is the average intensity, ΔI_o is the intensity noise term, m is the visibility of the interference pattern and ϕ is the phase difference between the object and reference beams. This phase difference is defined as:

$$\phi = \phi_o + 4\pi\left(\frac{\Delta z}{\lambda}\right)\cos(\omega_e t + \alpha) \tag{7.4}$$

where Δz is the amplitude.

By taking the difference between I_1 and I_2 the desired interference term is found. This difference is then amplified with a difference amplifier, whose output is given by:

$$U_o = A(I_o + \Delta I_o)m\cos(\phi) \qquad (7.5)$$

where A is a proportionality constant.

The phase of the vibrating cantilever is measured by a lock-in amplifier. The amplifier is used as the phase meter by setting the reference signal in quadrature with the input signal U_o.

The phase signal from the lock-in amplifier is used as an error signal to maintain a constant force gradient by changing the voltage across the z piezo (thus changing the tip-sample separation) of the xyz piezo-scanner on which the sample is mounted. This change in voltage is directly related to the magnetic microstructure of the sample under investigation.

All measurements made on the SMFM are controlled by a Hewlett-Packard 68000-based microcomputer system. The system is interfaced to the microscope through a VME bus. Two 12-bit digital to analogue converters (DAC) are used to control the x and y piezos of the scanner. The output voltages of the DACs are amplified (output in the range 0-1500V) and applied across the piezos. The x and y scan directions each have a range of 7μm in this instrument. A 12-bit analogue to digital converter (ADC) reads the output signal from the lock-in amplifier. The digitised values are then stored in a two-dimensional array. The contents of this array are then displayed on a monitor via a frame buffer.

A Pascal computer programme (den Boef 1991) operates the software for the microscope. It allows the size of the image stored in the array to be chosen (maximum of 256x256 pixels). The scanning direction can be either vertical or horizontal (the latter was always chosen during this study). During scanning a fast flyback mode was operated. In this mode, the object was moved slowly forward followed by a fast flyback where the tip is retracted. After the measurement has finished, the image may be stored on disc and limited image processing performed.

The SMFM is an extremely sensitive instrument and any external noise (acoustical, vibrational) will severely limit its performance by introducing unwanted motion of the tip with respect to the object. To insure against this, the

microscope is covered with a perspex hood and placed on a damped optical bench.

7.3 Tip fabrication

The fabrication of the cantilever and its tip is the most important feature of a force microscope. Its size, shape and the materials chosen should optimise the performance of the microscope. A cantilever intended to measure magnetic forces should have a weak tip lever, in order to reduce the topographic contrast which arises from weak van der Waals forces. However, it must also be stiff enough (have high resonant frequency) to eliminate any external noise or vibration. Finally the magnetic properties of the tip should be tailored to suit the object under investigation.

Most cantilevers are produced by electrochemically etching thin ferromagnetic foils or wires (eg Fe, Ni, Co). Reasonable tips with small radii of curvature (few 10s of nm) and high aspect ratio can be obtained with this method. However the tips used in conjunction with the microscope at Philips involved coating non-magnetic tips with a ferromagnetic thin film. The advantage of coated tips is the greatly reduced stray field. This can result in better resolution than that achieved with bulk tips. It is also of importance when imaging "softer" (low coercive) magnetic materials, since large stray field effects may alter the magnetic state of the material.

The cantilever was fabricated from a 1mm length of 10μm thick tungsten wire, with its end etched in 4% KOH solution to produce a fine tip with a radius of ≈60nm. The end of the cantilever was bent to 90° with a knife edge to produce a tip. To make the tip ferromagnetic, cobalt was galvanised onto the end as shown schematically in figure 7.2. This was done by lowering the tip into a cobalt solution which had a small DC current of 300nA sent through it via a resistor. The duration of the current was usually 1-3seconds. Finally to align the magnetic moment of the tip along its axis, it was placed in a magnetic field of 1 Tesla.

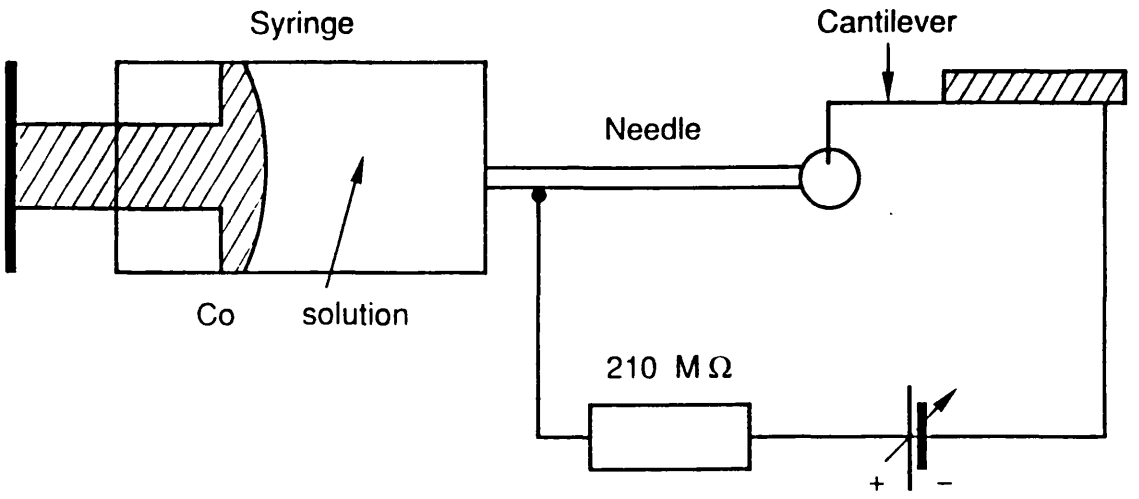

Figure 7.2 Schematic of galvanic deposition process for ferromagnetic tip fabrication.

The procedure of depositing the cobalt layer was crucial. The magnetic contrast observed in the final image depends on the dipole moment of the tip. Tips with large moments give better contrast, due to the larger forces involved, but yield poorer resolution because of greater tip volume. Therefore, depending on the specimen and the information required, the amount of cobalt deposited is controlled by adjusting the current and deposition time during galvanisation.

Scanning electron microscope (SEM) images of tips fabricated in the above manner, revealed that they were made up of many small crystallites (average size of ≈100nm). This helps to explain why the magnetic dipole moment was not always aligned with the tip axis; the crystals were randomly orientated, resulting in an unpredictable magnetic anisotropy. This suggests that additional optimisation of the galvanic deposition technique is necessary. Tips coated in this manner have yielded spatial resolution of ≈50nm.

A new approach to tip fabrication has been suggested by Grütter (1990) whereby batch fabricated silicon microcantilevers have been coated with thin magnetic films. This process eliminates the tedium of individually constructing each tip and should make SMFM an easier technique to implement.

7.4 Imaging Co/Pt multilayers with SMFM

To complement the study of Co/Pt multilayers by MDPC and other modes of Lorentz microscopy at the University of Glasgow, a project was undertaken during a three month placement at the Philips Research Laboratories to study Co/Pt multilayers by SMFM in their as-grown and ac-demagnetised states. An in-depth study (van Kesteren et al 1991) involving the study of thermomagnetically written marks in Co/Pt had already been undertaken at Philips. During this project, the films were demagnetised using the magnetic field produced by a VSM: the sample was spun between the poles while the magnitude of the field was slowly reduced. To make the SMFM measurements easier from a practical viewpoint, and to make better comparisons with the DPC images, all images were taken from multilayers that had been deposited on

Si_3N_4 TEM windows (as discussed in chapter 3).

The images of domain structures show the same irregular maze pattern that was observed when imaging with Lorentz microscopy. Now however, the domains show no preferred directionality and this is entirely due to there being no need to introduce a tilt to the sample, since the film surface and the tip should (ideally) be perpendicular to each other.

Figure 7.3 shows two typical SMFM images of natural domains in a film whose composition is 5x(0.35nm Co + 1.5nm Pt), deposited on a 1.5nm Pt seed layer. The upper image is of the film in its as-grown state, while the lower image was taken after the film had been ac-demagnetised. Each figure contains two images; the one on the left shows the grey level which is linearly related to the tip-object distance, while the one on the right shows the differentiated contrast, which can enhance small detail. The contrast generated in the images will be discussed in the next section. The horizontal and vertical scales are both 7μm. The spatial resolution of SMFM images is taken to be either the tip radius or tip-sample separation, whichever is the greatest. For the images displayed in this chapter a spatial resolution of ≈100nm can be estimated. The mean domain period, in the ac-demagnetised state, for this domain distribution was ≈1500nm, a value that is comparable with domain periods found in other very thin Co/Pt multilayers. Domain periods for other multilayers, that had greater numbers of bilayers in the stack were greatly reduced, having values in the range of 200-400nm. The increased contribution from the magnetostatic energy of these thicker films and their more sheared hysteresis loops account for the reduction in the domain period. These values of measured domain periods agree well with the measurements taken from Lorentz microscopy (Donnet et al 1992).

7.5 Contrast mechanism and interpretation of SMFM images

The task of quantitatively understanding the contrast generated from high resolution SMFM images is non-trivial. This is because a SMFM responds to magnetic forces (magnetostatic in origin), therefore it does not give a direct

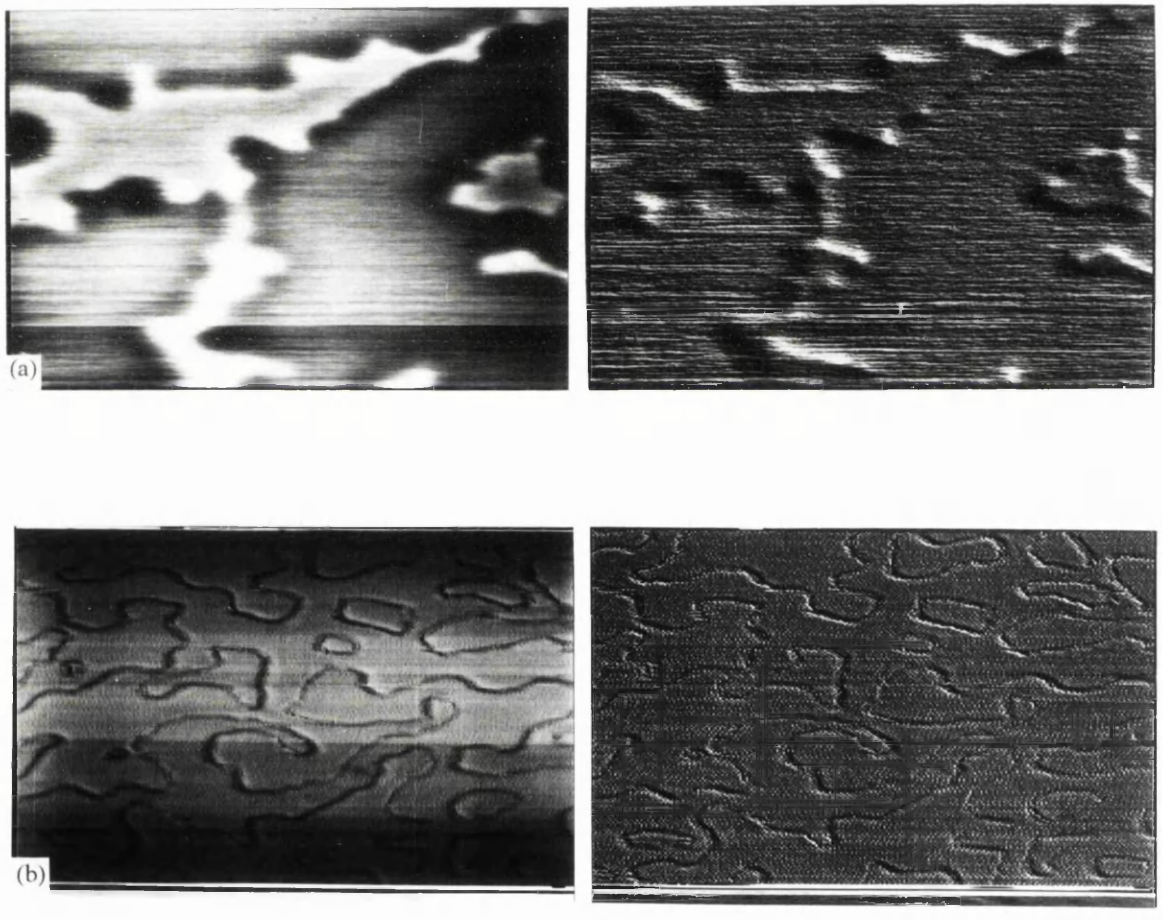

Figure 7.3 (a) and (b) Scanning force microscopy images of the domain structure within a Co/Pt multilayer. In each image the area scanned is $7x7\mu m^2$.

measure of the magnetisation of the sample. However, when combined with information from other magnetic domain imaging techniques (Lorentz and Kerr microscopy, SEMPA) a fuller description of the magnetisation may be obtained. Simple models exist which can qualitatively describe the contrast observed (Hartmann 1988). In many cases this is very useful in itself. In general, an image is thought of as a map of tip height as a function of position over the specimen for a constant force gradient. In the simplest interpretation, it is assumed that a point dipole tip follows contours of force gradient determined by stray field from the sample. Both the tip and object are assumed to be magnetically "hard" (ie have high coercivity) in this model and thus neither can influence or modify the other's magnetisation. This is adequate for studying magnetic recording media, but breaks down when soft magnetic materials are investigated. Also, the tip magnetisation is assumed to be uniform along its axis, but for galvanised tips, it has been observed that the tip is made up of crystallites resulting in an unpredictable anisotropy.

According to theory, contrast in SMFM images should only be seen where there is a high density of magnetic charge at the surface. This would allow domain walls to be delineated, since the field gradient peaks sharply in the vicinity of a domain wall, while contrast is left constant within the domain interior. However from figure 7.3 it is clear that in practical circumstances this is not always the case. Far away from any domain walls, the tip should only sense the electrostatic force gradient. It is expected that lines of constant electrostatic force gradient run parallel to the object, resulting in equal tip-object spacing for both magnetisations. In (a) however, it is observed that the spacing is significantly different for the two possible directions of magnetisation. Schönenburger et al (1990) relate this phenomenon to the domain length of the tip. The predicted contrast from theory occurs when the tip may be considered as a point-dipole, as suggested above. This is approximately the case when the domain length of the tip is much smaller than the domains being imaged. Such an image is shown in (b) where the only contrast observed is at domain walls.

The simple model given above is adequate to explain qualitatively the

contrast observed in SMFM images to a resolution of ≥100nm. More thorough investigation of the tip and its relationship with the sample is required if smaller detail is to be quantitatively understood.

At all times care must be taken to ensure that surface topology is not also interpreted as magnetic contrast. When an object is scanned below the tip, the force gradient K will alter due to both topographic and magnetic stray field variations. Various methods for separating the two components have been suggested. By increasing the tip-object separation then the tip responds only to the longer range magnetic forces. den Boef (1991) decided on another system. The total force gradient measured in the SMFM consists of an electrostatic f(z) and magnetostatic term f(m). Only in the vicinity of a domain wall does f(m) have an substantial value. By making the bias applied between the tip and object small, both topographic and magnetic features are displayed in the image. However if the bias is increased, the relative contribution to the force gradient from f(m) is greatly diminished and it is now only possible to image topography. From the two images it is then possible to correlate the magnetic structure with any structural ones.

7.6 Comparison of DPC and SMFM domain imaging modes

Following domain studies with both electron optical and force microscopy techniques, it is now useful to compare the relative advantages and disadvantages of each method. It should be noted that the discussion below is limited to the microscopes actually used through this work.

Figure 7.4(a) shows two in-plane induction maps from DPC images of a multilayer whose composition is: 14x(0.35nm Co + 1.09nm Pt), while figure 7.4(b) shows SMFM images of the same film. In (a), the lower magnification image reveals a large region of the domain pattern, while the high magnification image centres on a small area of a single domain wall. The spatial resolution of the image was ≈20nm. This compared favourably with the 100nm resolution found in (b). The quality of the DPC images is also greater than that of the

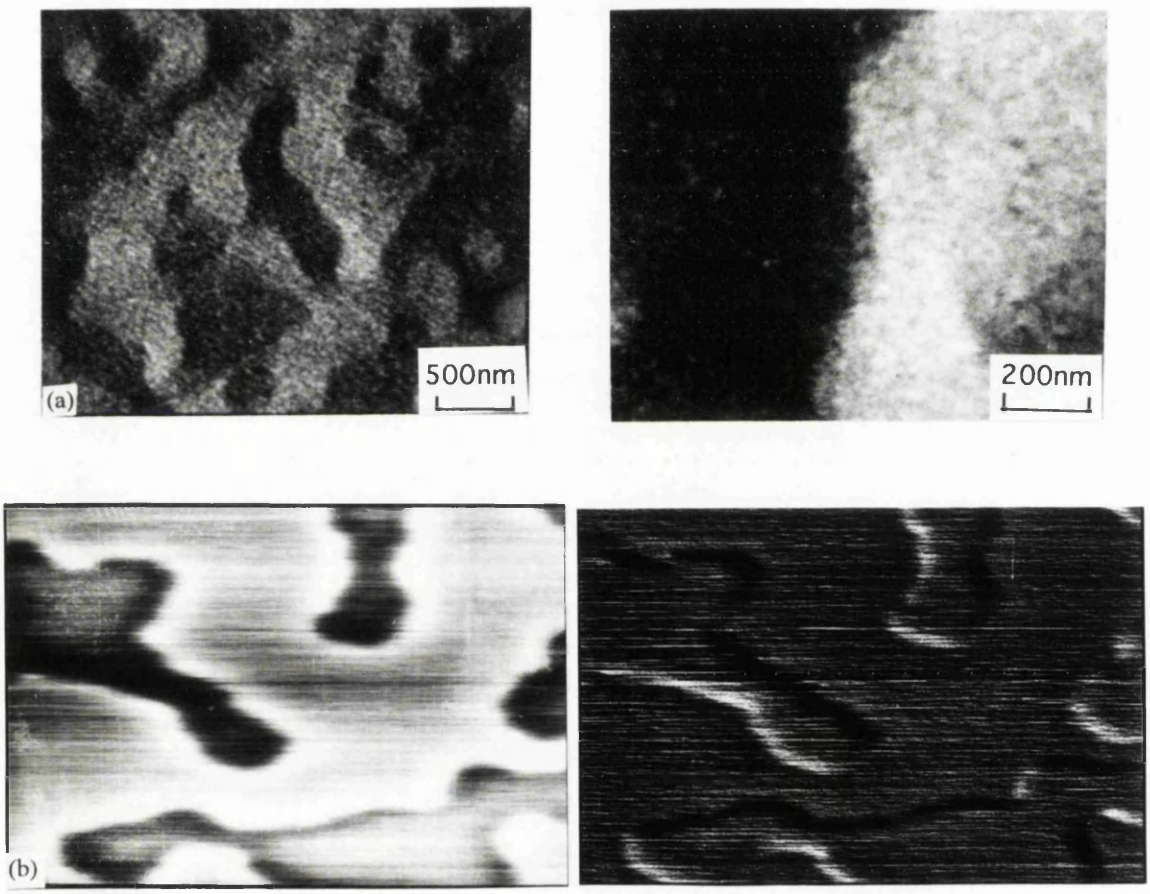

Figure 7.4 **(a)** Low and high magnfication DPC images (a) of a Co/Pt multilayer with composition of 15x(0.35nm Co +0.9nm Pt).

(b) SMFM images of the same multilayer.
The area scanned was 7x7μm

SMFM images due to an averaging over four frames to reduce noise. Scan lines are clearly visible on the SMFM image.

In the electron microscope, when dealing with perpendicularly magnetised materials (such as MO media), a tilt must be introduced to provide a significant component of induction orthogonal to the electron beam. This results in a small distortion of the domain pattern, as seen in (a). The directionality is wholly dependent on the tilt axis chosen, as was shown in chapter 3. No such tilt was required when imaging with SMFM, thus a more faithful representation of the domain structure was obtained in a single image. It should be noted however, that an unwanted directionality may be introduced if the tip (or its magnetic moment) were not aligned perpendicular to the sample surface.

The main advantage of SMFM over DPC and other electron optical imaging modes was that no special or sensitive specimen preparation is required and no vacuum environment is deemed necessary. For STEM analysis, the specimen must be transparent to electrons; thus specimen thicknesses must be less than 100nm (for 100kV electrons). This means that samples of technological importance must often be separated from their seed layers and substrates (which can have a great bearing on their microstructure) and in the case of very thick specimens, some thinning may be required. Throughout this study, the DPC investigations were carried out on multilayers which had been deposited on specially prepared Si_3N_4 windows to allow electron transmission. As this is not necessary when imaging with SMFM, experiments may be carried out on real discs, allowing actual recording characteristics to be related to the magnetic contrast observed from the images. This advantage was exploited by van Kesteren et al (1991) in their study of written marks in Co/Pt multilayers. It will be of great importance in helping to optimise future disc production.

A second disadvantage (after poorer resolution) found when imaging with this force microscope was the time required to form an image. A 256x256 pixel image took ≈40 minutes to construct. A comparable DPC image (single frame), may be produced with an acquisition time of ≈12s.

The greatest disadvantage of using SMFM to image magnetic domains was

that it was not very reproducible. In contrast, DPC microscopy can achieve very reproducible results, if a camera length which gives good magnetic contrast has been chosen. The difficulties arose in SMFM mainly because of tip fabrication. It was extremely difficult to deposit an equal amount of cobalt onto each tip and therefore the dipole moment and shape of each ferromagnetic tip can differ. To overcome such a problem, Grütter et al (1990) proposed a method for batch fabrication of sensors for use in force microscopy. These sensors can be matched to a particular sample through a choice of different magnetic coatings. Tip crashes also hinder the technique of SMFM. Some or all of the ferromagnetic coating may be lost during such a crash and although it was easy to deposit more onto the tip, the contrast will be altered due to the different quantity of cobalt.

An important advantage of modified DPC microscopy is the ability to substantially separate contrast arising from magnetic and non-magnetic sources. This allows finer magnetic detail to be observed than was previously possible. It is a problem when imaging with SMFM to overcome the influence of surface topology.

Finally, as was explained in chapter 2, the DPC mode of Lorentz microscopy is a linear imaging technique and the contrast in the final image is well understood. This allows quantitative analysis (as in chapter 5) to be undertaken, which could not be performed on SMFM images.

7.7 Summary

This chapter has shown that force microscopy is a powerful technique for imaging magnetic domains. Spatial resolution of the order of 100nm is routinely achieved and 10-25nm is possible with considerable effort. This does not compare favourably with DPC imaging, although a breakthrough in tip technology would allow for much greater spatial resolution. The main advantage of this imaging mode is in the study of recording materials. The domain structures within real discs may be investigated without the need for any special

specimen preparation. Although it is difficult to obtain quantitative results from SMFM, its use complements other magnetic domain imaging techniques and contributes to obtaining a full description of the magnetisation of the film under investigation.

Chapter 8

A Domain and compositional study of MnZn-ferrites

8.1 Introduction

This chapter moves away from the work concerning Co/Pt multilayers for MO recording purposes and deals with the analytical studies that were performed on polycrystalline soft MnZn-ferrites, which had been suitably thinned for use in the electron microscope. Soft MnZn-ferrites are most commonly used in high frequency (up to 10MHz) commercial applications (Pannaparayil et al 1991). Specialised applications include read/write heads for high speed magnetic recording and high frequency telecommunications applications. The composition of the ferrites studied throughout this chapter was $Mn_{0.60}Zn_{0.35}Fe_{2.05}O_4$. The method of preparation of these films differed from the conventional ceramic processing techniques. Wet chemical methods were used in the powder preparation and consolidation (Noordermeer and Severin-Vantilt 1988). By adjusting the sinter temperature between 750 and 1250°C, MnZn-ferrites of constant composition but with different grain sizes (in the range 0.2-16μm) could be produced.

Two different electron microscopy studies were undertaken. The domain structures within two films which had the same composition, but different grain sizes were examined by Lorentz microscopy to ascertain whether the grains were mono-domain. From analysis of characteristic energy dispersive x-ray spectra (EDX analysis) from one film, compositional profiles (specifically the variation of Zn/Fe and Mn/Fe) were determined in the vicinity of grain boundaries within the film.

8.2 Domain structures in MnZn-ferrites

8.2.1 Introduction

The domain structures of these ferrites had previously been studied, in bulk samples, by neutron depolarisation (ND) (van der Zaag et al 1991) in order to determine the relationship between the grain size and their domain size. In the study reported upon here, the domain structures of the same samples were studied, albeit in thin films using all three modes of Lorentz microscopy (Foucault, Fresnel and MDPC) to directly observe the roles played by the grains and their boundaries in determining the domain structure. Two samples were studied which had grain sizes of 1.9 and 0.2μm (measured from SEM images). For use in electron microscopy the ferrite samples were lapped and polished to about 10μm thick. Subsequently the specimen was thinned down to 100keV electron transparency by Ar^+ ion-milling to ≈50nm. To facilitate handling, these samples were then mounted on phosphor bronze rings with an inside diameter of 2mm. Before imaging took place the films were ac-demagnetised. As throughout this thesis, the two CTEM modes of Lorentz microscopy were employed initially, followed by more detailed investigations using DPC.

8.2.2 Results

Figures 8.1 and 8.2 show standard bright field, Foucault and Fresnel images of two areas in the larger grained ferrite. From the images, it was clear that the domains appeared across the whole area of the thinned specimen. There were many distinct domain wall boundaries, but also many others which were not so well defined. This suggests a slowly varying direction of magnetisation. In some cases, there was significant change in direction of the magnetisation at grain boundaries (indicated on the figures), suggesting that they also act as domain boundaries. However, this was not universally true; domain walls could be observed inside the grains in the Fresnel images (top right image) and in some places they actually cross grain boundaries. MDPC imaging allowed the domain

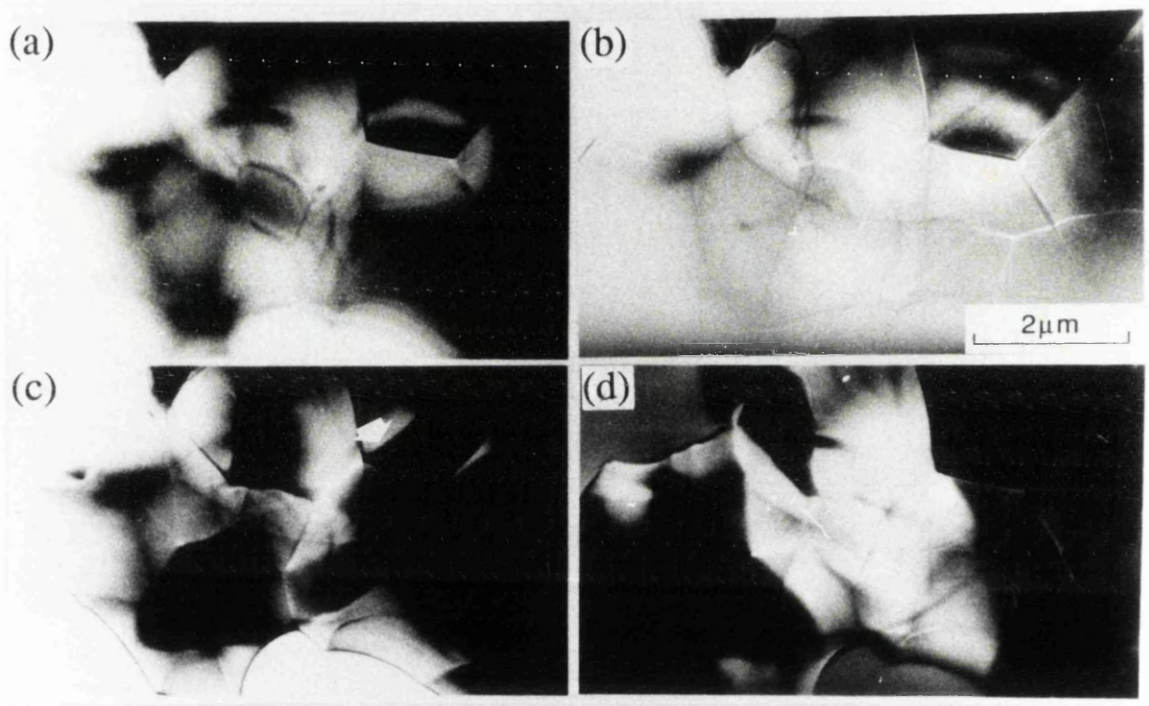

Figure 8.1 A BF (a), Fresnel (b) and two Foucault (c) and (d) images of a region of the larger grained ferrite.

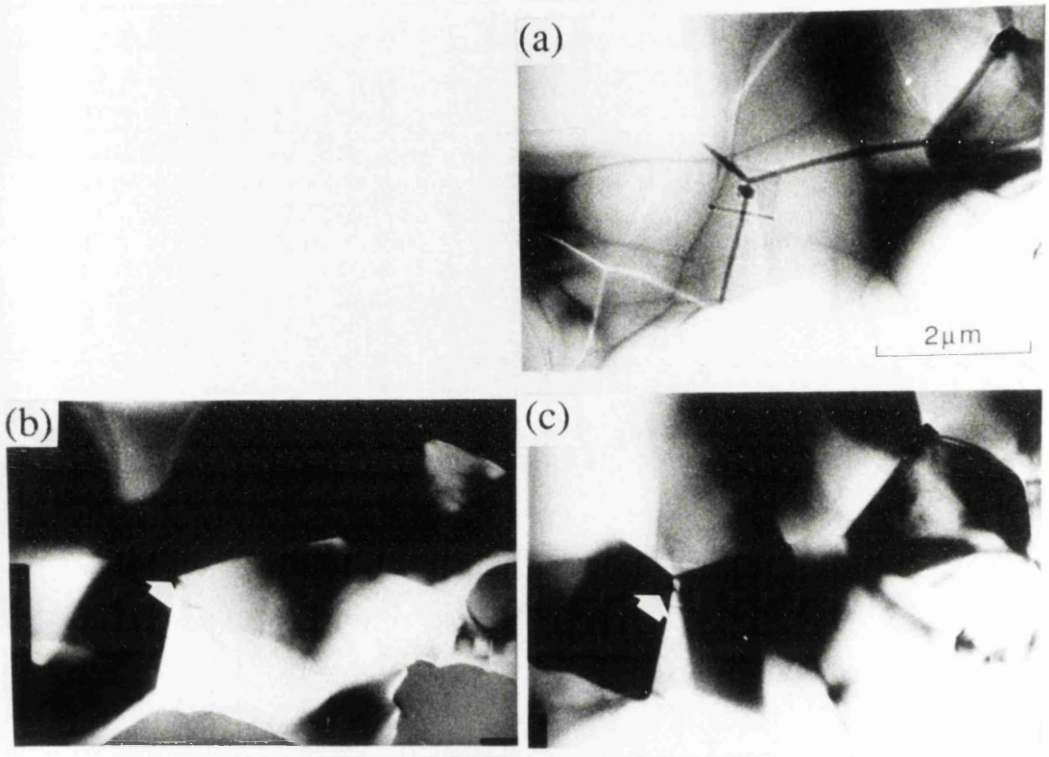

Figure 8.2 A Fresnel (a) and Foucault (b) and (c) images of a second region in the larger grained ferrite.

structures to be examined with greater resolution. The imaging conditions used on the HB5 STEM are given below. The probe was formed by exciting C1 together with a 25μm SAA. A 500μm VOA was used as a spray aperture. The best magnetic contrast was achieved with the following PSL settings: P1:+8, P2: off, P3: +8, which resulted in a smaller camera length than used when imaging the multilayers in the previous chapters. This was because the scale of the crystallites in the ferrites were of the same order as the domain structure. The MDPC images (figures 8.3, 8.4) show magnetic images mapping induction in two orthogonal directions together with a bright field image. These confirmed the findings that close to the edge of the hole the grains were not mono-domain. Thus in general ferrites with a grain size of the order of a few microns were not mono-domain in such thin foils.

Lorentz imaging of the smaller grained ferrite proved more difficult because the separation of magnetic from crystallographic contrast could not always be achieved unambiguously. This fact made the observations of domains, with MDPC in particular, extremely hard. However, the Foucault images (d and e in figure 8.5) of this film suggest that there was a coarse magnetic structure significantly larger than the grain size; nevertheless, despite this, fine magnetic detail was also discernible within the grains themselves as marked on the Fresnel images (b and c). Thus in this case also, there were grains which certainly appeared multi-domain.

The above results would seem to be in contradiction with those attained from neutron depolarisation experiments which found that grains with sizes in the region 0.2-4μm were mono-domain for these ferrites. The Lorentz microscopy of these films showed that in general these grains were multi-domain, although in many instances the grain boundaries did also act as domain walls. A possible explanation for the discrepancies found between the results of the two techniques could be the extra specimen preparation (thinning) required for the bulk samples to be of use in electron microscopy.

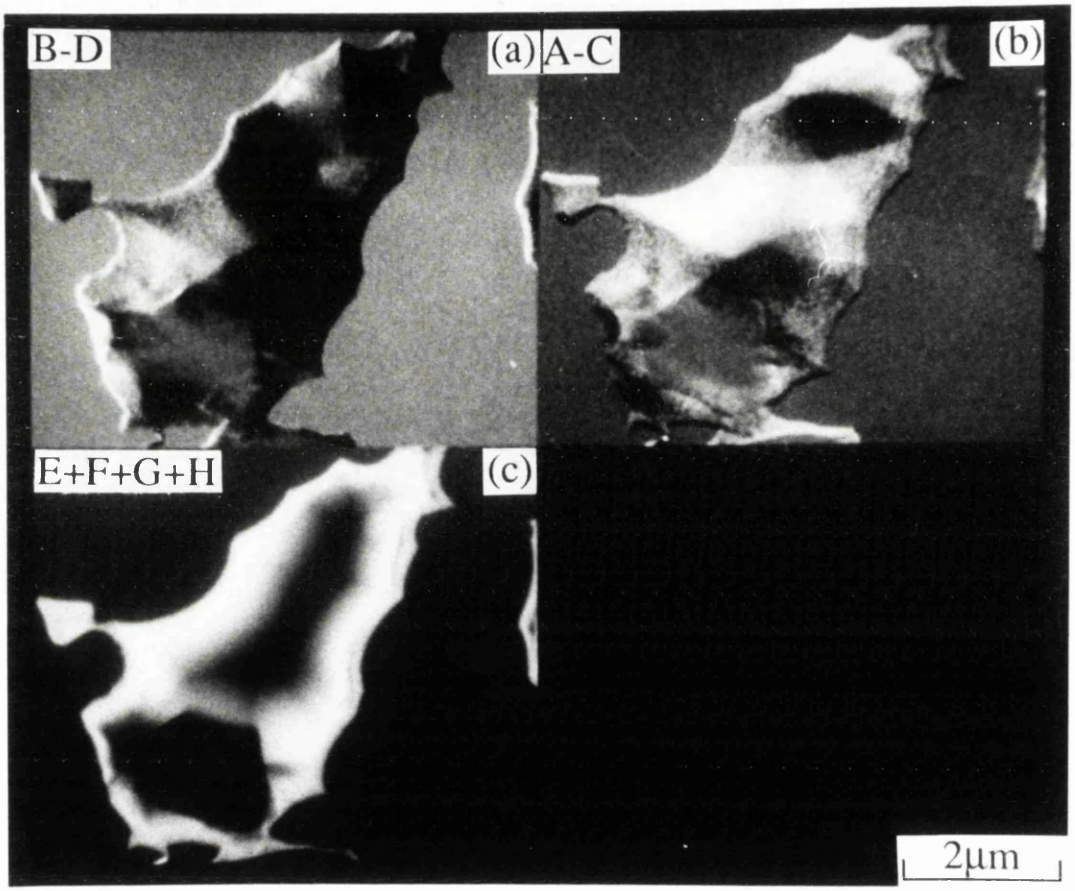

Figure 8.3 MDPC images of a region in the larger grained ferrite.

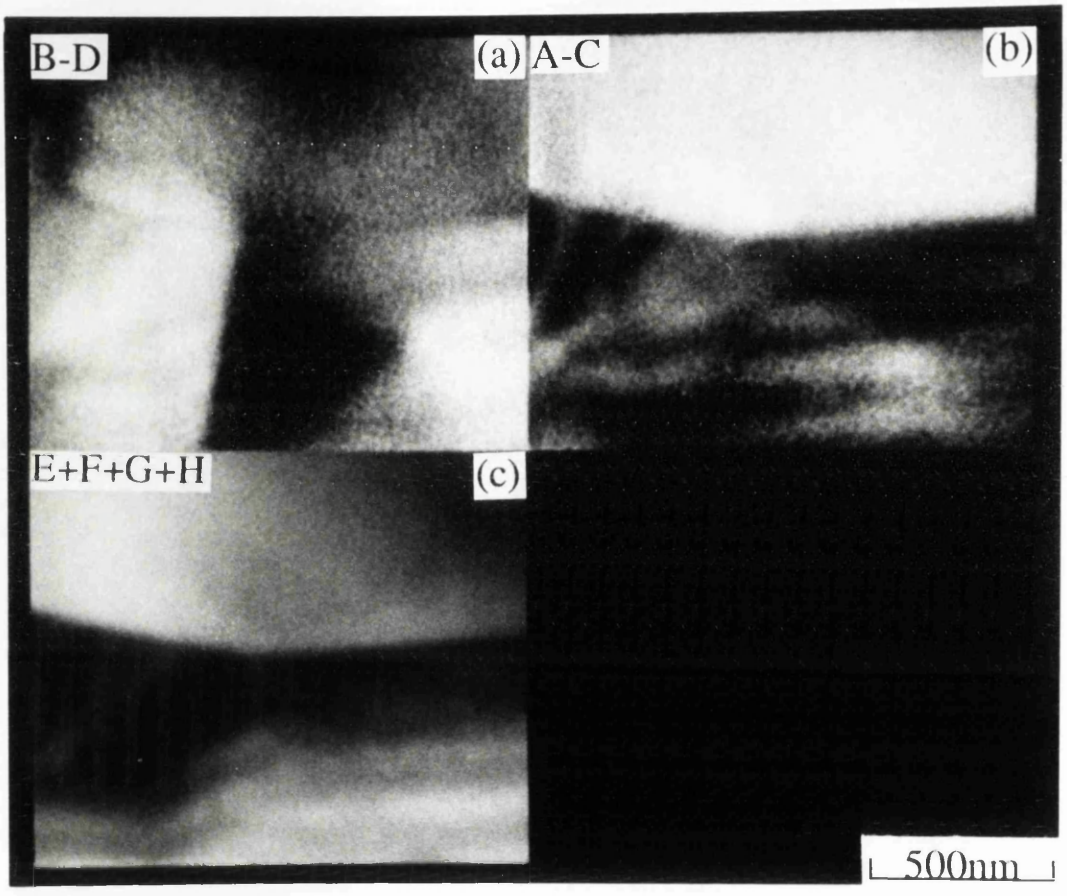

Figure 8.4 MDPC images of a second region in the larger grained ferrite.

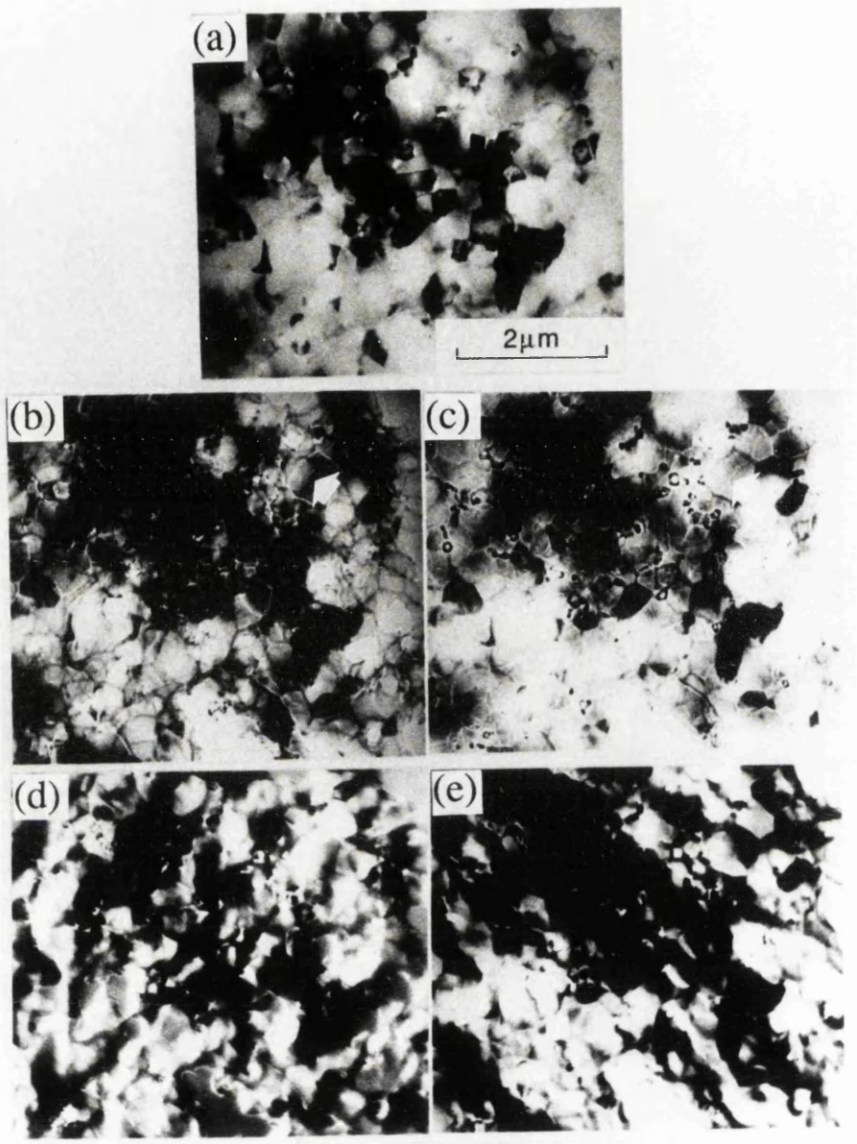

Figure 8.5 A BF (a), two Fresnel (b), (c) and two Foucault (d) and (e) images of a region in the smaller grained ferrite.

8.3 Composition profiles across grain boundaries

Grain boundaries play an important role in determining the properties of soft ferrites (Franken and van Doveren 1978). The actual grain growth during the sintering process depends on the quality of the grain boundary and impurities (Na is the main impurity in these films) in the boundary can inhibit or encourage grain growth. As explained in the introduction to this chapter, we were interested in determining whether any local accumulation of Mn or Zn occurred in the neighbourhood of a grain boundary. This could result in a regions of lower permeability which in the extreme case could lead to a non-magnetic grain boundary. Johnson and Visser (1990) and Visser and Johnson (1991) postulated a non-magnetic grain boundary model to account for the behaviour of the permeability in these ferrites. This study was carried out by analysing characteristic x-ray spectra, taken from a thinned (≈50nm) area of the film with grain size of 0.2μm.

8.3.1 X-ray production in the STEM

X-rays can be produced by two different mechanisms in thin films when excited by electrons with energies of around 100keV. Bremsstrahlung photons are produced when the incident electrons are accelerated in the field of an atomic nucleus in the specimen. They can lose any amount of energy up to their kinetic energy and this gives rise to a continuous background in the spectrum which decreases in magnitude with increasing photon energy. As it is similar for all elements, it is not characteristic of a particular atom and cannot yield any direct information on elemental concentrations in the film. Characteristic x-ray photons are produced when an atom de-excites following the ionisation of an inner shell by an incident electron. The emitted photon of energy hν is characteristic of the atom and so a peak appears in the spectrum centred about this energy. It is these photons which provide the information on elemental concentrations. The analysis in this chapter is only concerned with the electron transitions to the inner K-shell. A K_α x-ray is radiated when the inner shell electron is replaced

by one from the L-shell and a K_β x-ray is radiated if the replacement electron comes from the M-shell.

Thus a typical EDX spectrum (figure 8.6) consists of Bremsstrahlung of all wavelengths down to a minimum corresponding to the incident electron energy together with characteristic x-ray peaks whose wavelength depends on the nature of the specimen.

8.3.2 EDX microanalysis

High spatial resolution energy dispersive x-ray (EDX) microanalysis is an appropriate analytical technique to determine the local elemental composition of thin film specimens (Cliff and Lorimer 1972). The technique is based on detecting and quantifying characteristic x-rays produced when a volume of the specimen is irradiated by a focused electron probe which is held stationary with respect to the specimen. The x-ray photons emitted from the film enter a semiconductor detector which is situated close to the specimen in the microscope and produce photoelectrons which ionise the detector atoms. These then in turn de-excite and generate electron-hole pairs. Since the energy for each of these excitations is small, the number of pairs is directly proportional to the energy of the original photon. A voltage applied across the detector separates the electrons and the holes and a current pulse is generated, whose magnitude is proportional to the incident photon energy. The current pulse is measured and the channel of a multi-channel analyser corresponding to this photon energy is incremented. The accumulation of these pulses across the whole energy range produces an x-ray spectrum from which it is possible to quantify local concentrations in the specimen.

8.3.3 Experimental considerations

The work was carried out using the extended VG HB5 STEM at the University of Glasgow. To ensure that the specimen was in thermal equilibrium with the microscope interior and thus reduce specimen drift to a minimum it was loaded in a double tilt Be cartridge around 16 hours before data acquisition began. In

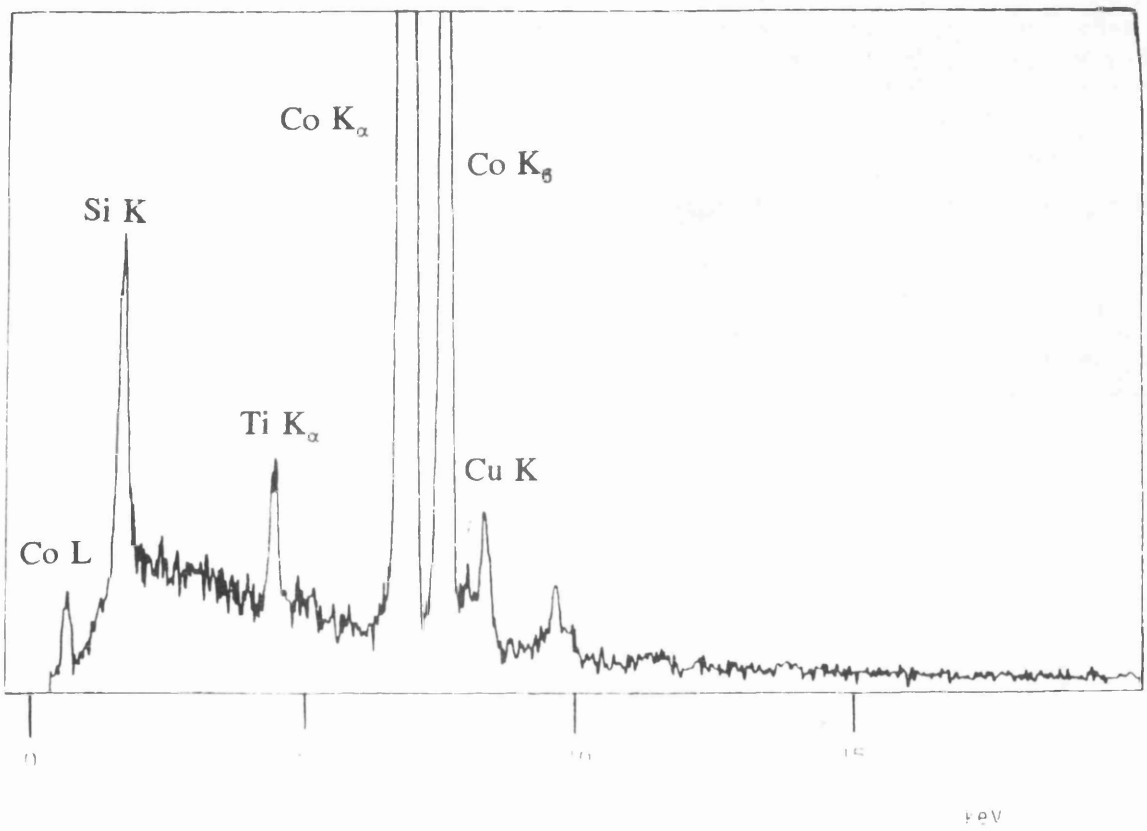

Figure 8.6 A typical x-ray spectrum from a Co sample showing both the Bremsstrahlung and the characteristic x-ray peaks.

order to carry out analytical microanalysis with high spatial resolution on a small area of specimen, a very small probe is required. To provide this, the microscope was operated with both C1 and the objective lens excited and a 100μm virtual objective aperture (VOA) was used as the probe defining aperture. Undesirable artifacts from the x-ray spectra were eliminated by using a VOA instead of a real objective aperture. This mode produces a probe with a ≈1.5nm diameter (McGibbon et al 1989) with sufficiently high energy to produce characteristic x-rays.

The x-ray detector used in this project was a Link Analytical lithium drifted silicon crystal located at an angle of 100° with respect to the electron beam direction. The crystal is held between gold electrodes with a potential difference of 500V. A protective beryllium window (≈8μm thick) is situated between the crystal and the microscope column. The specimen was tilted towards the detector (x and y tilts of -20° and +20°) so that absorption of x-rays from the specimen was minimised.

Areas with suitably orientated grain boundaries (with respect to the electron beam) for EDX analysis were selected using annular dark field (ADF) images. In such digital images, acquired as prescribed in chapter 3, the boundaries are more clearly defined thus making the positioning of the electron probe easier. The experimental procedure entailed the acquisition of a series of x-ray spectra from thin regions (≈50nm) close to the edge of the hole in the thinned specimen that had well defined, suitably orientated boundaries. In this study, beam-induced contamination was not a severe problem because each area was "flooded" (Rogers 1990) with electrons prior to the microanalysis, thus immobilising any local supply of contaminant.

Acquisition and analysis of the spectra were carried out using a Link Analytical eXL acquisition system. The software available with the eXL allowed the number of characteristic x-rays from each element of interest to be determined by defining windows over appropriate peaks and background regions in their vicinity. This is all the information that was required if variations in composition are sought as the number of x-ray photons emitted are directly

proportional to the number of atoms of that element irradiated. Thus errors in the compositional profiles come from x-ray statistics and the uncertainty with which the probe is positioned with respect to the boundary.

For each region, a spectrum was recorded from an area of 10000nm^2 to obtain a "global" concentration of each element in that particular area. The probe was then positioned centrally on a boundary (with 0.5nm accuracy) and a spectrum recorded. These spectra were acquired for 60s, during which time no discernable specimen drift was observed. The area scans were recorded for longer periods of time so that their contribution to the final error was usually insignificant. If depletion of Zn was observed at the boundary, the probe was moved with increments of 1, 2, 4, 10 and 20nm into the grains on either side of the boundary in question and a spectrum recorded at each position (again recorded for 60s). Figures 8.7, 8.8 and 8.9 are dark field images of regions of the grains in the MnZn-ferrite investigated and indicated on them are the areas where the microanalysis was undertaken.

8.3.4 Analysis of x-ray spectra

A typical spectrum obtained from a small region of a MnZn-ferrite with a grain size of 0.22μm is presented in figure 8.10. The first stage of analysis involved removing the unhelpful contribution of Bremsstrahlung in the vicinity of the characteristic peaks. For the spectra here the background was small and a linear interpolation technique was satisfactory. This yielded direct values for the counts in the Mn K_α and Cu K_α peaks. The copper contribution arose from the holder onto which the ferrite was fixed and was greatly diminished by the insertion of a selected area aperture (SAA) in the microscope to act as a spray aperture. However it was clear that the Mn K_β peak overlaps with the Fe K_α peak thus making a non-negligible contribution to the number of counts in that peak. This contribution made to the total counts in this peak by Mn was calculated by multiplying the number of counts in the Mn K_α peak by 1-p derived from the relevant partition function (Gray 1981), which is defined as:

Figure 8.7 ADF image of a region in the smaller grained ferrite, indicated are the area where EDX microanalysis took place.

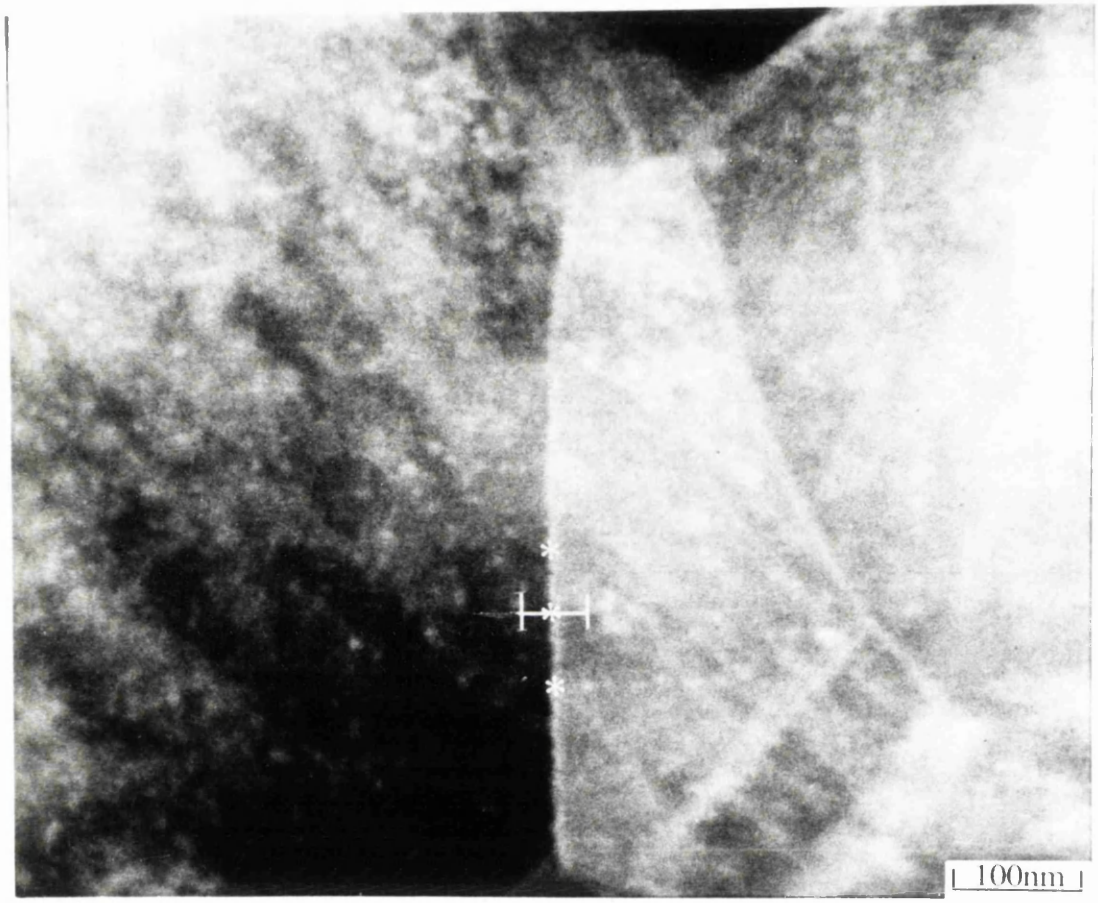

Figure 8.8 ADF image of a second region in the smaller grained ferrite. Indicated are the areas where EDX microanalysis took place.

Figure 8.9 ADF image of a third region in the smaller grained ferrite. Indicated are the areas where EDX microanalysis took place.

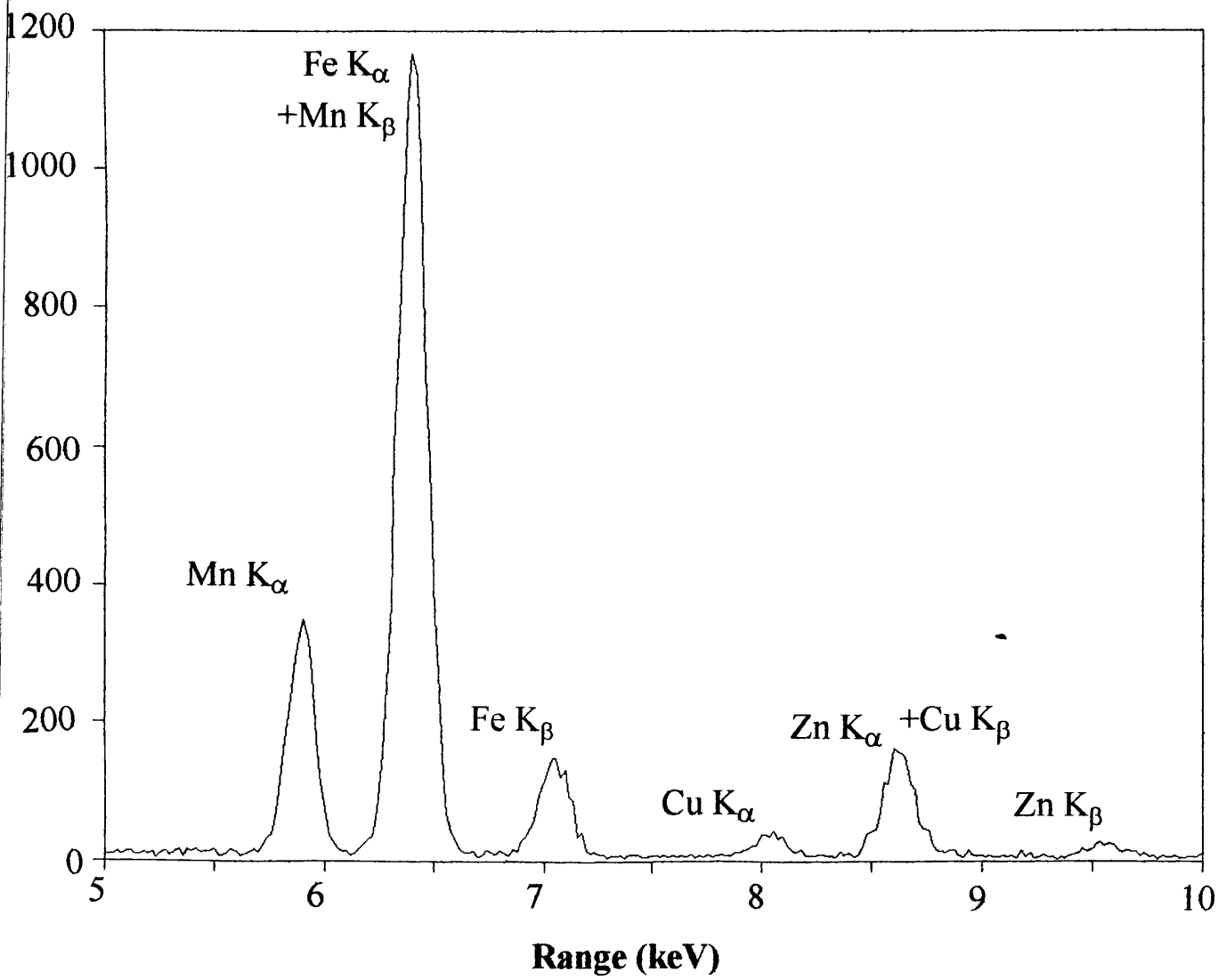

Figure 8.10 A typical x-ray spectrum taken from a ferrite with composition of $Mn_{0.60}Zn_{0.35}Fe_{2.05}O_4$ and showing the peaks of interest.

$$p = \frac{K_\alpha}{K_\alpha + K_\beta} \tag{8.1}$$

The number of Mn K_β counts so determined was subtracted from the peak containing Fe K_α. A similar procedure was used to remove the Cu K_β contribution from the peak containing the Zn K_α peak.

To turn the recorded x-ray counts in the corrected K_α peaks into absolute atomic compositions a knowledge of the relative efficiencies of x-ray generation and detection of the elements of interest was required. The characteristic photons of interest here were detected with similar efficiencies, but there was a difference in their generation efficiencies. A k-factor relates the number of atoms of each element in the excited volume (n) to the measured number of characteristic x-rays corresponding to that element (N) through:

$$\frac{n_A}{n_B} = k_{AB}\frac{N_A}{N_B} \tag{8.2}$$

This factor is given by:

$$k_{AB} = \frac{\omega_B p_B \sigma_B \varepsilon_B}{\omega_A p_A \sigma_A \varepsilon_A} = k_{BA}^{-1} \tag{8.3}$$

where ω is the fluorescence yield (probability of emission of a characteristic x-ray rather than an Auger electron), p is the partition function, σ is the ionisation cross-section with 100keV incident electrons and ε is the efficiency of the detector. For the elements under consideration only two k-factors were required. These were k_{ZnFe} and k_{MnFe} and insertion of the correct values (Bearden 1967) (given in table 8.1) yields a figure of 1.09 for k_{ZnFe} and 1.00 for k_{MnFe}.

8.3.5 Results

The overall boundary depletion of Zn(Mn) was calculated as:

	Fe	Mn	Zn
σ (m^2)	7.12×10^{-46}	7.99×10^{-46}	4.6×10^{-46}
ω	0.339	0.302	0.48
ε	≈ 1	≈ 1	≈ 1
p	0.139	0.139	0.142

Table 8.1 Values of constants required to calculate the necessary k-factors.

$$\%Zn(Mn)dep = 100 * \left[\frac{Zn(Mn)_{grain} - Zn(Mn)_{boundary}}{Zn(Mn)_{grain}} \right] \qquad (8.4)$$

The results from these calculations for six examinations are shown in table 8.2 and figure 8.11(a) and (b) compares two x-ray spectra taken from the boundary and a grain interior. For zinc, substantial depletion at the boundary was observed in most instances, with the mean value being 16.5%; for manganese no evidence of depletion within the accuracy that we can determine compositions was observed. The errors were almost entirely due to the statistical uncertainties in the counts in the characteristic peaks.

In order to gain a measure of the spatial extent of the Zn depletion in the vicinity of the boundaries, a series of spectra as detailed above were recorded across 4 boundaries (denoted 1,2,5 and 6 in table 8.2). The quantity of interest was basically the ratio r of Zn to Fe. However for ease of comparison between the four areas a parameter P(x) was introduced which is a normalised version of r which runs between 1 (at the boundary centre) and 0 (characteristic of the overall grain composition). P(x) is given by:

$$P(x) = \frac{r_g - r(x)}{r_g - r(0)} \qquad (8.5)$$

where r_g is the global ratio of Zn/Fe, r(x) is the ratio at a position x from the boundary centre and r(0) is the ratio at the centre of the boundary. Thus 1-P provided the desired compositional profile of Zn depletion. It should be noted that for each plot, the results from comparable distances on either side of the boundary were averaged to provide better statistics. This seems valid since there was nothing to suggest, from the recorded x-ray spectra, that the composition in any one grain was different from that of its neighbour.

The profiles for the four individual regions are shown in figure 8.12. Although there was a fair spread in the actual values at each position from the boundary, the trend was similar in all plots. To get better statistics it was therefore assumed that the compositional profile was the same in each case and produced

Area	Zn depletion (%)	error	Mn depletion (%)	error
1	27.0	4.6	3.4	2.1
2	19.4	3.7	-3.8	1.1
3	6.5	4.3	-1.6	2.9
4	10.8	7.2	-4.8	2.5
5	19.0	3.7	2.4	1.8
6	16.4	3.1	-0.5	1.7

Mean Zn depletion = 16.5%

Standard deviation = 6.5%

Standard error = 2.7%

Mean Mn Depletion = -0.8%

Standard deviation = 3.0%

Standard error = 1.2%

Table 8.2 Results of Zn and Mn depletion at all areas investigated.

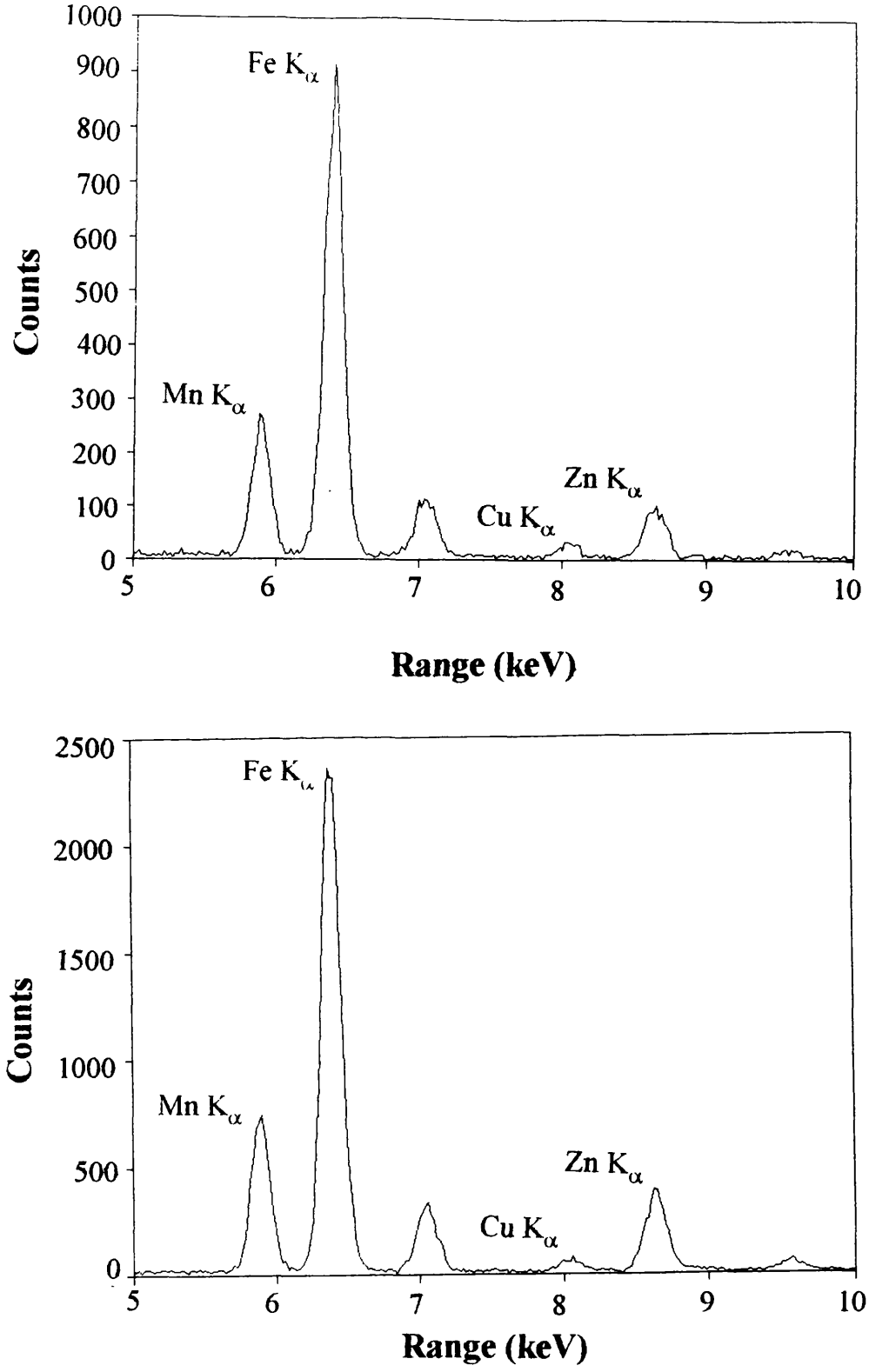

Figure 8.11 Two x-ray spectra taken from a boundary (top) and a grain of one area that was investigated.

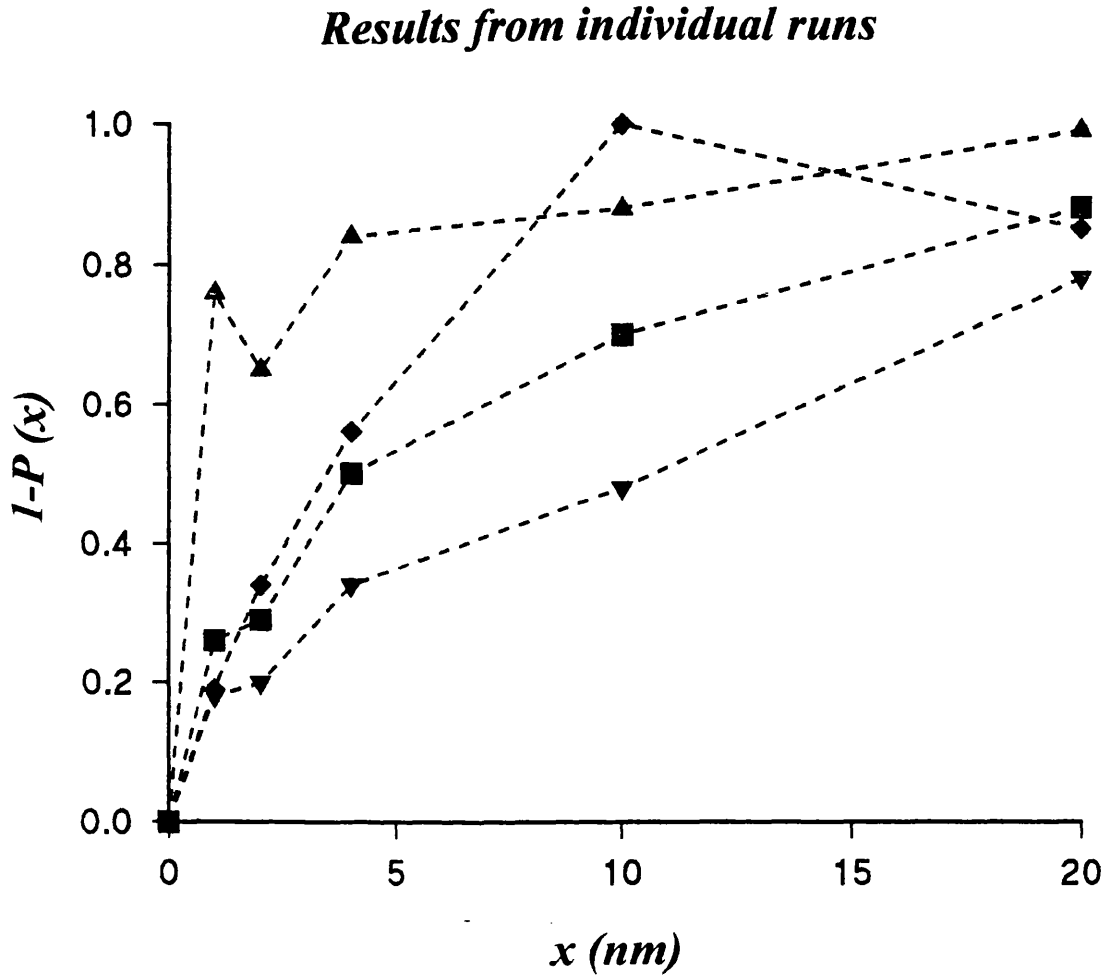

Figure 8.12 Compositional profiles from the individual areas.

a "mean value" plot, which is presented in figure 8.13. From this, a suitably defined boundary "width" can be obtained. Many things can degrade the spatial resolution of the analysis: beam spreading due to large angle (elastic) scattering in the finite thickness of the specimen (roughly proportional to $t^{3/2}$) (Goldstein et al 1977), the finite size of the probe and errors in its positioning and misorientation of the boundary itself. From the results presented here, it can be concluded that the regions where Zn depletion occurs are contained within the upper limits of the composition profile.

8.3.6 Discussion

From the results of the previous section it appeared that significant Zn depletion occurred at the grain boundaries with respect to the bulk composition. A similar depletion of Zn was previously found by Sundahl et al (1981). They also found that such a depletion lead to a decrease in the initial permeability of the ferrite. Therefore the Zn depletion found here could induce a region of low permeability. This would be in accordance with model of Visser and Johnson (1991) which proposed that the bulk ferrites consisted of grains of diameter D surrounded by a non-magnetic (or low permeability) grain boundary of thickness δ. The domain structures observed in section 8.2 would seem to contradict this evidence; calculations performed using the model predict a δ of 1.5nm for the ferrite analysed here. This result was well within the extent of Zn depletion observed from the composition profile.

8.4 Summary

The domain studies of two thin foils of soft MnZn-ferrites with different grain sizes (0.2 and 1.9μm) revealed that, in general a multi-domain structure was present, although in many instances for the larger grained ferrite grain boundaries did act as domain walls. These results differed from ND experiments carried out on the same ferrites, but the differences could, in the most, be explained by the need to use thin foils for electron microscopy purposes.

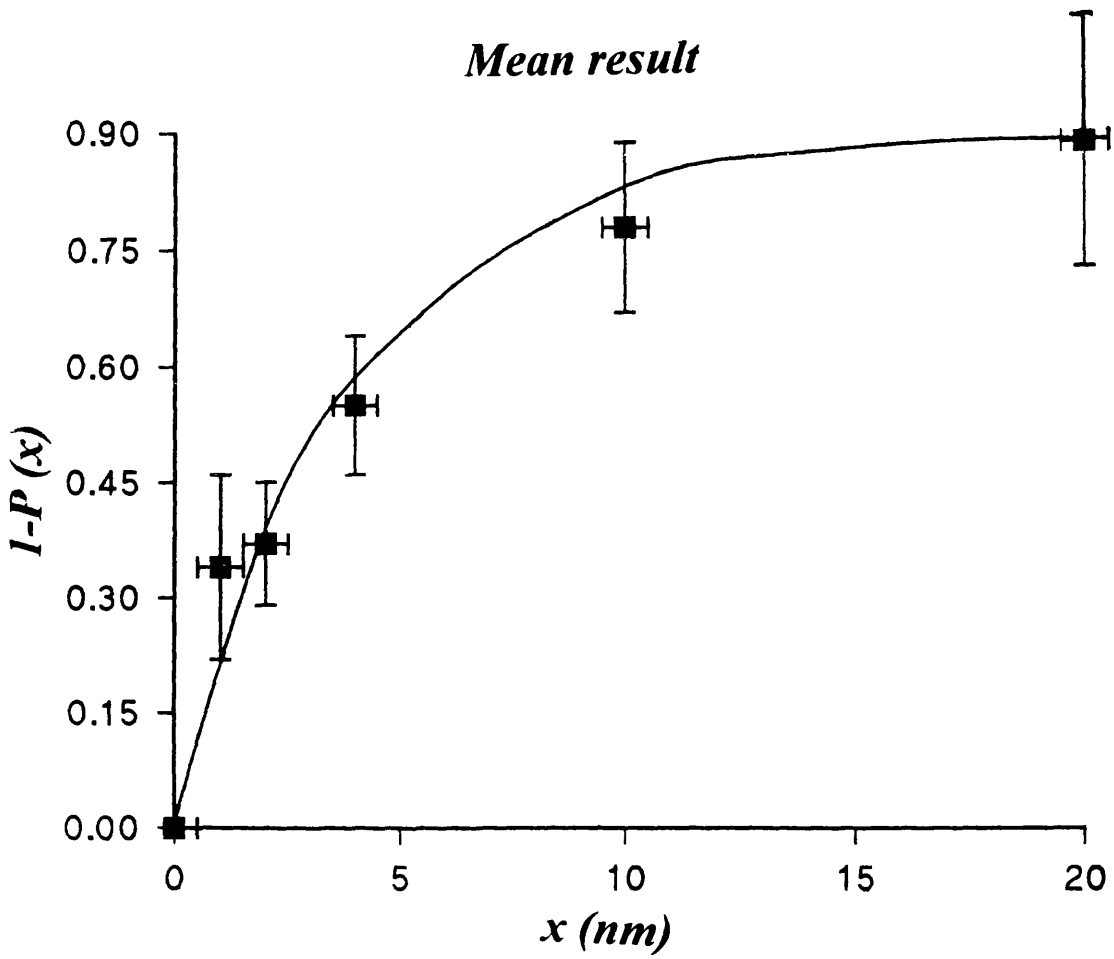

Figure 8.13 Mean compositional profile taken from results of figure 8.12.

The x-ray microanalysis showed that at the grain boundaries notable Zn depletion occurred which could lead to a decrease in initial permeability. From the microanalysis profile, the extent of the Zn depletion was shown to be in agreement with the calculations from the model suggested by Visser and Johnson.

Chapter 9

Conclusions and future work

Artificial multilayers of cobalt and platinum have been under extensive review during the past few years. Their magnetic and structural properties have been well documented as has their applicability as a future MO recording material. The aim of this project was to investigate directly, in detail, the domain structures that are supported by these films (both in the natural state and in the form of thermomagnetically written marks) using Lorentz microscopy. In particular the MDPC mode was employed because of the high spatial resolution (≈20nm) that can be achieved with this mode. The observations from these images were then related to bulk characteristics such as coercivity, anisotropy and shape of hysteresis loops. The application of in-situ magnetic fields allowed the nucleation and reversal mechanisms to be determined also using MDPC microscopy.

The last chapter of the thesis was concerned with the investigations of soft MnZn-ferrites. Lorentz microscopy and EDX microanalysis were employed to determine whether the grains were mono or multi-domain and whether they were surrounded by non-magnetic grain boundaries.

This chapter reports on the conclusions drawn from the results achieved throughout the thesis and also gives some recommendations for future work.

9.1 Conclusions

9.1.1 General

The initial work presented in chapter 3 summarised the deposition and characterisation of the multilayers and their suitability as future candidates as MO recording media. Lorentz microscopy (in particular MDPC microscopy) of

the same multilayers (deposited on specially prepared substrates for electron microscopy) demonstrated that despite the presence of substantial amounts of platinum these films revealed strong magnetic contrast which arose from a "maze-like" domain structure in which the direction of the domains were well defined. This type of structure arose because of the strong perpendicular anisotropy of the multilayers. The perpendicular anisotropy also necessitated a tilting of the specimen within the microscope to introduce a component of induction orthogonal to the electron beam. This tilting resulted in some areas of the films having a null deflection which appeared as grey regions in the MDPC images. The MDPC mode of Lorentz microscopy was found most suitable for the domain investigations of the multilayers. Despite a very small Lorentz deflection domains could be observed with a spatial resolution of ≈20nm, allowing detailed examinations of the structures in various remanent states.

The above technique was compared with SMFM in chapter 7. Natural domain structures within Co/Pt were imaged using both methods and the relative merits of both discussed. It was found that the routinely achieved resolution of SMFM was ≈100nm which did not compare favourably with the 20nm realised with MDPC. SMFM was not a very reproducible technique, mainly because of difficulties in tip fabrication and the possibilities of tip crashes during imaging. However it was accepted that bulk fabricated tips coated with thin magnetic films could greatly improve the reproducibility. The most important advantage of SMFM over any Lorentz technique is that no specimen preparation is required, therefore real discs can be imaged and the findings related to recording results. Unfortunately because it is magnetic forces being detected and not the induction itself, SMFM is not a linear imaging technique thus making quantitative analysis of the images difficult. Nevertheless it is a very useful technique and could be used in parallel with MDPC to gain a greater understanding of the magnetisation of the multilayers.

9.1.2 In-situ magnetising experiments

These experiments allowed direct observations of the domain structures of two films to be examined in various remanent states which corresponded to important points in the bulk magnetising loops, measured out on the AGFM. Such observations provided great insight into the mechanisms that determine the shape of the bulk magnetising loop. The reversal mechanism was found to be different for the two films; the lower coercivity film relied on domain wall motion, while it appeared that coherent rotation was the governing mechanism for the higher coercivity film. However from the fact that during magnetising the skeletal shape of domains remains mostly intact it can be concluded that the density of pinning points is high in both films. Finally these experiments showed that as Jakubovics (1991) had found (for films with in-plane magnetisation), not all domains annihilate with comparable ease.

9.1.3 Thermomagnetically written marks

The MDPC imaging mode proved most useful in the study of written marks. Previous Lorentz studies were not able to observe the marks with the same resolution thus making detailed conclusions difficult. However with the 20nm resolution available with MDPC microscopy the important features of the marks, which may effect signal levels, could be investigated in great detail. In chapter 5 the marks were studied on two films as both a function of bias field and applied laser power. Apart from their size (smaller in sample I, explained as being due to the lower Curie temperature) comparable marks in the two films did not show any remarkable differences and each set followed the same trends. Reverse domains were present in the written area until a large enough bias field ($\approx$30kA.m^{-1} for both films) was applied for the mark to become single domain. This behaviour could be explained with reference to the nucleation model described by Suits et al (1988). However, as the mark moved towards a single domain it was observed that the boundary became more irregular. Both reverse domains and irregular boundaries would lead to lower signal levels; thus it

would seem that the optimum writing parameters would be a sufficiently high enough bias field to eliminate reverse domains, but also to minimise edge irregularity. The laser power should be such that no recrystallisation occurs.

The quantitative analysis carried out in this chapter agreed well with the actual recording results presented by Zeper (1990) on similar films, thus validating the approach of using average pixel values to measure the signal level.

9.1.4 Domain wall energy

The Kooy and Enz model, adapted for multilayer structures was employed to estimate the domain wall energy density in a series of Co/Pt multilayers. By balancing the domain wall and magnetostatic energy contributions whilst the films were in a low energy state, it was shown that the experimentally measured domain periods could be modelled closely by using a magnetic characteristic length of 6.7nm. This value agreed well with that found by Zeper (1991). This value was then used to calculate the wall energy density and a figure of $12.9 mJ.m^{-3}$ was found. The validity of this result was examined by making use of the well known relationship between the wall energy and the exchange stiffness constant A and then comparing to quoted values of A for bulk cobalt. A good agreement was once again found.

9.1.5 MnZn-Ferrites

The Lorentz imaging of domain structures within the thinned ferrite samples proved quite difficult mainly due to the strong crystallographic contrast arising from the polycrystalline nature of the films. However, in the larger grained ferrite it was possible to observe domains in grains close to the ion-milled hole. In general these grains were not mono-domain, although in many instances the grain boundary did act as a domain wall also. The results were less clear in the smaller grained sample, although it was observed again (from Fresnel imaging) that many grains were multi-domain. These results were in conflict with previous neutron depolarisation experiments, on the same samples, which

showed that grains less than 4μm should be mono-domain. However, the discrepancies found between the two methods could possibly be explained by the need to thin the ferrites for use in the electron microscope.

The EDX microanalysis carried out on the smaller grained ferrite proved most successful and clearly showed that there was a substantial depletion of Zn in the vicinity of the grain boundary. This could lead to a region of significantly lower permeability and thus suggests that in the model of Johnson and Visser (1990), the boundaries (of the order of 2nm) would have substantially different magnetic properties, but we have seen no evidence that they would be non-magnetic.

9.2 Suggestions for future work

9.2.1 Co/Pt multilayers

The Lorentz studies on these multilayers have provided a great deal of information relating to their domain structures. However there are still many experiments that could be undertaken to expand this knowledge. Improved instrumentation will allow for such experiments to be undertaken. At Glasgow University a new instrument optimised for the study of magnetic materials should be in place by early 1993. The new magnetic microscope will be based on a Philips CM20 FEG TEM/STEM and will offer a number of features not readily available on other instruments. Foremost among these will be a larger specimen chamber that will allow a wide range of in-situ experiments to be undertaken. It will also be equipped with a Lorentz lens allowing CTEM and STEM modes to be accessible with state-of-the-art resolution and with the specimen situated in field free space and will have an analytical capability allowing more flexibility in obtaining structural or compositional information from areas of magnetic interest. With particular reference to Co/Pt multilayers, these features should allow the domain structures to be studied as a function of temperature (in particular in the vicinity of the Curie temperature) as well as magnetic field, which is vitally important to gain a better understanding of the magnetisation processes that arise in MO media. The analytical facilities (EELS,

EDX) could be employed to allow the structure and composition of the multilayers to be investigated in areas such as the ragged edges of written marks (where the coercivity may vary locally) and also to investigate the actual nature of pinning sites in the naturally occurring domain, established from magnetising experiments.

As mentioned in chapter 5 a method to analyse quantitatively the degree of raggedness and determine a single figure of merit for a written mark boundary was proposed. To make full use of such a technique it should be applied to a series of marks such as those shown in chapter 5 where qualitatively it is observed that as the bias field increased during writing the edge became more ragged. Such an experiment, when carried out in parallel with the quantitative analysis of the magnetisation of the mark would provide a clearer representation of the signal level and could be compared more closely with the actual recording results.

Throughout the above chapter, only continuous lines and laser modulated marks were studied. However, another common method for writing domains in MO materials utilises magnetic field modulation (MFM) where the marks have greatly diminished dimensions, allowing for larger storage densities. Similar studies to those carried out in chapter 5 could be undertaken, examining the effect of bias field and the frequency at which it is modulated. Of interest would be the transition regions between domains of opposite polarity; their regularity and acuity.

Another important point is that the multilayer films studied throughout this thesis were deposited by electron beam evaporation, however on a commercial scale this method of production would be too costly and the most appropriate method of mass production would be sputtering. It would therefore be of interest to compare how the domain structures of such sputtered films behaved when under the influence of heat and magnetic fields.

Finally there are some new materials, closely related to Co/Pt multilayers, which could be employed as future MO materials. Examples are CoPt alloys

and Co/Ni multilayers. Similar experiments to those carried out in this study could be undertaken on these materials. One experiment in particular would be comparing the domain wall energy of CoPt alloys to the multilayers structures using the original Kooy and Enz model.

9.2.2 MnZn-ferrites

The new microscope will also be of help in furthering the studies of the domain structures and composition profiles of MnZn-ferrites. The increased spatial resolution will help markedly the observations of domains in smaller grained ferrites, although there will still be the strong crystallographic contrast from the grains themselves. With the available 200keV electrons it may be possible to image thicker areas of the samples which were previously opaque when using the 100keV electrons in the HB5. This would help to clear up the differences between the Lorentz observations and the results obtained from the neutron depolarisation experiments. These Lorentz observations presented in chapter 8, clearly showed the existence of multi-domain grains. Using the CM20 microscope, it should be possible to acquire x-ray spectra from the vicinity of the domain walls to gauge if any compositional variation can explain their presence within the grains.

Finally the compositional profile which gave further evidence of the existence of a non-magnetic grain boundary was only carried out on one sample with a grain size of 0.2μm. To truly validate the model of Johnson and Visser would require profiles to be undertaken on a series of ferrites with different grain sizes.

REFERENCES

Chapter 1

M. Aeschlimann, M. Scheinfein, J. Unguris, F.J.A.M. Greidanus and S. Klahn, *J. Appl. Phys.*, **68** 4710 (1990).

F. Bloch, *Z. Phys.*, **74** 295 (1931).

P.F. Carcia, A.D. Meinhaldt and A. Suna, *Appl. Phys. Lett.*, **47** 178 (1985).

P.F. Carcia, *J. Appl. Phys.*, **66** 5066 (1988).

P.F. Carcia and W.B. Zeper, *IEEE. Trans. Mag.*, **26** 1703 (1990).

J.T. Chang, J.F. Dillon and U.F. Gianola, *J. Appl. Phys.*, **36** 1110 (1965).

P. Chaudhari, J.J. Cuomo and R.J. Gambino, *Appl. Phys. Lett.*, **22** 337 (1973).

G.A.N. Connell, R. Allen and M. Mansuripur, *J. Appl. Phys.*, **53** 7759 (1982).

M. Faraday, *Trans. Roy. Soc.*, **5** 592 (1846).

F.J.A.M. Greidanus, B.A.J. Jacobs, J.H.M. Spruit and S. Klahn, *Appl. Phys. Lett.*, **54** 963 (1989).

F.J.A.M. Greidanus, W.B. Zeper, B.A.J. Jacobs, J.H.M. Spruit and P.F. Carcia, *Jap. J. Appl. Phys.*, **28-3** 37 (1989).

P. Hansen, *J. Magn. Magn. Mater.*, **83** 6 (1990).

M. Hartmann, B.A.J. Jacobs and J.J.M. Braat, *Philips Techn. Rev.*, **42** 37 (1985).

W. Heisenberg, *Z. Phys.*, **49** 619 (1928).

K. Ichihara, Y. Mizusawa, N. Yasuda and T. Suzuki, *J. Appl. Phys.*, **63** 5154 (1988).

J. Kerr, *Phil. Mag.*, **3** 339 (1877).

M.H. Kryder, *J. Appl. Phys.*, **57** 3913 (1985).

C.J. Lin and H.V. Do, *IEEE. Trans. Mag.*, **26** 1700 (1990).

S.B. Luitjens, *IEEE. Trans. Mag.*, **26** 6 (1990).

W.H. Meiklejohn, *Proc. IEEE.*, **74** 1570 (1986).

L. Neèl, *Compt. Rend.*, **241** 533 (1955).

Y. Ochiai, S. Hashimoto and K. Aso, *IEEE. Trans. Mag.*, **25** 3755 (1989).

P. Weiss, *J. Phys.*, **6** 661 (1907).

W.B. Zeper, F.J.A.M. Greidanus and P.F. Carcia, *IEEE. Trans. Mag.*, **25** 3764 (1989).

W.B. Zeper, F.J.A.M. Greidanus, P.F. Carcia and C.R. Fincher, *J. Appl. Phys.*, **65** 4971 (1989).

W.B. Zeper, Ph.D Thesis, Philips Research Laboratories, (1991).

Chapter 2

Y. Aharonov and D. Bohm, *Phys. Rev.*, **115** 485 (1959).

F. Bitter, *Phys. Rev.*, **38** 1903 (1931).

R.C. Cellota and D.T. Pierce, *Science.*, **234** 333 (1986).

J.N. Chapman and G.R. Morrison, *J. Magn. Magn. Mater.*, **35** 254 (1983).

J.N. Chapman, *J. Phys. D: Appl. Phys.*, **17** 623 (1984).

J.N. Chapman, E.M. Waddell, P.E. Batson and R.P. Ferrier, *Ultramicroscopy*, **4** 283 (1979).

J.N. Chapman, I.R. McFadyen and S. McVitie, *IEEE Trans. Mag.*, **26** 1506 (1990).

A.V. Crewe, in 'Electron Microscopy and Materials Science, ed U. Valdre 162 (1971).

N.H. Dekkers and H. de Lang, *Optic*, **41** 452 (1974).

P. Grütter, E. Meyer, H. Heinzelmann et al, *J. Vac. Sci. Technol.*, **A6** 279 (1988).

M.E. Hale, H.W. Fuller and H. Rubenstein, *J. Appl. Phys.*, **30** 789 (1959).

S. McVitie, Ph.D. Thesis, University of Glasgow, (1988).

G.R. Morrison, Ph.D. Thesis, University of Glasgow, (1981).

W. Rave, R. Schaffer and A. Hubert, *J. Magn. Magn. Mater.*, **65** 7 (1987).

D.J. Rogers, Ph.D. Thesis, University of Glasgow, (1990).

K. Tsuno and T. Taoka, *Jap. J. Appl. Phys.*, **22** 1047 (1983).

E.M. Waddell and J.N. Chapman, *Optic*, **54** 83 (1979).

Chapter 3

J.P.C. Bernards and C.P.G. Schrauwen, Ph.D Thesis, Philips Research Laboratories (1989).

S. Chikazumi, in "Physics of Magnetism" ed. S.H. Charap (J. Wiley & Sons) (1964).

S. Foner, *Rev. Sci. Instrum.*, **30** 584 (1959).

F.J.A.M. Greidanus, B.A.J. Jacobs, F.J.A. den Broeder, J.H.M. Spruit and M. Rosencrantz, *Appl. Phys. Lett.*, **54** 963 (1989).

S. Hashimoto, Y. Ochiai and K. Aso, *J. Appl. Phys.*, **67** 4429 (1990).

P. He, W.A. McGahan, J.A. Woollam, F. Sequeda, T. McDaniel and H. Do, *J. Appl. Phys.*, **69** 4021 (1991).

J.W.M Jacobs and J.F.C.M Verhoven, *J. of Microscopy.*, **143** 103 (1986)

Z.G. Li and P.F. Carcia, *J. Appl. Phys.*, **71** 842 (1992).

C.J. Lin, G.L. Gorman, C.H. Lee, R.F.C. Farrow, E.E. Marinero, H.V. Do, H. Notarys and C.J. Chien, to be published in: *J. Magn. Magn. Mater.* (1992).

Y. Ochiai, S. Hashimoto and K. Aso, *IEEE Trans. Mag.*, **25** 3755 (1989).

K. Sato, Jap. *J. Appl. Phys.*, **20** 2403 (1981).

D.Weller, H. Notarys, G. Gorman, T. Logan, I. McFadyen and C.J. Chien, to be published in: *IEEE Trans. Mag.*, (1992).

W.B. Zeper, Ph.D Thesis, Philips Research Laboratories, (1991).

W.B. Zeper, F.J.A.M. Greidanus, P.F. Carcia and C.R. Fincher, *J. Appl. Phys.*, **65** 4971 (1989).

H. Zijlstra, *Rev. Sci. Instrum.*, **41** 1241 (1970).

Chapter 4

H.J.G. Draaisma and W.J.M. de Jonge, *J. Appl. Phys.*, **62** 3318 (1987).

P.J. Flanders, *J. Appl. Phys.*, **63** 3940 (1988).

J.P. Jacubovics, *J. Appl. Phys.*, **69** 4029 (1991).

C. Kooy and U. Enz, *Philips Res. Rep.*, **15** 7 (1960).

C.J. Lin, J.C. Suit and R.H. Geiss, *J. Appl. Phys.*, **63** 3835 (1988).

B. Liu, W.W. Clegg and C.D. Wright, *J. Magn. Magn. Mater.*, **101** 245 (1991).

M. Mansuripur, *J. Appl. Phys.*, **61** 1580 (1987).

K. O'Grady, *IEEE Trans. Mag.*, **26** 1870 (1990).

H. Zijlstra, *Rev. Sci. Instrum.*, **41** 1241 (1970).

Chapter 5

M. Aeschlimann, M. Scheinfein, J. Unguris, F.J.A.M. Greidanus and S. Klahn, *J. Appl. Phys.*, **68** 4710 (1990).

B.E. Bernacki and M. Mansuripur, *J. Appl. Phys.*, **69** 4960 (1991).

W. W. Clegg, N.A.E. Heyes, E.W. Hill and C.D. Wright, *J. Magn. Magn. Mater.*, **83** 535 (1990).

F.J.A.M Greidanus, B.A.J. Jacobs, F.J.A. den Broeder, J.H.M. Spruit and M. Rosencrantz, *Appl. Phys. Lett.*, **54** 963 (1989).

F.J.A.M Greidanus, B.A.J. Jacobs, J.H.M. Spruit and S. Klahn, *IEEE Trans. Mag.*, **25** 3524 (1989).

P. Hansen, *J. Appl. Phys.*, **62** 216 (1987).

B. Huth, *IBM J. Res. Develop.*, **18** 100 (1974).

K. Ichihara, Y. Mizusawa, N. Yasuda and T. Suzuki, *J. Appl. Phys.*, **63** 5154 (1988).

C.J. Lin, J.C. Suits and R.H. Geiss, *J. Appl. Phys.*, **63** 3835 (1988).

W. Qian and D.M. Titterington, to be published in, *Phil. Trans. R. Soc. A.*

D. Shieh, Ph.D Thesis, Carnegie Mellon University (1987).

J.C. Suits, D. Rugar and C.J. Lin, *J. Appl. Phys.*, **64** 252 (1988).

H.W. van Kesteren, A.J. den Boef, W.B. Zeper, J.H.M. Spruit, B.A.J. Jacobs and P.F. Carcia, *J. Appl. Phys.*,**70** 2413 (1991).

W.B. Zeper, Ph.D Thesis, Philips Research Laboratories (1991).

Chapter 6

J.P.C. Bernards and C.P.G. Schrauwen, Ph.D Thesis, Philips Research Laboratories (1989).

H.J.G. Draaisma and W.J.M. de Jonge, *J. Appl. Phys.*, **62** 3318 (1987).

C. Kooy and U. Enz, *Philips Res. Rep.*, **15** 7 (1960).

M. Mansuripur, *J. Appl. Phys.*, **66** 6175 (1989).

G. Schutz, R. Wienke, W. Wilhelm, W.B. Zeper, H. Ebert and K. Sporl, *J. Appl. Phys.*, **67** 4456 (1990).

P.E. Tannenwald and R. Weber, *Phys. Rev.*, **121** 715 (1961).

T. Wielinga, Ph.D Thesis, University of Twente (1983).

W.B. Zeper, Ph.D Thesis, Philips Research Laboratories (1991).

Chapter 7

J.P.C. Bernards and C.P.G. Schrauwen, Ph.D Thesis, Philips Research Laboratories (1989).

G. Binnig, C.F. Quate and Ch. Gerber, *Phys. Rev. Lett.*, **56** 930 (1986).

A.J. den Boef, *Appl. Phys. Lett.*, **56** 2045 (1990).

A.J. den Boef, Ph.D Thesis, Philips Research Laboratories, (1991).

D.M. Donnet, J.N. Chapman, H.W. van Kesteren, W.B. Zeper, *J. Magn. Magn. Mater.*, **115** 342 (1992).

P. Grütter, D. Rugar, H.J. Mamin, G. Castillo, S.E. Lambert, C.J. Lin, R.M. Valletta, O. Wolter, T. Bayer and J.Greschner, *Appl. Phys. Lett.*, **57** 1820 (1990).

P. Grütter, H.J. Mamin and D. Rugar, in 'Scanning Tunnelling Microscopy II', ed's H.J Guntherodt and R. Wiesendanger (Springer-Verlag Berlin Heidelberg 1992).

U. Hartmann, *J. Appl. Phys.*, **64** 1561 (1988).

P.C.D. Hobbs, D.W. Abraham and H.K. Wickramasinghe, *Appl. Phys. Lett.*, **55** 2357 (1989).

Y. Martin, C.C. Williams and H.K. Wickramasinghe, *J. Appl. Phys.*, **61** 4723 (1987).

Y. Martin and H.K. Wickramasinghe, *Appl. Phys. Lett.*, **50** 1455 (1987).

Y. Martin, D.W. Abraham and H.K. Wickramasinghe., *Appl. Phys. Lett.*, **52** 1103 (1988).

Y. Martin, D. Rugar and H.K. Wickramasinghe, *Appl. Phys. Lett.*, **52** 244 (1988).

D. Rugar, H.J. Mamin and P. Guethner et al, *J. Appl. Phys.*, **68** 1169 (1990).

C. Schönenberger and S.F. Alvarado, *Z. Phys. B- Cond. Matt.*, **80** 373 (1990).

H.W. van Kesteren, A.J. den Boef, W.B. Zeper, J.H.M. Spruit, B.A.J. Jacobs and P.F. Carcia, *J. Appl. Phys.*, **70** 2413 (1991).

Chapter 8

J.A. Bearden, in National Standard Reference Data Series No. 14, National Bureau of Standards, published by US Government Printing Office.

G. Cliff and G.W. Lorimer, Proc. 5TH European Congress on Electron Microscopy, Bristol (1972).

C.C. Gray, Ph.D Thesis, University of Glasgow, (1981).

J.I. Goldstein, J.L. Costly, G.W. Lorimer and S.J.B. Reed, SEM 1977, ed. O. Johari, IIRTI, Chicago (1977).

P.E.C. Franken and H. van Doveren, *Ber. Dtsch. Keram. Ges.*, **55** 287 (1978).

M.T. Johnson and E.G. Visser, *IEEE Trans. Mag.*, **26** 1987 (1990).

A.J. McGibbon, J.N. Chapman, A.G. Cullis, N.G. Chew, S.J. Bass and L.L. Taylor, *J. Appl. Phys.*, **65** 2293 (1989).

T. Pannaparayil, R. Marande and S. Komarneni, *J. Appl. Phys.*, **69** 5349 (1991).

D.J. Rogers, Ph.D Thesis, University of Glasgow, (1990).

R.C. Sundahl, B.B. Ghate, R.J. Holmes, C.E. Pass and W.C. Johnson, in Advances in Ceramics, edited by L.M. Levinson (American Ceramic Society, OH, 1981) Vol. 1, p502.

P.J. van der Zaag, M.T. Johnson, A. Noordermeer, P.T. Por and M.Th. Rekveldt, *J. Magn. Magn. Mater.*, **99** L1 (1991).

E.G. Visser and M.T. Johnson, *J. Magn. Magn. Mater.*, **101** 143 (1991).

Chapter 9

M.T. Johnson and E.G. Visser, *IEEE Trans. Mag.*, **26** 1987 (1990).

J.P. Jakubovics, *J. Appl. Phys.*, **69** 3940 (1988).

J.C. Suits, D. Rugar and C.J. Lin, *J. Appl. Phys.*, **64** 252 (1988).

W.B. Zeper, Ph.D Thesis, Philips Research Laboratories, (1991).